



University
of Glasgow

Qian, Ling (2001) Towards numerical simulation of vortex-body interaction using vorticity-based methods. PhD thesis

<http://theses.gla.ac.uk/4902/>

Copyright and moral rights for this thesis are retained by the author

A copy can be downloaded for personal non-commercial research or study, without prior permission or charge

This thesis cannot be reproduced or quoted extensively from without first obtaining permission in writing from the Author

The content must not be changed in any way or sold commercially in any format or medium without the formal permission of the Author

When referring to this work, full bibliographic details including the author, title, awarding institution and date of the thesis must be given.

Towards Numerical Simulation of Vortex-Body Interaction Using Vorticity-based Methods

L. Qian, B.Sc.(Eng), M.Sc.(Eng)

Thesis submitted to the Faculty of Engineering,
University of Glasgow, for the Degree of Doctor of Philosophy

University of Glasgow
Department of Aerospace Engineering

June 2001

© 2001 Ling Qian

Acknowledgements

I would like to express my sincere thanks to Dr. M. Vezza for his supervision and helpful discussion throughout the study. The efforts made by him regarding my thesis writing and subsequent proof-reading are also highly appreciated.

I'm indebted to Prof. Q.P. Cao of Nanjing University of Aeronautics and Astronautics, China, who introduced me into the fascinating field of CFD through supervising my M.Sc. study and subsequent working at NUAA.

I would also like to thank Prof. B.E. Richards and Prof. R.A. McD. Galbraith of the department for their help during the process of application and encouragement throughout my stay at the University of Glasgow.

The useful discussions with Allen Masson and Ian Taylor of the department are also gratefully acknowledged.

Finally, I would like to thank my wife Jue and son Junqiang as well as my parents for their understanding and patience during my Ph.D study and in fact, this thesis is dedicated to them.

Abstract

This study is mainly concerned with the application and development of the vorticity-based methods for unsteady aerodynamic problems, particularly, vortex-body interactions.

In the first part of the study, numerical results are presented for modelling vortex-vortex and vortex-body interactions (blade-vortex interaction in particular) by using the grid-free Lagrangian discrete vortex method.

For parallel blade-vortex interaction, a 2-D numerical model has been used and both the single vortex and twin vortex interacting with an aerofoil have been studied in which the interaction vortex or vortices are represented by several hundreds to several thousands of overlapping vortex particles. A new method has been developed for calculating the velocity of the nascent vortices to avoid oscillations in the normal component. The dominant mechanisms during a BVI event, namely the effective angle of attack induced by the approaching vortex and the local effect due to passage of the vortex close by or around the surface, have been analysed using the unsteady C_p distribution together with images of the passing interaction vortex. For relatively strong BVI, such as the head-on interaction case, vortex induced local flow separation has also been predicted in the present study. The effect of the angle of attack and the height of the interaction vortex on the strength of the interaction are then studied systematically. For a twin vortex system, the effect of the initial position on the subsequent interaction process has been examined in detail by calculating a number of cases with different initial vortex positions. Extensive

comparisons are made with other numerical results and the results from the Glasgow University BVI wind-tunnel test.

For normal blade-vortex interaction, the interaction between a vortex ring and a rectangular wing has been simulated by using a 3-D vortex particle method. The wing surface is represented by over one thousand source panels and each panel is further divided into multiple subpanels in order to calculate the velocity of the flow near the surface more accurately. The vortex ring is also discretised into several thousand overlapping vortex particles which is located at some distance upstream of the leading edge of the blade. The early stage of the interaction, namely where the core of the vortex ring has almost penetrated into the leading edge of the blade, has been simulated and the suction force due to the approaching vortex ring has been predicted by using a global vorticity based method which compares well with other numerical studies. Due to the limitations in the 3-D vortex particle method, some further study is needed to simulate the entire penetration process of the vortex ring.

To reduce the computational cost of the 3-D vortex particle method, an adaptive fast summation algorithm, based on the Taylor expansion of kernel functions arising from calculating the velocity using Biot-Savart law, has been implemented. An efficient hierarchical incomplete tree-code for sorting vortices and calculating velocity has been incorporated into the code. The performance of the algorithm, namely the accuracy and efficiency etc., has been tested by calculating the interaction of two vortex rings using a large number of vortex particles, which shows that the present method provides a simpler alternative to the prevailing fast multipole method for 3-D flow problems.

In the second part of the study, a new hybrid vorticity-based method combining some favourable features in the finite volume method and the discrete vortex method has also been developed. In this method, the vorticity transport equation in

conservative form is solved by using the cell-centred finite volume method, while the velocities needed at the centre of each control volume are calculated by a modified Biot-Savart formula in conjunction with a fast summation algorithm. The vorticity and mass conservation in the flow are guaranteed during the calculation by virtue of the finite volume approach and the method of implementing the boundary conditions at the body surface. To demonstrate the feasibility and accuracy of the method, both the early stage development and long term evolution of the flow around an impulsively started circular cylinder have been computed. The present results are compared with other numerical and experimental results for the same flow problem, and show very good agreement. This method can accommodate both structured and unstructured grids and has the ability to capture very fine vortex structures in the flow. These features make the method an ideal tool to study both 2-D and 3-D vortex-body interaction problems.

Finally, some conclusions drawn from the study will be discussed.

Nomenclature

c	Blade chord length
C_d	Drag coefficient
C_l	Lift coefficient
$C_{m\frac{1}{4}}$	Quarter-chord moment coefficient
C_n	Normal force coefficient
C_t	Tangential force coefficient
G	The Green function
$\mathbf{i}, \mathbf{j}, \mathbf{k}$	Unit vector for x,y,z direction respectively
N_p	Total number of panels around the surface of an aerofoil or wing
N_s	Number of nascent vortices in each panel
N_v	Total number of vortex particle in the flow
p	Pressure
r	Radial position from the centre of a vortex particle
R	Rotor blade radius or radius of a circular cylinder
Re	Reynolds number
(\mathbf{s}, \mathbf{n})	Unit vector of the local surface coordinate system
t, T	Time

\mathbf{u}	Velocity vector, (u,v,w)
\mathbf{u}_∞	Velocity of the free stream
\mathbf{x}, \mathbf{y}	Position vector, (x,y,z)
(X_v, Y_v)	Initial position of the interaction vortex
Z	Complex position of a point in x-y plane, $x+ yi$
α	Angle of attack
α_j	Strength vector of 3-D vortex particle j
γ	The density of the circulation in the control zone
σ	Core radius of vortex particles or a vortex ring; strength of a source panel
ω	Vorticity vector
δ	Height of the control zone or the Dirac delta function
Γ_j	Circulation of vortex particle j
Γ_v	Circulation of the interaction vortex
ν	Coefficient of kinematic viscosity
Ω	Angular velocity of a rotating body
ψ	Stream function
Ψ	Vector potential
Δs	Length of each panel

Contents

Acknowledgements	ii
Abstract	iii
Nomenclature	vi
1 Introduction	1
1.1 Background of the study	1
1.2 Review of previous BVI studies	4
1.3 Discrete vortex methods	11
1.4 The scope of the present study	19
1.5 Layout of the thesis	22
2 Theoretical Background of Vortex Methods	24
2.1 Governing equations and boundary conditions	24
2.2 Generalised Biot-Savart law	28
2.3 Construction of vorticity-based method	31
3 Implementation of the Discrete Vortex Method	33
3.1 Two dimensional case	33
3.1.1 Discretization and evolution of vorticity field	33
3.1.2 Representation of body surface and implementation of bound- ary conditions	39

3.1.3	Calculation of the surface pressure	42
3.1.4	Controlling the total number of particles	45
3.2	Three dimensional case	47
3.2.1	Discretization and evolution of vorticity field	47
3.2.2	Discretization of 3-D body surface - source panel method . . .	57
3.2.3	Calculation of aerodynamic forces	60
4	Results and Discussion for Vortex-Body Interaction	62
4.1	Parallel Blade-Vortex Interaction: Single Vortex	62
4.1.1	Rankine vortex model: comparison with the panel method . .	62
4.1.2	Scully vortex model: Comparison with experimental data . . .	71
4.2	Parallel Blade-Vortex Interaction: Twin Vortices	76
4.3	Normal vortex-ring body interaction	82
4.3.1	Validation of the numerical method	82
4.3.2	Inviscid normal vortex-body interactions	88
5	Fast summation algorithm	97
5.1	Basic idea	97
5.2	Taylor expansion	99
5.3	Mesh structure and sorting of vortices	102
5.4	Velocity calculations	105
5.5	Performance of the algorithm	107
5.5.1	Accuracy of the algorithm	107
5.5.2	Timing of the fast algorithm	108
5.5.3	High resolution calculation of twin vortex ring interaction . . .	109
5.6	Conclusions	110
6	Implementation of the New Hybrid Vorticity-based Method	116

6.1	Basic idea of the method	116
6.2	Solution of vorticity transport equation	116
6.3	Velocity calculation	119
6.4	Implementation of boundary conditions	122
6.5	Calculation of surface pressure and body forces	126
6.6	Results and Discussion	127
6.6.1	Fast algorithm vs direct summation	129
6.6.2	Grid effects	129
6.6.3	Comparison with other results	131
6.6.4	Long time calculation: $Re = 1000$	142
6.7	Conclusions	145
7	Conclusions and Future study	148
7.1	2-D parallel BVI	148
7.2	Normal blade-vortex interaction	150
7.3	Fast summation algorithm	151
7.4	The new hybrid vorticity-based method	152
7.5	Concluding remarks	152
A	Recurrence relations for $a_k(\mathbf{x}, y_\tau) = \frac{1}{k!} D_y^k f(\mathbf{x}, y)_{y=y_\tau}$	154
B	Proof of equation 2.26	155
	Bibliography	158

List of Tables

5.1	Convergence study of the fast algorithm in terms of the order of Taylor expansion λ	108
5.2	Effect of λ value on timing of the fast algorithm	108
6.1	Drag coefficient and Strouhal number for the flow around a circular cylinder at $Re = 1000$	147

List of Figures

1.1	A summary of specific flow problems which occur on a helicopter. From Conlinsk(1997)	2
1.2	Three typical cases of BVI: parallel, normal and streamwise interactions	2
1.3	Definition sketch for two dimensional parallel BVI	3
1.4	The set-up of wind tunnel BVI tests at Glasgow University[44]	5
1.5	Cp distribution and aerodynamic loads on the blade cross-section from BVI tests at Glasgow University[57]	6
1.6	Vortical flow(twin vortex system) associated with the vane tip con- figuration of a helicopter blade. From Brocklehurst et al(1994)	7
1.7	Deformation and splitting of the vortex during the head-on interac- tion predicted by a panel method. From Lee and Smith(1991)	8
1.8	Flow visualization of the complex flow field during the normal BVI in the strong vortex regime. From Krishnamoorthy and Marshall(1998)	9
1.9	Splitting of the vortex filament during a normal BVI predicted by a vortex filament method. From Marshall and Yalamanchill(1994)	10
1.10	Boundary elements and vortex tiles used on surface in 3-D discrete vortex method. From Gharakhani(1997)	17
3.1	Vorticity and velocity distributions for various 2-D core functions	36
3.2	Discretisation of the core of the interaction vortex using vortex particles: $r_c = r_l \frac{1+12n^2}{6n}$	37

3.3	Core overlapping condition on accuracy of solution for a vortex with Rankine core	38
3.4	Illustration of surface panels and vortex particle generation using the linear distributed density of circulation in the control zone	41
3.5	Calculation of newly created circulation from the body surface for each surface control volume	43
3.6	Calculation of the contribution to the aerodynamic force and moment from each panel	44
3.7	Results for the interaction and fusion of two vortex rings using the 3-D vortex particle method	52
3.7	Continued	53
3.7	Continued	54
3.7	Continued	55
3.7	Continued	56
3.8	Illustration of a planar surface panel for 3-D calculation	58
4.1	Surface pressure distribution during BVI at the lower surface of a NACA 0012 aerofoil for three initial vertical positions of the interaction vortex	64
4.2	Surface pressure distribution during BVI at the upper surface of a NACA 0012 aerofoil for three initial vertical positions of the interaction vortex	65
4.3	Effects of initial vertical position of the oncoming vortex on the induced velocity near the leading edge	66
4.4	Surface pressure distribution during BVI at the lower surface of a NACA 0012 aerofoil without modification of stagnation point pressure coefficient	66

4.5	Evolution of the aerodynamic coefficients during BVI for three initial vertical positions of the interaction vortex and comparison with the panel method[63]	67
4.6	The trajectory of vortex particles during BVI for $Y_v/c = -0.26$	68
4.7	The trajectory of vortex particles during BVI for $Y_v/c = 0.26$	68
4.8	Effect of induced surface vorticity on convection velocity of the vortex	69
4.9	The trajectory of vortex particles during BVI for $Y_v/c = 0.0$	69
4.10	The set-up of BVI wind tunnel test at Glasgow University	71
4.11	Evolution of aerodynamic coefficients during the BVI and comparison with the BVI test from [74]	73
4.12	Vortex induced local flow separation: trajectory of the vortex particles for $Y_v/c = 0.0$	74
4.13	Upper surface pressure distribution during BVI for $Y_v/c = 0.1$	75
4.14	Effects of initial vertical position and flow incidence on ΔC_n : a comparison with the BVI test[71]	76
4.15	Definition sketch of initial position of the twin vortex system	77
4.16	Deformation and rotation of a twin vortex system	80
4.17	Evolution of the aerodynamic forces during the twin BVI and comparison with the wind tunnel test[74]	81
4.18	Evolution of the quarter chord moments during the twin BVI	82
4.19	Trajectory of vortices during a twin bvi event: $\theta = 30^\circ$	83
4.20	Trajectory of vortices during a twin bvi event: $\theta = 120^\circ$	84
4.21	Surface pressure distribution during a twin BVI event: $\theta = 30^\circ$	85
4.22	Surface pressure distribution during a twin BVI event from the wind tunnel test[71]	86
4.23	Surface pressure distribution during a twin BVI event: $\theta = 120^\circ$	87
4.24	Dimensionless self-induced propagation speed of a vortex ring	89

4.25	Effect of particle overlapping condition on the accuracy of velocity calculation in 3-D vortex particle method	89
4.26	Illustration of vortex ring-sphere interaction problem	90
4.27	Comparison of vortex induced force on body for the vortex ring-sphere interaction problem between present study and Butler's sphere theorem[10]	90
4.28	Prediction of drag coefficients for the normal blade-vortex ring interaction and comparison with the numerical results from the vorticity collocation method[69]	91
4.29	Initial position of the vortex ring and surface discretization of the wing for the normal vortex ring-blade vortex interaction problem . . .	91
4.30	Trajectory of the vortex particles during the normal vortex ring-blade interaction	92
4.31	Prediction of drag coefficient of the normal interaction between a vortex ring and a sphere	93
4.32	Prediction of side force coefficient of the normal interaction between a vortex ring and a sphere	93
4.33	Trajectory of the vortex particles during the normal interaction between a vortex ring and a sphere	94
5.1	Illustration of a complete three-level binary tree in the context of vortex sorting	103
5.2	Illustration of an incomplete four-level binary tree in the context of vortex sorting	104
5.3	Logic flow chart for adaptive grid generation and vortex sorting . . .	105
5.4	Logic flow chart for calculating velocity using the fast summation algorithm	106

5.5	Vortex particle distribution at $T = 4.0$ from the direct summation method for the two vortex ring interaction problem	109
5.6	Vortex particle distribution at $T = 4.0$ from the fast summation method for the two vortex ring interaction problem	110
5.7	Comparison of CPU timing between the fast algorithm and the direct summation method for the two vortex ring interaction problem	111
5.8	Results for the interaction and fusion of two vortex rings using the fast summation algorithm	112
5.8	Continued	113
5.8	Continued	114
5.8	Continued	115
6.1	Definition sketch of a control volume in the hybrid vortex method . .	117
6.2	Illustration for a control volume and its four neighbouring cells in the context of calculating convective and viscous fluxes	117
6.3	Velocity contribution from each control volume using the modified Biot-Savart law	119
6.4	Square adaptive zonal decomposition in the context of fast summation algorithm for velocity calculations	121
6.5	Illustration for surface vorticity flux calculation	124
6.6	Definition sketch of the flow past a circular cylinder	128
6.7	Coordinate system and the grids for the flow past a circular cylinder .	128
6.8	Accuracy of the fast algorithm: Drag coefficient	130
6.9	Accuracy of the fast algorithm: Vorticity contours	130
6.10	Effect of grid density on the drag coefficient	131
6.11	Effect of grid density on the streamlines	132
6.12	Comparison of drag coefficients, $Re = 550$	133

6.13 Radial velocity distribution along the rear centre line of the circular cylinder, $Re = 550$	134
6.14 Vorticity contours: $Re = 1000$	135
6.15 Surface vorticity distribution: $Re = 1000$	136
6.16 Comparison of drag coefficients: $Re = 1000$	136
6.17 Vorticity contours: $Re = 3000$	138
6.18 Surface vorticity distribution: $Re = 3000$	139
6.19 Comparison of drag coefficients, $Re = 3000$	139
6.20 Streamlines for $Re = 3000$ at $T = 5.0$; A: Calculated, B: Experiments[9]	140
6.21 Radial velocity distribution along the rear centre line of the circular cylinder, $Re = 3000$	141
6.22 Surface vorticity distribution: $Re = 9500$	142
6.23 Vorticity contours: $Re = 9500$	143
6.24 Comparison of drag coefficients, $Re = 9500$	144
6.25 Radial velocity distribution along the rear centre line of the circular cylinder, $Re = 9500$	144
6.26 Vorticity contours for $Re = 1000$: long time calculation	145
6.27 Streamlines for $Re = 1000$, $T = 168.0$	146
6.28 Evolution of drag and lift coefficients: $Re = 1000$	146

Chapter 1

Introduction

1.1 Background of the study

The phenomenon of a vortex, which is defined as a region of concentrated vorticity of one sign, or combination of vortices, interacting with a body occurs in many engineering applications, such as helicopters, aircraft, wind turbines, as well as a cluster of risers of an off-shore platform and a group of tall buildings. Of particular interest to the Department of Aerospace Engineering is the study of helicopter aerodynamics in which blade-vortex interaction(BVI), along with dynamic stall etc., is one of the key problems, as depicted in fig.1.1.

Under certain flight conditions, a rotor blade may encounter or pass through the tip vortices trailed from either itself or other preceding blades, or vortices shed from the blade surface during the process of dynamic stall. The BVI event not only drastically changes the aerodynamic loads on the rotor, but has also long been considered one of the sources of helicopter noise and vibration. In recent studies of BVI and vortex interaction with other forms of body, a variety of flow patterns have been revealed, such as the deformation and even splitting of the interaction vortex, and vortex-induced boundary layer flow separation in a close strong interaction.

Generally, blade vortex interaction is a complicated three-dimensional flow problem. Depending on the flight trajectory of a helicopter, the interaction may involve

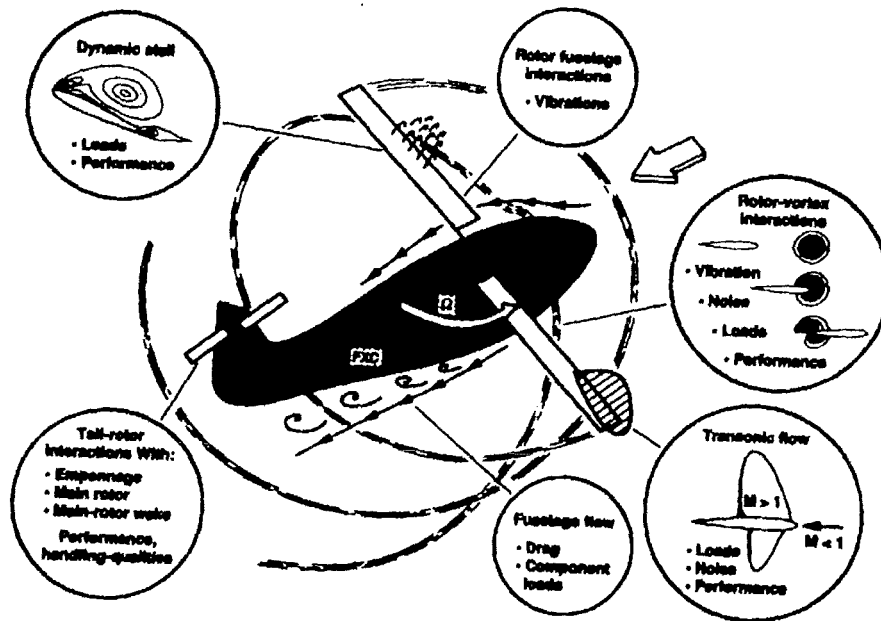


Figure 1.1: A summary of specific flow problems which occur on a helicopter. From Conlinsk(1997)

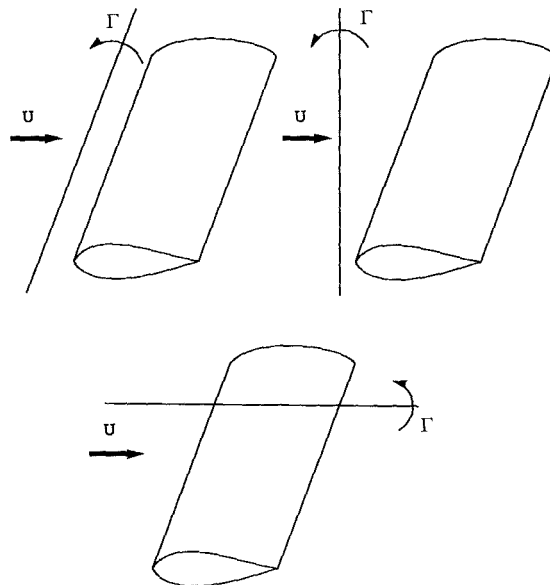


Figure 1.2: Three typical cases of BVI: parallel, normal and streamwise interactions

an oblique vortex. However, as a simplification, three extreme cases(fig.1.2) exist in terms of the interaction angle between the axis of the vortex and the spanwise direction of the blade: parallel interaction, streamwise interaction and normal interaction. Furthermore, if the spanwise variation of the flow is neglected, then the parallel interaction can be approximated by a two-dimensional model. In this case, as shown in fig.1.3, the whole event is simply controlled by the initial position, circulation or strength and the size of the oncoming vortex.

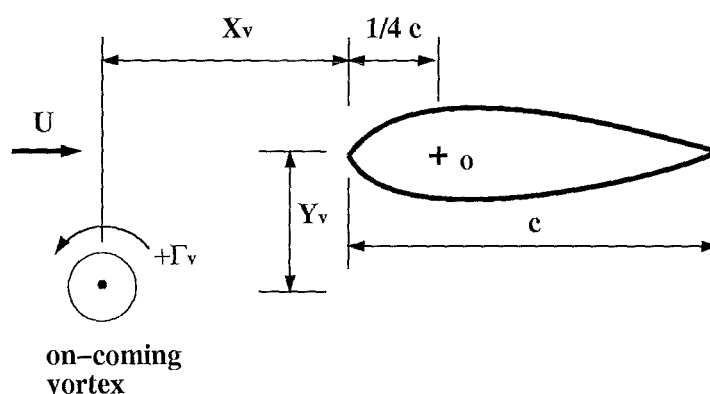


Figure 1.3: Definition sketch for two dimensional parallel BVI

Because of the importance of understanding the mechanisms of BVI, it has received considerable attention in recent years. An excellent comprehensive review of both experimental and numerical studies of vortex body interaction including BVI was given by Rockwell[92]. Due to the nature of this kind of flow, i.e. the vorticity is concentrated only in a small region occupied by the vortex and around the surface of the body or blade, vorticity based methods(possibly the Lagrangian description) are particularly desirable and have been strongly recommended by the authors for the simulation and interpretation of BVI events in future studies.

The present study is mainly concerned with the numerical simulation of the 2-D parallel and 3-D normal blade vortex interaction by using the Lagrangian discrete vortex methods. Some more general topics on the construction of a 3-D discrete

vortex code for simulating general unsteady flows including development of a fast summation algorithm are also discussed. Due to some limitations in the discrete vortex method, particularly the difficulties in extending the method to 3-D problems, a new vorticity-based method has also been developed in the study, which hopefully can be applied to the vortex-body interaction problems in the future.

In the following sections of this chapter, previous BVI studies are briefly reviewed, followed by a detailed description of the historical development and the state-of-the-art of discrete vortex methods. Then the scope of the present work is discussed and the layout of the thesis is given.

1.2 Review of previous BVI studies

During the last three decades, a limited number of experimental studies have been carried out in an attempt to gain a clear understanding of the fluid dynamics behind the BVI phenomenon.

In the pioneering work conducted by Surendraiah(1969)[111] and subsequently by Padakannaya(1971)[81], an isolated blade vortex interaction was studied by using an upstream wing tip to generate a vortex that interacted with a downstream rotor. The surface pressure distribution of the blade was measured using pressure transducers and thus the gross features of the BVI, including the development and collapse of a large leading edge suction peak during the interaction, and the associated buildup and reversal of the normal force, were documented.

A similar study at NASA Ames Center using a higher resolution in pressure measurement was able to identify a “convective disturbance” of the suction pressure ridge associated with the overhead passage of the interaction vortex.

More recently, at Glasgow University, a series of parallel BVI tests have been carried out by using a set-up similar to the previous studies as shown in Fig.1.4. In these studies, the interaction vortex was generated by two adjoining wings of NACA

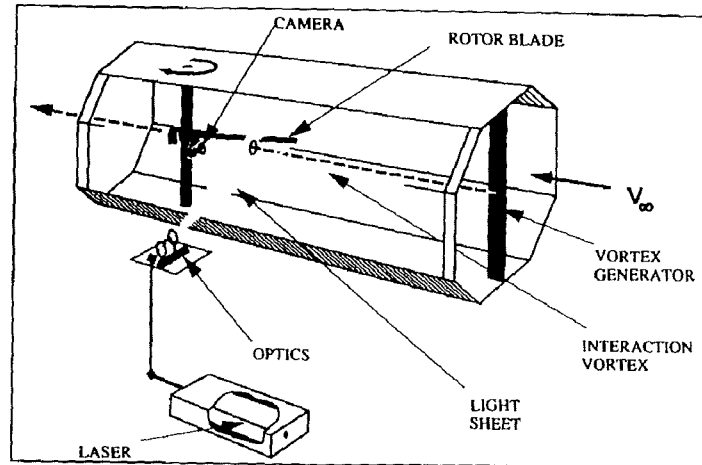


Figure 1.4: The set-up of wind tunnel BVI tests at Glasgow University[44]

0015 aerofoil section set at equal but opposite incidence. A linear relationship has been achieved between the strength of the interaction vortex and the incidence of the wing. By using much greater resolution in the measurement of the surface pressure distribution, not only the integration of the normal force, but also the moment and the tangential force were obtained[57], see fig.1.5. Further development of BVI test facilities[43],[44] focused upon the utilisation of some advanced techniques such as hot wire anemometry and particle image velocimetry. As a result, detailed measurements were made of the strength and core size of the interaction vortex and the trajectory of the vortex under the influence of the passing blade was recorded. Some phenomena associated with a strong close interaction, e.g. the deformation and the splitting of the vortex, as well as the vortex-induced boundary layer separation were clearly revealed with the aid of these techniques. A systematic parametric study has also been done to examine the effects of the initial vortex position and strength, and the pitching angle of the blade on the strength of the interaction.

Recent interest in the use of a Vane Tip(Brocklehurst and Pike(1994) [10], fig.1.6) to reduce the noise level of BVI by generating two weaker co-rotating vortices has initiated the study of the interaction between a blade and twin vortex system. Some

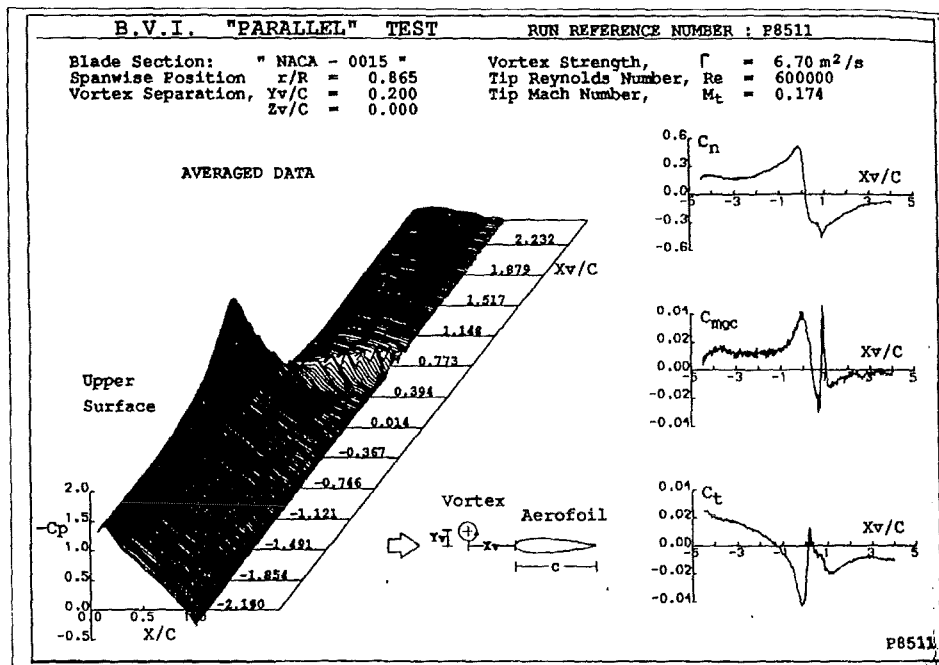


Figure 1.5: C_p distribution and aerodynamic loads on the blade cross-section from BVI tests at Glasgow University[57]

preliminary results have been reported by Copeland and Masson regarding the generation of a twin vortex system in wind tunnel tests[28] and measurement of the loads on the blade under the influence of twin vortices[74] respectively. Because of the complexity of the twin vortex system, further study is needed to clarify some details of the flow structure during the interaction.

Instead of studying the interaction between a rotor blade with a tip vortex, some researchers have used different set-ups in an attempt to remove 3-D effects of the rotor blade during the interaction. In these studies, notably by Booth[8], Seath[99] and Straus[110], the two-dimensional transverse vortex generated by either an upstream oscillating rectangular wing or impulsively pitching wing interacted with a fixed downstream finite wing and the surface pressure distribution, and hence the integrated loads on the aerofoil, were obtained.

Meanwhile, numerical studies, mainly based on unsteady panel methods and

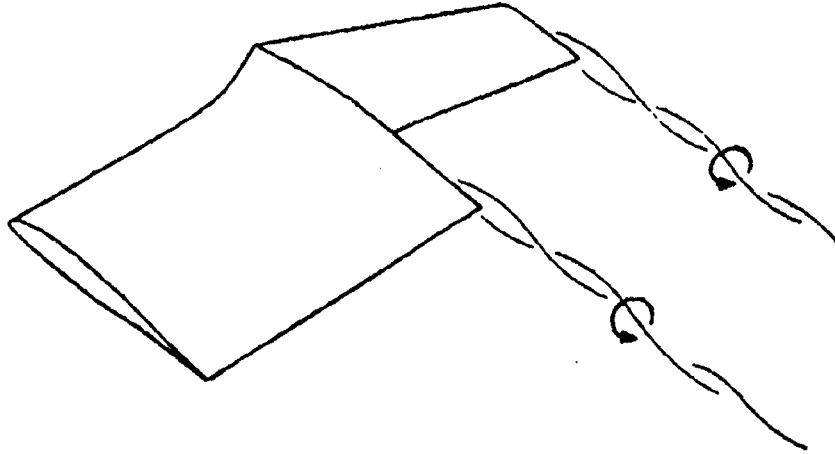


Figure 1.6: Vortical flow (twin vortex system) associated with the vane tip configuration of a helicopter blade. From Brocklehurst et al(1994)

conformal mapping methods, have also contributed significantly to the understanding of the BVI event. In the early studies, a point vortex was used to represent the interaction vortex, and its influence on the aerodynamic forces on the aerofoil was given. In [83], a point vortex is convected past an aerofoil at a fixed half-chord separation distance, while in [22], the same problem was examined by allowing the vortex to move freely in response to the induced flow field around a Joukowski aerofoil. More recently, the distributed vortex model, in which the finite core of the vortex was discretised into multiple vortex elements or blobs, was employed by Lee and Smith[63](fig.1.7) and Mook and Dong[77]. In these studies, the aerofoil surface was represented by either source panels or vorticity panels and the vorticity shed from the trailing edge of the aerofoil was also represented by vortex particles. The strength or the shedding rate of the trailing edge vorticity was determined by the unsteady Kutta condition and the conservation of vorticity in the entire flow field. The Rankine vortex model, in which a constant distribution of the vorticity is assumed within the core of the vortex, was used and significant deformation and splitting of the vortex were predicted in a close interaction. The effects of core size

of the vortex on the strength of interaction and severity of vortex deformation were also examined in [63]. However, these methods, derived from the theory of potential flow, have been restricted by shedding vorticity from the trailing edge only, thereby precluding possible flow separation from the surface of the body, either induced by the interaction vortex or resulting from the flow at a high angle of incidence. Also, in these studies, only the normal force distributions during the BVI were given and no comparison was made between the numerical simulation and experimental tests.

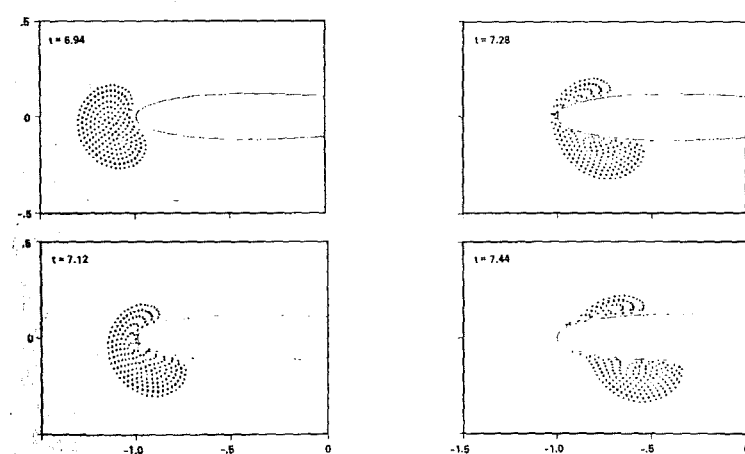


Figure 1.7: Deformation and splitting of the vortex during the head-on interaction predicted by a panel method. From Lee and Smith(1991)

Among others, the grid-based methods have also been used to study the BVI problem. In [41], the incompressible Navier-Stokes equations were solved using the finite difference method for the 2-D BVI problem, but the Reynolds number for the calculation was less than 200 due to the limitation of the method. Later, to reduce the excessive numerical diffusion of the interaction vortex, a high-order space discretization scheme was applied for the convection term in the thin-layer N-S equations[91]. In [50], a 2-D full potential model was used to model parallel BVI in the transonic flow regime. However, as stated in a recent review of helicopter aerodynamics by Conlinsk[27], grid-based methods currently still suffer from diffi-

culties in capturing and subsequently tracking compact vorticity regions, such as the interaction vortex, unless more complicated and time-consuming high order space discretization schemes and self-adaptive grid generation systems are used. Hsu and Wu [45][46] also studied the effect of flow turbulence on the blade-vortex interaction by using a turbulent boundary layer solver. The results for both laminar and turbulent flows suggested that flow turbulence has little effect on the transient normal force development due to the fact that the process of the interaction happens in a very short period of time.

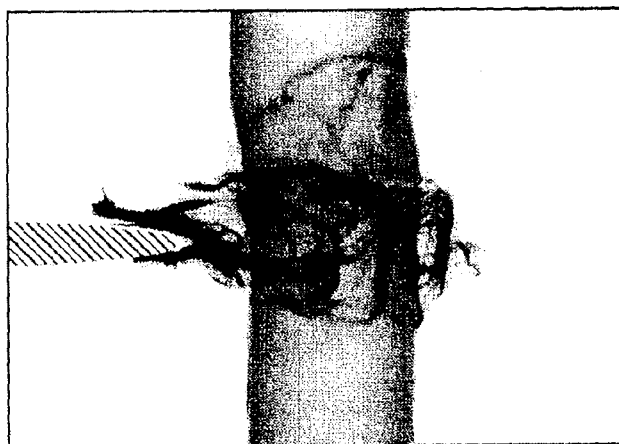


Figure 1.8: Flow visualization of the complex flow field during the normal BVI in the strong vortex regime. From Krishnamoorthy and Marshall(1998)

As to the 3-D normal blade vortex interaction, due to the complexity of the flow problem and a lack of competent computational tools, so far only a very limited number of experimental and numerical studies have been carried out. An experimental study of the normal BVI was reported by Johnston and Sullivan(1992)[49] in which the trailing vortex from a propeller was cut by a blade traversed from downstream. The vortex deformation due to cutting by the blade was visualized by smoke, and the unsteady pressure distribution on the blade surface was measured. Another experimental study of normal BVI was performed by Weigand[118] in

which the response of a vortex ring to a cut normal to the core axis by a thin plate was investigated. The PIV technique was used to measure the axial flow within the vortex core and secondary vortices were found due to vortex-induced boundary layer separation. In some cases, the secondary vortices interact with the nearby ring vortex, which leads to the breakup of the ring and formation of three individual vortex rings. A more recent experimental study of normal BVI in the strong vortex regime[60](fig.1.8) clearly shows the complex flow field of the interaction between the induced second vortex loops and the primary vortex.

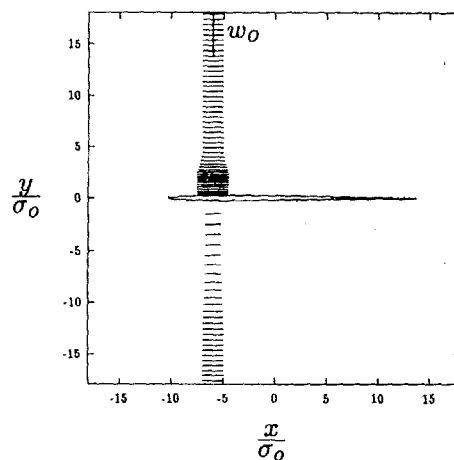


Figure 1.9: Splitting of the vortex filament during a normal BVI predicted by a vortex filament method. From Marshall and Yalamanchill(1994)

In [71], a vortex filament interacting with a rectangular wing of NACA 0016 aerofoil section was simulated numerically by using the long-wave vortex filament model, in which the cutting process of the filament by the blade was not modelled due to the limitation of the method. Instead, the vortex cutting occurs instantaneously during the calculation. It was found that if the thickness of the blade is sufficiently small compared to the core radius of the filament, the vortex does not bend significantly before splitting into two parts. On the other hand, if the body is sufficiently thick relative to the vortex core radius, severe bending of the vortex occurs during

the encounter. To account for the distributed vorticity of the vortex during the interaction, Marshall and Grant[72] recently simulated the interaction between a vortex ring and a finite wing by using a Lagrangian vorticity-based method. The vortex ring was represented by several thousands of vortex particles and the surface of the wing was represented by vorticity panels. The suction force induced by the approaching vortex ring was predicted for the time period represented by the leading edge having penetrated into the majority of the core. In this study, inviscid flow is assumed and no surface vorticity was allowed to be drawn into the flow.

While the above work is mainly concerned with the fluid dynamic aspects of blade vortex interaction, some researchers are more interested in the aeroacoustic aspects of the problem. Lyrintzis[70] provided a good discussion of two acoustic approaches related to BVI. In these approaches, it is necessary to know the surface pressure distribution and the flow field around the blade before an acoustic analysis can be conducted.

1.3 Discrete vortex methods

Over the last few decades, with the advent of computer systems and the steady improvement in their performance(speed, memory size of the CPU, software etc), computational fluid dynamics(CFD) has emerged and rapidly developed as a new tool for the analysis of many fundamental and practical fluid dynamics problems. A straightforward way to solve the governing equations, namely the Navier-Stokes equations, of the fluid flow is by using the Euler description, in which the truncated domain of the entire flow region is overlaid by a grid system and the governing partial differential equations are discretized into a system of algebraic equations in terms of the unknown variables at the grid nodes. These equations then can be solved numerically on a computer by employing relevant boundary conditions, which leads to the prevalent grid-based methods such as finite difference, finite element, finite

volume and spectral methods. On the other hand, the Lagrangian description of the fluid flow is much less used due to the fact that the deformable fluid elements are hard to track in the primitive form of the governing equation and the number of the fluid elements required to represent the entire disturbed flow region is prohibitive. One exception is the discrete vortex method for incompressible fluid flows. In this method, the continuous vorticity field, which is contained within a compact region of the entire fluid flow, is discretized into a collection of vortex elements (vortex points, vortex blobs and vortex sheet for 2-D flow; vortex filament, vortex balls, vortex tiles and vortex sticks etc for 3-D flow). These vortex elements interact with each other in compliance with the Biot-Savart Law and are tracked in the Lagrangian manner, i.e. each vortex element or particle moves with the local velocity and at the same time, the vorticity (circulation) associated with each element changes due to the stretching (for 3-D) and diffusion of the vorticity field. As an alternative numerical technique for simulating unsteady incompressible viscous flow, the discrete vortex method offers the following advantages over grid-based methods and methods in primitive variable form:

1. the use of the vorticity as the dependent variable removes the pressure from the governing equations, i.e. it is eliminated as a dependent variable. Thus, for two-dimensional flow the Navier-Stokes equations are replaced by a set of just two partial differential equations, in place of the three for the velocity components and pressure. Furthermore, for a certain kind of vortex dominated flow, as will be shown in the present study, it is easier to analyze the results by using vorticity dynamics.
2. there is low numerical diffusion compared with the discretization of the convection term in the grid-based method, so it is more suitable for simulating high Reynolds number flows.

3. the method is self-adaptive in the sense that the vortex particles are concentrated only in the limited region with non-zero vorticity where significant velocity gradients evolve.
4. the boundary condition at infinity is exactly satisfied in contrast with the grid-based methods in which the boundary conditions are only given approximately on the boundary of the truncated computational region.
5. it is a grid-free method, so it is particularly attractive for simulating unsteady flow problems and flow with a complex boundary configuration.

Early applications of the discrete vortex method to aerofoils were limited to inviscid flow and 2-D problems, for example the unsteady surface vorticity method, where the vorticity sheds from the trailing edge only or from separation points which are either known a priori or determined by other means[115][116]. In his pioneering work, Chorin(1973)[20] proposed a random walk scheme to simulate viscous diffusion in a study of boundary layer flow problems. In this scheme, the vortex sheets and vortex blobs, which were used to represent the vorticity near the surface and in the wake respectively, move with the local velocity and then are displaced stochastically using the Gaussian probability distribution. The method was later applied to the flows around impulsively-started stationary and rotating circular cylinders (Cheer(1983)[16], Kida et al(1992)[53]). In this method, because the vorticity is shed from the entire surface of the body, flow separation can be simulated as a natural process of the vorticity convection and diffusion. Kim and Flynn(1995)[54] also used this strategy to simulate the flow around two cylinders in tandem with various gaps. The qualitative flow patterns, such as the velocity vector distribution, compared well with the experimental results. Other applications of the discrete vortex method concerned the flow around pitching aerofoils under the condition of dynamic stall which involved the moving body problem and massive flow separation.

Spalart(1982,1988)[108] made the first attempt to study this complex unsteady separated flow using the vortex blobs to represent the entire surface vorticity of the aerofoil. In this scheme new vortices are created at every time step to satisfy the no-penetration boundary condition and the surface pressure distribution is calculated from the vorticity creation rate at the surface. A variant of this approach was developed by Lin and Vezza[69] at Glasgow University, in which a control zone was set up around the aerofoil surface and the vorticity in each panel was further broken down into multiple vortex particles. As a result, smoother surface pressure distributions were obtained and the premature stall phenomenon was avoided. More recently, the code has also been generalized and tested for bluff body problems by Taylor[112]. A similar result for the flow around a pitching aerofoil was also given by Shih et al[106], in which the no-penetration boundary condition was maintained by using mirror vortices.

One disadvantage of the discrete vortex method is the computational cost in evaluating the velocity of vortices via the Biot-Savart law. In this process, each vortex is influenced by all the others(N-body problem), therefore the operation count for this procedure is proportional to the square of the total number of vortices. If the number of the vortices is very large, the calculation time is usually prohibitive for most available computer systems. To reduce this computational cost, Christiansen(1973)[23] used a grid-based finite difference method to solve the Poisson equation for the streamfunction, while vortex particles were still tracked in the Lagrangian manner. This approach is referred to as the vortex-in-cell method and has been widely used for simulating the flow around the impulsively started circular cylinder for a wide range of Reynolds number(Smith and Stanby[107], C.C. Chang[15]). The key disadvantage of this scheme is that it makes the grid-free method once again grid dependent. During the last decade, the fast summation algorithm, based on the expansion of the kernel function in the Biot- Savart formula, has emerged as a

tool to speed up the calculation for N-body problems, including the discrete vortex method. Several methods have been proposed, including the hierarchical code of Appel[2], Barnes and Hut[4], the algorithm based on the multipole expansion of the potential kernel by Greengard and Rokhlin[38], as well as the Laurent series approximation of the singular Biot-Savart formula[32]. More recently, C. Draghicescu and M. Draghicescu[33] developed a more general approach, in which high accuracy is achieved by using high-order Taylor series for both singular and smooth kernels and can be applied directly to the kernel in the Biot-Savart formula in terms of the vortex blobs. All the methods mentioned above employ a hierarchical structure(N-body tree codes) to group the vortices spatially and then approximate the effects induced by relatively distant groups. Thus the particle-particle interaction problem is converted to the particle-box or box-box interaction problems, with the number of direct interactions drastically reduced. Generally, these methods have a complexity of $O(N)$ or $O(N\log N)$ rather than $O(N^2)$, where N is the total number of vortices. These methods have been tested by many researchers for 2-D discrete vortex methods and applied to solve practical flow problems.[39] [85].

Much of the recent development in discrete vortex methods focuses upon finding more accurate schemes for simulating viscous diffusion. Instead of the random walk method which has the shortcomings of slow convergence rate and introducing noise into the calculation, several deterministic methods have been developed for the vortex methods. In [80] and [25] the concept of diffusive velocity has been introduced by defining an equivalent convection velocity for the diffusion process based on the 2-D scalar vorticity transport equation. The application of the method to the flow around a circular cylinder and aerofoil [25] shows that smoother results can be obtained as long as the vortex particles strictly overlap. Another deterministic method called the particle strength exchange(PSE) scheme[59][120] is also suitable for vortex methods, in which the circulations associated with the vortex particles

irregularly distributed in the flow domain are redistributed either by the use of an integral representation for the Laplacian operator or a more complicated formula which is given in [100].

Although, to some extent, the discrete vortex method is successful in 2-D applications, the extension of the method to 3-D flow problems is still at a very early stage of development. There are several reasons which are responsible for this situation. Firstly, in 3-D, vorticity is no longer a scalar; both the vorticity and vector potential (the counterpart of the streamfunction in 2-D) are three-component vectors. So, compared to the 3-D Navier-Stokes equations in the primitive variable form, the vorticity-vector potential form of the Navier-Stokes equation no longer reduces the number of the partial differential equations. Secondly, the use of vortex particles to represent the vorticity field does not guarantee the solenoidality of the vorticity. The effect of this non-physical representation of vorticity on the numerical solution is still uncertain. On the other hand, the filament representation of the vorticity field which automatically satisfies the divergence-free condition also suffers from some limitations. For instance, due to the strong stretching of the flow, regular smoothing or remeshing of the filament representation is needed, and it is not easy to use filaments to represent the surface vorticity and its subsequent shedding into the wake due to the convection and diffusion of the vorticity field. Finally, the computational cost for a 3-D calculation is far higher than its 2-D counterpart, because generally, a much larger number of vortices is required for an accurate simulation of the vortical flow.

So far, applications of the 3-D vortex method are mostly restricted to unbounded flow problems such as wake flow and the interaction between vortex rings. Comprehensive reviews of the 3-D vortex method were given in [66] and [120] for the filament method and vortex particle method respectively, in which the advantages and disadvantages of each method were discussed in detail. In [120], some new devel-

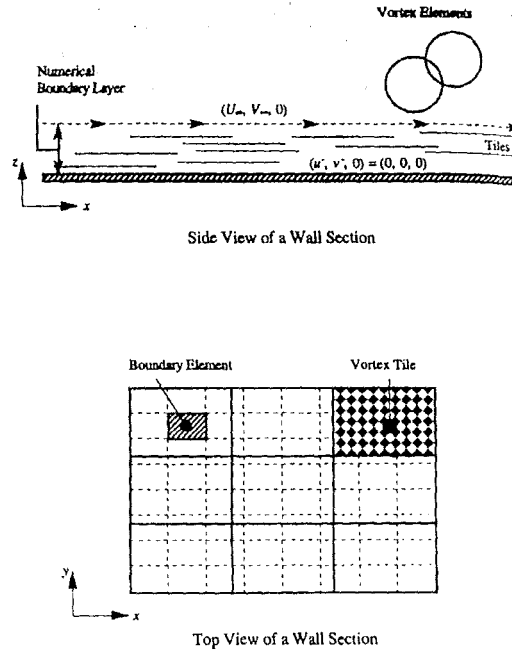


Figure 1.10: Boundary elements and vortex tiles used on surface in 3-D discrete vortex method. From Gharakhani(1997)

opments of the 3-D vortex particle method were also reported; a transpose scheme was put forward for the stretching term which has better properties in terms of the conservation of the total vorticity and the linear moment of vorticity of the flow, a new scheme was devised for the relaxation of the divergence-free condition of the vorticity field, and the interaction and fusion of two vortex rings was calculated in the study to show the ability of the vortex particle method with the inclusion of viscous diffusion by using the PSE scheme. During the course of the present study, several attempts to model the flow around a 3-D body such as a sphere and a cube have also emerged[35][37], in which the surface vorticity has been modelled by vortex tiles which are transformed to vortex points as they move away from the surface, see fig.1.10. In these calculations, only the qualitative results for starting flow have been given, which highlights the remaining problems in producing accurate long time calculations. At this stage it can be claimed that the most difficult

aspect in the 3-D vortex method, i.e. the representation and discretisation of the surface vorticity and its further shedding into the wake without destroying either the divergence-free condition of the vorticity field or the boundary conditions at the surface of body, remains unresolved.

As to the application of the fast summation algorithm in 3-D flow problems, a systematic study on the multipole expansion method was carried out by Pringle[85], in which the vortex ring with a finite core radius was used to examine the performance of the algorithm, and the parallelization of the code was also discussed and implemented.

At this stage, the problems with the discrete vortex methods can now be outlined as follows. Firstly, after some period of evolution of the vortices, the particle distribution may become uneven, thus destroying the overlapping condition which necessitates a remeshing process[59]. In addition, a large number of vortices are needed to capture the fine flow structure near the surface of the body. Secondly, it is not straightforward to include viscous effects, including turbulence, in the calculation, although some developments have been made recently[100]. Lastly, it is not clear how best to extend the method to 3-D flow problems due to the fact, among others, that the vortex particle representation in 3-D is not divergence free. These problems or difficulties in the discrete vortex method have prompted the development of a new vorticity-based method in the present study. The main points of the method are that, firstly, by solving the vorticity transport equation using the finite volume method and calculating velocity using a modified Biot-Savart law, only the flow region with non-zero vorticity needs to be solved. Secondly, during the calculation, mass and vorticity conservation can be guaranteed by using this approach together with the method of implementing the surface boundary conditions. Thirdly, high accuracy in capturing fine vortex structures can be achieved by accommodating either structured or unstructured meshes. Finally, the extension of

the method to 3-D problems is straightforward.

1.4 The scope of the present study

The present work mainly consists of four parts. In the first part, the 2-D parallel blade-vortex interaction problem is systematically studied by using a two-dimensional discrete vortex code, which was originally developed within the Department for simulating dynamic stall of a pitching aerofoil[69]. In this method, the entire vorticity region including the oncoming vortex is represented by a finite number of vortex blobs (particles with finite core radius) which are tracked through the flow according to the local velocity calculated from the Biot-Savart law. The effect of viscous diffusion is modelled by the random walk method. The surface of the aerofoil is represented by the panel method and at each time step, to satisfy the relevant boundary conditions, new vortices are introduced along the surface which are, in part or in whole, allowed to enter the wake from the entire surface depending on the convection and diffusion of the local flow. This feature of the method therefore makes it possible to simulate flow separation without the need for either a Kutta condition to calculate the vorticity shedding rate at the trailing edge and at separation points, or empirical methods to determine the separation points.

To adapt the code to the present study, routines have been written for the discretization of the interaction vortex using the Scully vortex model and to incorporate other necessary changes for the inclusion of the oncoming vortex or vortices. To reduce the total number of vortex particles in the flow field, a different, usually larger, core radius is used when discretising the interaction vortex than that employed for the vortices shed from the aerofoil surface. A new scheme has been implemented to calculate the velocity of nascent vortices to avoid the possible oscillation of its normal component. To speed up the calculation, a fast adaptive summation algorithm [32] [113] based on the Laurent series of the singular kernel function in the Biot-

Savart formula has been integrated into the code, which enables a large number of particles to be used in the calculation.

A systematic study of BVI has been carried out by using the modified discrete vortex code. The dominant mechanisms of a blade interacting with a single vortex are clearly revealed through the illustration of the unsteady surface pressure distribution and the loads, as well as the trajectory of the interaction vortex. The effects of some parameters, such as the initial vertical position and the core size of the vortex, as well as the pitching angle of the aerofoil, on the strength of the interaction are examined. Some phenomena associated with a close strong interaction, such as the deformation and splitting of the interaction vortex, and the vortex-induced boundary layer separation, are predicted and illustrated, and wherever possible, the results are compared with either other numerical results or experimental results from the wind tunnel BVI tests at Glasgow University. Some ambiguities in the previous study concerning the vortex convection velocity during the interaction are clarified by analysing the mutual interaction of the oncoming vortex and the induced surface vorticity.

The results for the interaction between a twin vortex system and a blade are also presented. Due to the fact that two vortices separated by some distance in space is an unstable system in which a slow rotation around their common center occurs strong deformation and even amalgamation of the twin vortex may happen before they encounter the aerofoil, depending on the initial relative position. Hence, the effects of the initial condition of the twin vortex on the BVI event are examined.

In the second part of the present work, preliminary studies of the interaction between a vortex ring and both a finite wing of NACA 0016 aerofoil section and a sphere are conducted by using a 3-D vortex particle method. The vortex ring is represented by a large number of vortex particles and the body surface is discretised into more than one thousand source panels. To better represent the body surface

and calculate more accurately the velocity of vortex particles near the surface, each panel is further divided into multiple subpanels with local curvatures instead of the planar panels. The forces exerted on the body are calculated from a vorticity-based global method and the results are compared with a similar calculation using a slightly different discrete vortex approach.

Some efforts have also been made in constructing a general 3-D vortex particle code to model complex 3-D flow problems. As a first step, in this study, a fast summation algorithm based on the domain decomposition and Taylor expansion of the kernel function in the 3-D Biot-Savart law is implemented. The advantages of this approach are that the expansion can be directly conducted on the velocity expression and it is also much simpler than the multipole expansion method in mathematical formulation. Some details on the algorithm are discussed, including the derivation of the recurrence relations of the coefficients in the Taylor series and the domain decomposition method. The performance of the algorithm, e.g. the breakeven point, the speed-up ratio and the accuracy of the method, is tested by calculating the viscous interaction of two vortex rings. Finally some problems in developing a 3-D vortex code are discussed and analysed.

In the final part of the study, a novel vorticity-based method has also been developed for unsteady aerodynamic problems. In this method, the vorticity transport equation in conservative form is solved by the cell-centred finite volume method, while the velocities needed at the centre of each control volume are calculated by using a modified Biot-Savart formula in conjunction with an adaptive fast summation algorithm. The method employed to implement the boundary conditions and to calculate the vorticity creation at the body surface ensures both the mass and vorticity are conserved during the calculation. This, along with the inherent conservative property of the finite volume method, guarantees the conservation of vorticity in the entire flow. A detailed description of the numerical implementation of the

method, including the fast summation algorithm and implementation of the boundary conditions are presented. By calculating the unsteady flow around a circular cylinder at various Reynolds numbers, the accuracy and efficiency of the method are demonstrated. Further development of the method, particularly in the application of the method to the vortex-body interaction problems, will also be discussed.

1.5 Layout of the thesis

In chapter 2, the theoretical background of both the 2-D and 3-D discrete vortex methods is reviewed, starting with the governing equations for incompressible flow in both the primitive variable form and in the velocity-vorticity form, and the boundary conditions that are needed for solving the governing equations. The generalised Biot-Savart Law, which is the basis of the discrete vortex method, is then introduced by using the Green's theorem. The conservation law of the vorticity field as well as the basic procedure for constructing the vorticity-based methods are also discussed in this chapter.

In chapter 3, the numerical implementation of the vortex method is presented in the context of the blade-vortex interaction problem, which includes the methods for discretizing the oncoming vortex, aerofoil and wing surfaces, and the evolution of the discrete vortex system using the Biot-Savart law. The effects of some parameters such as the core size of the vortices and the overlapping condition of the vortices are also examined. Then some details on the implementation of both 2-D and 3-D fast algorithms are given, along with some new developments of the discrete vortex method in the present study.

The results for 2-D blade vortex(single and twin) interaction and the 3-D vortex ring body(wing) interaction are demonstrated and discussed in chapter 4. In chapter 5, some details on implementation and performance of a fast summation algorithm for 3-D vortex particle methods are discussed.

In chapter 6, a detailed description of the new vorticity-based method will be given, including its implementation and numerical tests. This is followed by conclusions from the study and suggestions for further development of the vorticity-based method, with possible applications in vortex-body interaction problems presented in chapter 7.

Chapter 2

Theoretical Background of Vortex Methods

2.1 Governing equations and boundary conditions

The 3-D incompressible unsteady viscous flow can be described by the following vector form of the Navier-Stokes equations which are derived from the conservation laws of mass and momentum respectively:

Continuity equation:

$$\nabla \cdot \mathbf{u} = 0 \quad (2.1)$$

Momentum equation:

$$\frac{\partial \mathbf{u}}{\partial t} + (\mathbf{u} \cdot \nabla) \mathbf{u} = -\frac{\nabla p}{\rho} + \nu \nabla^2 \mathbf{u} \quad (2.2)$$

where $\mathbf{u} = [u, v, w]^T$ is the velocity vector, p the pressure, ρ the density of the fluid which is a constant for incompressible flow, and ν the kinematic viscosity. After using the vector identity

$$\mathbf{u} \times (\nabla \times \mathbf{u}) = \frac{1}{2}(\mathbf{u} \cdot \nabla) \mathbf{u} - (\mathbf{u} \cdot \nabla) \mathbf{u} \quad (2.3)$$

equation (2.2) can be written as

$$\frac{\partial \mathbf{u}}{\partial t} - \mathbf{u} \times (\nabla \times \mathbf{u}) = -\nabla \left(\frac{p}{\rho} + \frac{1}{2} \mathbf{u} \cdot \mathbf{u} \right) + \nu \nabla^2 \mathbf{u} \quad (2.4)$$

By taking the curl of both sides of equation (2.4), the transport equation for vorticity, defined by $\omega = \nabla \times \mathbf{u}$, can be obtained as

$$\frac{d\omega}{dt} = \omega \cdot \nabla \mathbf{u} + \nu \nabla^2 \omega \quad (2.5)$$

in which use has been made of the identity

$$\nabla \times (\mathbf{u} \times \omega) = \omega \cdot \nabla \mathbf{u} - \mathbf{u} \cdot \nabla \omega + \mathbf{u}(\nabla \cdot \omega) - \omega(\nabla \cdot \mathbf{u}) \quad (2.6)$$

and the auxiliary relations $\nabla \cdot \mathbf{u} = 0$ and $\nabla \cdot \omega = 0$. Thus, the governing equations (2.1) and (2.2) have been transformed into their equivalent form represented by the vorticity transport equation, the definition of vorticity and the continuity equation.

Because the velocity field is divergence-free, another vector Ψ , called the vector potential, can be introduced with the definition:

$$\mathbf{u} = \nabla \times \Psi \quad (2.7)$$

Inserting this equation into the definition of the vorticity and assuming that the vector potential itself is divergence-free, i.e. $\nabla \cdot \Psi = 0$, a Poisson equation for Ψ with ω as the source term is obtained as

$$\nabla^2 \Psi = -\omega \quad (2.8)$$

Now, by using equations (2.5) and (2.8), the governing equations for incompressible flow have been represented in the vorticity(ω)-vector potential(Ψ) form.

For the problem of flow around a closed body, the boundary conditions needed for solving the governing equations consist of two parts, both of which are given in terms of velocity. One is the so called far field condition in which the free-stream condition is applied at infinity:

$$\mathbf{u} = \mathbf{u}_\infty \quad (2.9)$$

The other is the condition on the body surface where the no-slip and no-penetration conditions are used:

$$\mathbf{u} = \mathbf{u}_b(\mathbf{x}_s, t) \quad (2.10)$$

where $\mathbf{u}_b(\mathbf{x}_s, t)$ represents the velocity at body surface. For a solid body translating with velocity $\mathbf{u}_{bt}(t)$ and rotating around a fixed point \mathbf{o} with angular velocity $\Omega(t)$, the surface velocity at point \mathbf{x}_s , $\mathbf{u}_b(\mathbf{x}_s, t)$, is given by

$$\mathbf{u}_b(\mathbf{x}_s, t) = \mathbf{u}_{bt}(t) + \Omega(t) \times (\mathbf{x}_s - \mathbf{x}_o) \quad (2.11)$$

For unsteady flow problems, the initial conditions are also required to start the calculation. This is achieved by either assuming that the flow starts impulsively from rest or prescribing the velocity or vorticity distribution in the flow field.

If the flow is two dimensional, where $\mathbf{u} = (u, v, 0)^T$ and $\frac{\partial u}{\partial z} = \frac{\partial v}{\partial z} = 0$, the governing equations have a simpler form. Firstly, the vorticity ω only has one non-zero component, $\omega = (0, 0, \omega)^T$; secondly, the vector potential Ψ can be replaced by a scalar streamfunction ψ with the definition $u = -\frac{\partial \psi}{\partial y}$, $v = \frac{\partial \psi}{\partial x}$. Accordingly, the transport equation for the non-zero component of vorticity is

$$\frac{d\omega}{dt} = \nu \nabla^2 \omega \quad (2.12)$$

and the continuity equation in the form of the Poisson equation for the streamfunction ψ is reduced to

$$\nabla^2 \psi = -\omega \quad (2.13)$$

By examining equations (2.5) and (2.8) and comparing them with equation (2.12) and (2.13), several points can be made. Firstly, by introducing the concept of vorticity into the flow description, the pressure term is eliminated from the governing equations of the fluid flow. Secondly, for 3-D flow problems, development of the vorticity field is not only affected by the viscous diffusion, but also by the velocity

gradients of the flow field, i.e. the term $\nabla \mathbf{u}$. It is well known that this term can be decomposed into two parts: $\nabla \mathbf{u} = D + S$, where the symmetric tensor $D = \frac{\nabla \mathbf{u} + \nabla \mathbf{u}^T}{2}$ is called the deformation tensor and $S = \frac{\nabla \mathbf{u} - \nabla \mathbf{u}^T}{2}$ is a skew-symmetric tensor corresponding to the rigid body rotation of the fluid. Thus, $\omega \cdot \nabla \mathbf{u} = \omega \cdot D + \omega \cdot S$. However, it is easy to check that $\omega \cdot S = \frac{1}{2} \omega \times \omega = 0$, so $\omega \cdot \nabla \mathbf{u} = \omega \cdot D$, which means that only the deformation (stretching and tilting) term of the velocity gradients contributes to the change of the vorticity vector (magnitude and orientation). Furthermore, from the last equation, it is readily shown that $\omega \cdot \nabla \mathbf{u} = \omega \cdot \nabla^T \mathbf{u}$, where $\nabla^T \mathbf{u}$ is the transpose of $\nabla \mathbf{u}$. This fact is the basis of the transpose scheme which will be used in the 3-D vortex particle method. Finally, in 2-D flows, because the stretching term no longer exists, the vorticity is only affected by viscous diffusion.

Another important fact about the vorticity field is that, by definition, the vorticity field is divergence-free, i.e. $\nabla \cdot \omega = 0$, which implies that the vorticity is conserved. In fact, it can be shown that for a general incompressible flow around a rotating body, the total vorticity in both the fluid region and the solid body is a constant at any instant of time:

$$\int_{vf} \omega \, d\mathbf{x} + \int_{vb} \omega \, d\mathbf{x} = \omega_o \quad (2.14)$$

or

$$\frac{d}{dt} \int_{vf+vb} \omega \, d\mathbf{x} = 0 \quad (2.15)$$

where vf and vb represent the fluid region and the solid body region respectively, and $\omega = 2\Omega(t)$ in the region of solid body. The constant ω_o represents the initial total vorticity in the fluid region from sources other than the body surface. The law of vorticity conservation sometimes is useful in construction of numerical algorithms.

For inviscid flow, the conservation of vorticity sometimes can also be expressed in a more specific way, such as by Kelvin's circulation theorem and Helmholtz's

theorem. As an important special case, for 2-D inviscid flow, the vorticity is simply carried along, unchanging, with the fluid particles.

2.2 Generalised Biot-Savart law

For unbounded flow in an otherwise motionless fluid, the Poisson equation for the vector potential Ψ can be solved by means of the Green's function approach. In 3-D, the Green's function which satisfies the equation $\nabla^2 G = -\delta(\mathbf{x} - \mathbf{x}')$ with δ the Dirac delta function, is

$$G(\mathbf{x}, \mathbf{x}') = \frac{1}{4\pi |\mathbf{x} - \mathbf{x}'|} \quad (2.16)$$

So, we have

$$\Psi(\mathbf{x}) = \int_v G(\mathbf{x}, \mathbf{x}') \omega(\mathbf{x}') dv(\mathbf{x}') \quad (2.17)$$

where the volume integral is taken over the entire vortical region.

Thus, the velocity, which is the curl of the vector potential, can be calculated from the following formula:

$$\mathbf{u}(\mathbf{x}) = \nabla \times \Psi = \frac{1}{4\pi} \nabla \times \int_v \frac{\omega}{|\mathbf{x} - \mathbf{x}'|} dv(\mathbf{x}') = \frac{1}{4\pi} \int_v \frac{\omega(\mathbf{x}') \times (\mathbf{x} - \mathbf{x}')}{|\mathbf{x} - \mathbf{x}'|^3} dv(\mathbf{x}') \quad (2.18)$$

Suppose that we have a vortex line C in space with circulation Γ and we assume that the vorticity is concentrated on C only, i.e. the flow is potential outside the filament C , then the velocity induced by the vortex filament is

$$\mathbf{u}(\mathbf{x}) = \frac{1}{4\pi} \int_C \frac{\mathbf{s}(\mathbf{x}' - \mathbf{x})}{|\mathbf{s}(\mathbf{x}' - \mathbf{x})|^3} \times \Gamma ds(\mathbf{x}') \quad (2.19)$$

where ds is the line element on C . This formula has the same form as the Biot-Savart law which is used in magnetostatics for calculating the induced magnetic field from the electric current. By analogy, equation 2.18 is also called the Biot-Savart formula for distributed vorticity in the context of fluid dynamics.

For 2-D flow, the Green function for the Laplace operator ∇^2 is

$$G(\mathbf{x}, \mathbf{x}') = \frac{1}{2\pi} \ln\left(\frac{1}{|\mathbf{x} - \mathbf{x}'|}\right) \quad (2.20)$$

and accordingly, the streamfunction and the velocity induced by the vorticity distribution ω can be expressed as

$$\psi(\mathbf{x}) = \frac{1}{2\pi} \int \omega(\mathbf{x}') \ln(|\mathbf{x} - \mathbf{x}'|) ds(\mathbf{x}') \quad (2.21)$$

$$\mathbf{u} = \frac{1}{2\pi} \mathbf{k} \times \nabla \psi(\mathbf{x}) \quad (2.22)$$

$$= \frac{1}{2\pi} \mathbf{k} \times \int \frac{\mathbf{x} - \mathbf{x}'}{|\mathbf{x} - \mathbf{x}'|^2} \omega(\mathbf{x}') ds(\mathbf{x}') \quad (2.23)$$

For the flow around a body or bodies, however, the boundary conditions also make contributions to the velocity calculation. With the aid of Green's theorem for vectors, the contribution from the freestream, movement of the body surface and the vorticity in the flow field to the velocity at point \mathbf{x} in the fluid region is [123]

$$\begin{aligned} \mathbf{u}(\mathbf{x}) &= \mathbf{u}_\infty + \int_v f \omega(\mathbf{x}') \times \nabla_{\mathbf{x}'} G(\mathbf{x}, \mathbf{x}') dv(\mathbf{x}') \\ &- \int_{bs} \{(\mathbf{n} \times \mathbf{u}(\mathbf{x}')) \times \nabla_{\mathbf{x}'} G(\mathbf{x}, \mathbf{x}') + (\mathbf{n} \cdot \mathbf{u}(\mathbf{x}')) \nabla_{\mathbf{x}'} G(\mathbf{x}, \mathbf{x}')\} ds(\mathbf{x}') \end{aligned} \quad (2.24)$$

where the surface integral is taken over the body surface. This formula is usually called the generalized Biot-Savart law or Poincare formula in some references. By noticing that $\nabla_{\mathbf{x}'} G(\mathbf{x}, \mathbf{x}') = -\nabla_{\mathbf{x}} G(\mathbf{x}, \mathbf{x}')$, the above equation can also be written as

$$\begin{aligned} \mathbf{u}(\mathbf{x}) &= \mathbf{u}_\infty + \nabla_{\mathbf{x}} \times \int_v f \omega(\mathbf{x}') G(\mathbf{x}, \mathbf{x}') dv(\mathbf{x}') \\ &+ \nabla_{\mathbf{x}} \times \int_{bs} (\mathbf{n} \times \mathbf{u}) G(\mathbf{x}, \mathbf{x}') ds(\mathbf{x}') - \nabla_{\mathbf{x}} \int_{bs} (\mathbf{n} \cdot \mathbf{u}) G(\mathbf{x}, \mathbf{x}') ds(\mathbf{x}') \end{aligned} \quad (2.25)$$

which indicates that the vector potential cannot be expressed explicitly from the vorticity in the flow region and the boundary conditions at the body surface for a general flow problem due to the presence of the scalar gradient term.

It is easy to show by using vector identities that, for a closed rigid body, the surface integral in the above formula can be transformed into the volume integral over the region inside the solid body, i.e.

$$\begin{aligned}
& - \int_{bs} \{ (\mathbf{n} \times \mathbf{u}(\mathbf{x}')) \times \nabla_{\mathbf{x}'} G(\mathbf{x}, \mathbf{x}') + (\mathbf{n} \cdot \mathbf{u}(\mathbf{x}')) \nabla_{\mathbf{x}'} G(\mathbf{x}, \mathbf{x}') \} ds(\mathbf{x}') \\
& = \int_{vb} \omega(\mathbf{x}') \times \nabla_{\mathbf{x}'} G(\mathbf{x}, \mathbf{x}') dv(\mathbf{x}') \tag{2.26}
\end{aligned}$$

where $\omega(\mathbf{x}') = 2\Omega(t)$. A proof of this is given in Appendix B. Thus, equation (2.24) can be represented by the volume integral only

$$\mathbf{u}(\mathbf{x}) = \mathbf{u}_\infty + \int_{vf+vb} \omega(\mathbf{x}') \times \nabla_{\mathbf{x}'} G(\mathbf{x}, \mathbf{x}') dv(\mathbf{x}') \tag{2.27}$$

which means that the velocity at any point in the fluid region can be calculated explicitly from the vorticity field in both regions, namely fluid and rotating solid body. Because the rotation velocity in a solid body $\Omega(t)$, is independent of the spatial variables, it can be taken to the outside of the integral, which then becomes much simpler for some applications. However, equation (2.24) is still useful for some special cases in which the movement of the boundary is caused by deformation of the body. From equation (2.27), it also can be shown that the boundary condition at infinity is exactly satisfied because the volume integral has no contribution to the velocity field at a point far away from the body surface.

For two dimensional flow, similar results can be obtained for the streamfunction and the velocity. In fact, a unified expression for the velocity in both 2-D and 3-D flow has been given by equations (2.24) and (2.27), in which G is the 2-D and 3-D Green function respectively.

2.3 Construction of vorticity-based method

It is well known that for incompressible viscous flow, the vorticity can only be generated at the surface of the body due to the no-slip boundary condition. The vorticity in the interior of the fluid domain, which in turn determines the velocity field through the Biot-Savart law, is the consequence of diffusion and convection of the boundary vorticity.

By using equations (2.5) and (2.27), which represent the kinematic and kinetic aspects of the entire flow problem respectively, vorticity-based methods, including the discrete vortex method, can be constructed. The kinematic step determines the velocity field induced by the vorticity distribution and relevant boundary conditions, while the kinetic step redistributes the vorticity within the flow domain by vorticity convection and diffusion. In the real world, these two steps should happen simultaneously, however, in the numerical procedure, it is reasonable to assume that the following three steps are needed to advance the solution to a new time level:

1. vorticity generation and its subsequent discretization into vortices near the body surface by using equation (2.27) and implementing the relevant boundary conditions. This process usually leads to a system of linear algebraic equations with the surface vorticity values as the unknowns.
2. calculation of the velocity and its derivatives with respect to the space variables using the Biot-Savart Law.
3. the transport of vortex elements according to the local velocity of the flow and the stretching and diffusion of the vorticity field in the flow domain.

After step (3), the boundary conditions at the body surface are usually violated, and we need to return to the first step to determine the boundary vorticity for the next time step by imposing the boundary conditions.

These ideas, which are based on the vorticity dynamics and the Biot-Savart law, have been extensively used by some researchers for simulating 2-D unsteady incompressible flows by coupling a finite difference method to solve the vorticity transport equation[122].

In the context of the vorticity representation of fluid flow, it has been shown that either the no-penetration condition or the no-slip condition can uniquely determine the velocity field in the entire flow domain. So, for the purpose of calculating the surface vorticity distribution, either condition can be implemented, which will be discussed further in the next chapter.

From the above discussion, it is clear that the generalized Biot-Savart formula plays a key role in constructing vortex methods. It is needed not only for calculating the velocity in the flow field, but also for determining the surface vorticity distribution by satisfying boundary conditions. The latter process can be considered an inverse problem in the sense that the boundary vorticity is calculated from the interior part of the vorticity field which contradicts the usual procedure in which the flow variables in the interior of the fluid domain are determined from the boundary variables.

In the next chapter, a detailed discussion will be given on how to implement these ideas into a computational tool, i.e. the discrete vortex method, by using a large number of vortex particles to represent the continuous vorticity field.

Chapter 3

Implementation of the Discrete Vortex Method

3.1 Two dimensional case

3.1.1 Discretization and evolution of vorticity field

Traditionally, in the studies of potential flow with embedded viscous region, surface vorticity panels and point vortices have been employed to represent the vorticity distribution in the thin layers of fluid surrounding a body and in the wake respectively. One example of such an approximation is the study of the wake flow of a bluff body, in which the vorticity in the wake is represented by two rows of point vortices (von Karman vortex street).

More generally, in point-vortex methods, the vorticity in a fluid is assumed to be concentrated in N_v vortices, located at \mathbf{x}_j , $j = 1, 2, \dots, N_v$, with circulations Γ_j and nominally, the vorticity field can then be represented by the sum of the point vortices:

$$\omega(\mathbf{x}) = \sum_{j=1}^{N_v} \Gamma_j \delta(\mathbf{x} - \mathbf{x}_j) \quad (3.1)$$

where δ is the 2-D Dirac function.

Inserting equation 3.1 into equations 2.21 and 2.23, one obtains the streamfunc-

tion and the velocity distribution induced by the point vortices:

$$\psi(\mathbf{x}) = -\frac{1}{2\pi} \sum_{j=1}^{N_v} \Gamma_j \ln |\mathbf{x} - \mathbf{x}_j| \quad (3.2)$$

$$\mathbf{u}(\mathbf{x}) = \frac{1}{2\pi} \mathbf{k} \times \sum_{j=1}^{N_v} \Gamma_j \frac{\mathbf{x} - \mathbf{x}_j}{|\mathbf{x} - \mathbf{x}_j|^2} \quad (3.3)$$

For inviscid flow, the evolution of the vortex system can be described by the conservation of vorticity and the movements of vortex particles with local velocities:

$$\frac{d\Gamma_j}{dt} = 0 \quad (3.4)$$

$$\frac{d\mathbf{x}_j}{dt} = \mathbf{u}(\mathbf{x}_j, t) \quad (3.5)$$

However, the vorticity field represented by equation 3.1 is singular in the sense that the self-induced velocity of a point vortex is infinite. So in the actual calculation of the velocity for a vortex located at \mathbf{x}_j , the self-induced contribution should be omitted from the sum. The other drawback of the point vortex model is that the vorticity field is neither smooth nor continuous, which is a bad approximation of the real vorticity distribution.

So, in the non-singular version of discrete vortex methods, the continuous vorticity field is approximated by a set of overlapping vortex blobs (particles with a finite core radius σ):

$$\omega(\mathbf{x}) = \sum_{j=1}^{N_v} \Gamma_j \delta_\sigma(\mathbf{x} - \mathbf{x}_j) \quad (3.6)$$

where Γ_j is the strength (circulation) of the vortex particle located at \mathbf{x}_j and the smooth core function $\delta_\sigma(\mathbf{x} - \mathbf{x}_j)$ is usually radially symmetric, i.e. $\delta_\sigma(\mathbf{x} - \mathbf{x}_j) = \frac{1}{\sigma^2} f\left(\frac{|\mathbf{x} - \mathbf{x}_j|}{\sigma}\right)$ and $2\pi \int_0^\infty r f(r) dr = 1$. Mathematically, it has been shown that vortex blob methods converge to the smooth Euler solutions as long as vortices are overlapped, i.e. the core radius σ of a vortex should be the order of or greater than the distance between neighbouring vortices.

In accordance with the vorticity distribution represented by equation 3.6, the velocity at any point \mathbf{x} in the flow field, particularly at the center of each particle \mathbf{x}_j , can be calculated using the Biot-Savart law, which gives

$$\mathbf{u}(\mathbf{x}) = \frac{1}{2\pi} \mathbf{k} \times \sum_{j=1}^{N_v} \Gamma_j \frac{\mathbf{x} - \mathbf{x}_j}{|\mathbf{x} - \mathbf{x}_j|^2} F\left(\frac{|\mathbf{x} - \mathbf{x}_j|}{\sigma}\right) \quad (3.7)$$

where F is defined by $F(r) = 2\pi \int_0^r r' f(r') dr'$. Correspondingly, streamfunction ψ is

$$\psi(\mathbf{x}) = -\frac{1}{2\pi} \sum_{j=1}^{N_v} \Gamma_j \bar{F}\left(\frac{|\mathbf{x} - \mathbf{x}_j|}{\sigma}\right) \quad (3.8)$$

with \bar{F} defined by $\bar{F} = \int_0^r \frac{F(r')}{r'} dr'$.

A number of choices are available in selecting the core function, such as the Gaussian and Rankine models. The former can be expressed as

$$f(r) = \frac{1}{2\pi\sigma^2} e^{-\frac{r^2}{2\sigma^2}}$$

and the induced velocity distribution by the vortex is

$$u(r) = \frac{\Gamma}{2\pi r} (1 - e^{-\frac{r^2}{2\sigma^2}})$$

The Rankine vortex model is described by

$$f(r) = \begin{cases} \frac{1}{\pi\sigma^2} & \text{if } r \leq \sigma \\ 0 & \text{if } r > \sigma \end{cases}$$

and correspondingly, the velocity distribution is

$$u(r) = \begin{cases} \frac{\Gamma r}{2\pi\sigma^2} & \text{if } r \leq \sigma \\ \frac{\Gamma}{2\pi r} & \text{if } r > \sigma \end{cases}$$

However, in the present study, a simple vortex core, which is usually referred to as the Scully model with

$$f(r) = \frac{1}{\pi} \frac{\sigma^2}{(\sigma^2 + r^2)^2}$$

and

$$u(r) = \frac{\Gamma}{2\pi} \frac{r}{\sigma^2 + r^2}$$

has been implemented. In figure 3.1, various vortex models and induced velocity distributions are plotted for comparison.

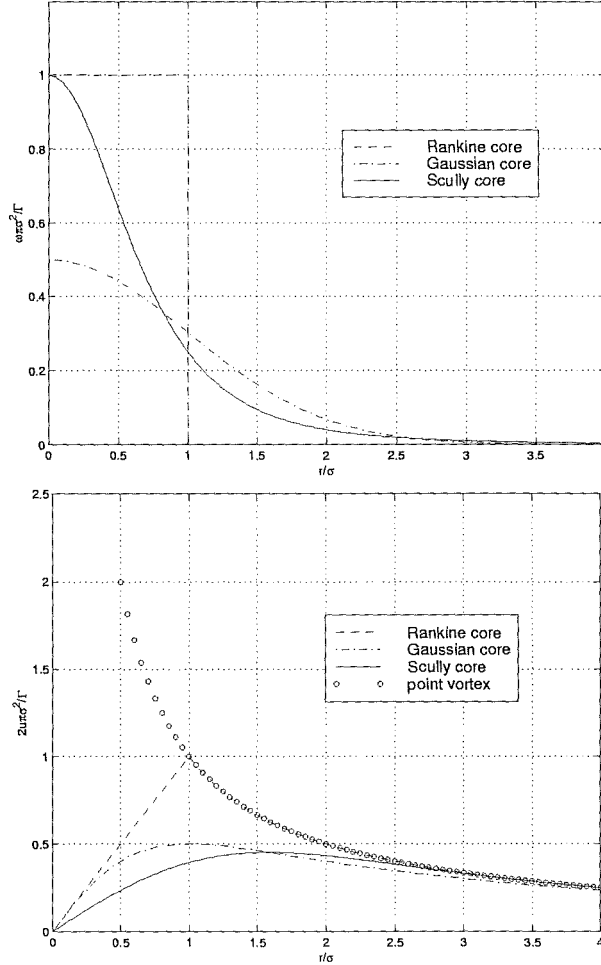


Figure 3.1: Vorticity and velocity distributions for various 2-D core functions

More specifically, for Scully vortex model, equations 3.7 and 3.8 can be given by

$$\mathbf{u}(\mathbf{x}) = \frac{1}{2\pi} \mathbf{k} \times \sum_{j=1}^{N_v} \Gamma_j \frac{\mathbf{x} - \mathbf{x}_j}{(|\mathbf{x} - \mathbf{x}_j|^2 + \sigma^2)} \quad (3.9)$$

$$\psi(\mathbf{x}) = -\frac{1}{4\pi} \sum_{j=1}^{N_v} \Gamma_j \ln(|\mathbf{x} - \mathbf{x}_j|^2 + \sigma^2) \quad (3.10)$$

At each time step, by convecting each vortex with the local velocity using the Euler first order or the Adams-Bashforth second order scheme and applying the random walk method [20] to mimic the effects of viscous diffusion, the new position of the vortex at \mathbf{x}_j after time interval Δt is given by

$$\mathbf{x}_j(t + \Delta t) \simeq \mathbf{x}_j(t) + \mathbf{u}(\mathbf{x}_j, t)\Delta t + \eta_j \quad (3.11)$$

or

$$\mathbf{x}_j(t + \Delta t) \simeq \mathbf{x}_j(t) + \Delta t \left[\frac{3}{2}\mathbf{u}(\mathbf{x}_j, t) - \frac{1}{2}\mathbf{u}(\mathbf{x}_j, t - \Delta t) \right] + \eta_j \quad (3.12)$$

where η_j are a pair of independent random variables with zero mean and variance $2\nu\Delta t$. Equation 3.4 is unchanged, i.e. circulation is conserved.

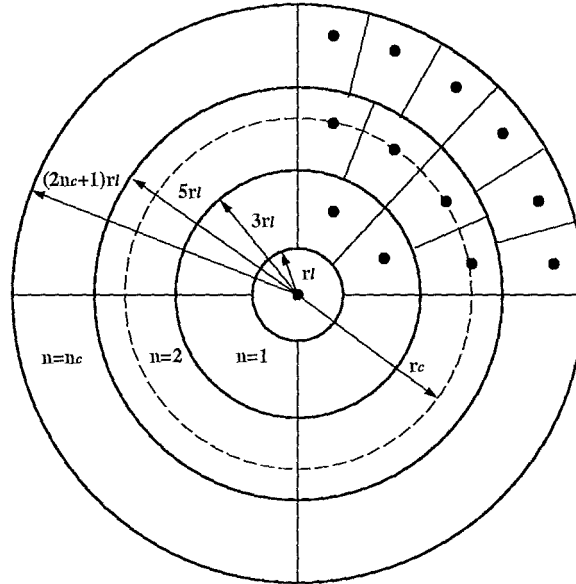


Figure 3.2: Discretisation of the core of the interaction vortex using vortex particles:
 $r_c = r_l \frac{1+12n^2}{6n}$

For the problem of blade vortex interaction, the entire vorticity in the flow field comes from two sources; the interaction vortex which is released into the flow from upstream of the aerofoil and the aerofoil surface where the new vorticity is created at each time step. Figure 3.2 shows how the initial vorticity field of the interaction vortex is discretised into a number of discrete vortex particles by overlaying the

vortex with a system of patches of equal area $A = \pi r_l^2$. Each vortex particle is placed at the centroid \mathbf{r}_c of the patch and has strength $\Gamma = \omega(\mathbf{r}_c) \cdot A$. The core radius of the discrete vortices ensures overlapping cores, i.e. $\sigma/r_l \geq 1$.

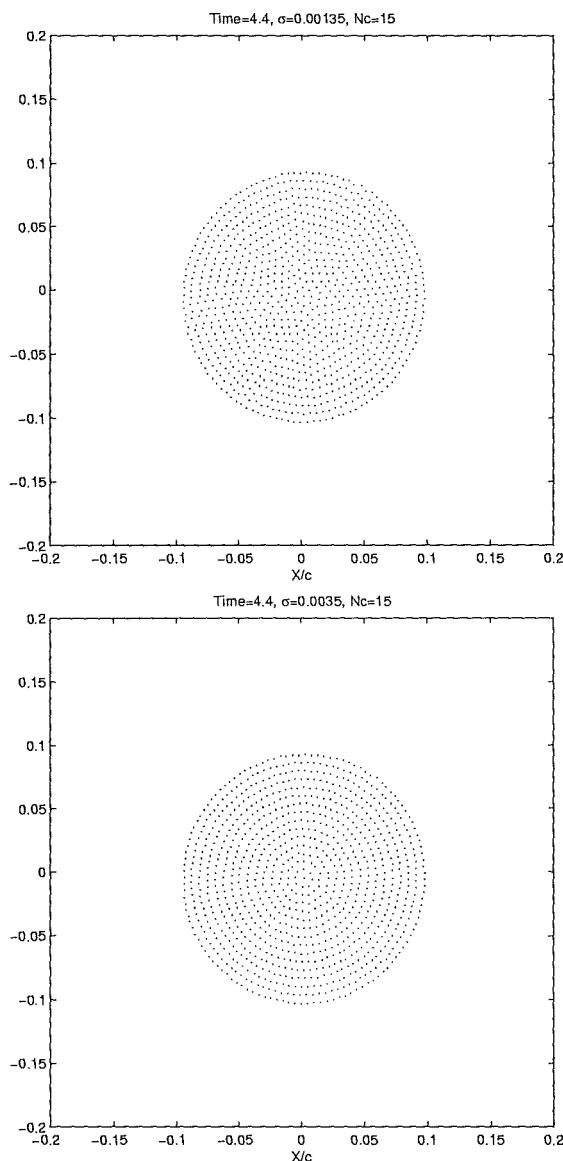


Figure 3.3: Core overlapping condition on accuracy of solution for a vortex with Rankine core

By using the above method to represent a circular vortex, a test calculation is carried out to examine the overlapping condition on the accuracy of the solution, in which time evolution of the vortex of radius $R_v = 0.1$ with a constant vorticity distribution within the core(Rankine core) is modelled . The time step used for the

calculation is 0.01 and 440 time steps have been advanced. The results at $t = 4.4$ are presented in figure 3.3 for two different core radii of vortex blobs respectively: one satisfies the overlapping condition ($\sigma/r_l = 1$) and the other does not ($\sigma/r_l = 0.42$). By comparing the two pictures, it is clearly shown that the overlapping condition is essential to maintain the smoothness of the vorticity field and the structure of the vortex.

3.1.2 Representation of body surface and implementation of boundary conditions

In the context of vorticity dynamics and discrete vortex methods, the surface of a body is one of the sources of vorticity generation and hence the vorticity or vortices in the flow field. The mechanisms for vorticity generation are very complex for a general fluid flow. However, for incompressible flow, which is the case in the present study, the vorticity generation at the body surface is due to the combined action of fluid viscosity and pressure gradient along the surface. Because the vorticity in the wake is a consequence of convection and diffusion of surface vorticity, it is crucial for the discrete vortex method to model the surface vorticity properly and accurately, which includes vorticity distribution along the surface and the vorticity generation rate at the surface.

As far as the surface vorticity is concerned, the contour of the aerofoil is divided into a number of panels - the polygonal representation of a closed curve and a thin strip near the body surface, which is also divided into the same number of trapezoids (control volume) as that of the panels, is set up to represent the vorticity near the surface as illustrated in figure 3.4. The density of the circulation $\gamma(s) = \int_0^\sigma \omega(s, n) dn$, which includes both the newly generated vorticity during the current time step and the residual vorticity from the previous timestep, is assumed to vary linearly along the surface coordinate s within each control volume. The vorticity

in each panel is also approximated by evenly positioned and overlapping vortex particles and the strength of each vortex particle is determined by the γ value at the node points (interfaces of the control zone). For example, if the vorticity in panel j is further broken down into N_s vortex particles, then the strength of the particle i , $i = 1, 2, \dots, N_s$, is

$$\Gamma_i = \frac{\Delta s}{N_s} \left\{ \gamma_{j-1} \left(N_s - i + \frac{1}{2} \right) + \gamma_j \left(i - \frac{1}{2} \right) \right\} \quad (3.13)$$

The γ values of the node points can be solved at each time step by satisfying the boundary conditions at the body surface. In the context of discrete vortex methods, it has been shown that the no-slip and no-penetration condition are equivalent, i.e. either condition is sufficient to determine the velocity field. Traditionally, one control point is chosen for each panel to implement either no-slip or no-penetration condition. The disadvantage of this approach is that, because the boundary condition is satisfied only at a limited number of points, there is a risk of having fluid “leak” through the boundary and hence violating the law of conservation of mass.

So, in the present study, the no-penetration condition is implemented in the zero mass flux form. For a stationary body, this scheme can be expressed as

$$\Delta\psi_j = \psi(\tilde{x}_{j+1}) - \psi(\tilde{x}_j) = 0 \quad (3.14)$$

for the panel with nodes \tilde{x}_{j+1} and \tilde{x}_j , where $\Delta\psi_j$ is a joint contribution from the free stream, the vortices from the control zone and in the wake. For example, the contribution from the free stream \mathbf{u}_∞ is

$$\Delta\psi_j = (\mathbf{u}_\infty \cdot \mathbf{n}_j) \Delta s_j \quad (3.15)$$

and the contribution from a vortex blob Γ_i located at \mathbf{x}_i is

$$\Delta\psi_j = \frac{\Gamma_i}{4\pi} \frac{|\mathbf{x}_j - \mathbf{x}_i|^2 + \sigma^2}{|\mathbf{x}_{j+1} - \mathbf{x}_i|^2 + \sigma^2} \quad (3.16)$$

By enforcing this equation for each panel, a linear algebraic system, which is to be solved at each time step, is set up with γ values at the node points as unknowns. However, for N panels, it is easy to check that if equation 3.14 is enforced in $N - 1$ panels, then this equation is also satisfied automatically in the remaining panel; in other words, only $N - 1$ equations are independent by implementing equation 3.14. A further equation is needed to make the solution unique. Fortunately, this can be achieved by using the vorticity conservation law. For the present method, we have

$$\sum_i (\Gamma_w)_i + \sum_k (\Gamma_n)_k = \Gamma_v \quad (3.17)$$

where Γ_w and Γ_n are the circulations of each vortex particle in the wake and within the control zone (nascent vortices) respectively, and Γ_v is the total vorticity of the initial interaction vortex.

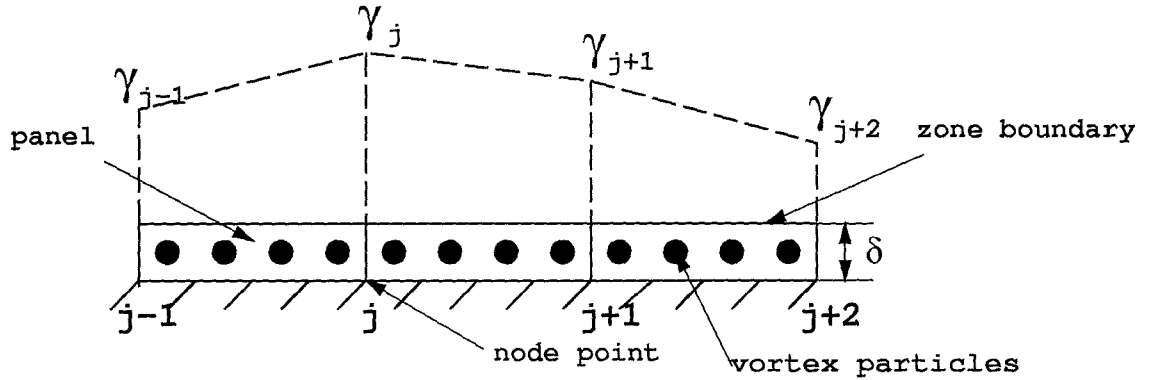


Figure 3.4: Illustration of surface panels and vortex particle generation using the linear distributed density of circulation in the control zone

Like the vortices in the wake, the vortices in the control zone are also convected and diffused at each time step. Depending on their new positions (in or out of the outer border of the control zone), they are released into the wake or absorbed as residual vorticity. Equally, if the center of a particle from the wake enters the control zone, it will be absorbed.

Although the velocity of the vortices in the control zone can also be calculated using equation 3.9, this approach leads to an oscillating velocity distribution due

to the fact that the boundary condition implemented cannot guarantee cancellation of the normal velocity at every point along the surface. The resulting transport of the vortex particles can lead to an unrealistic shedding of surface vorticity into the wake. Because the control zone is very thin, it is appropriate to assume the boundary-layer approximation there, namely $\omega = -\partial u/\partial n$, thus $\gamma(s) = -u(s)_{n=\sigma}$. Hence the vorticity weighted average velocity across the control zone, which is also used for the tangential velocity of the nascent vortices, is given by

$$u(s)_{av} = \frac{\int_0^\delta u\omega \, dn}{\int_0^\delta \omega \, dn} = \frac{u(s)_{n=\delta}}{2} = -\frac{\gamma(s)}{2} \quad (3.18)$$

which is independent of the specific profile of $\omega(y)$. For a stationary body, using the continuity equation in each control volume, the normal velocity of the nascent vortices located at $\delta/2$ above the panel with nodes j and $j+1$ is

$$(v_n)_j = \frac{(\gamma_j - \gamma_{j+1})\delta}{\Delta s} \frac{\delta}{4} \quad (3.19)$$

This is consistent with the γ distribution within the control zone and the exact boundary condition at the body surface, hence there is no oscillation within each panel.

3.1.3 Calculation of the surface pressure

Of particular interest in the study is an examination of the effect of the interaction vortex on the aerodynamic performance of the aerofoil, which requires the calculation of the surface pressure distribution. This, in turn, can be integrated into the aerodynamic coefficients such as C_n, C_t and $C_{m\frac{1}{4}}$.

For the body-oriented local orthogonal coordinate system (\mathbf{s}, \mathbf{n}) , the tangential momentum equation can be written at the surface of a stationary body:

$$\frac{1}{\rho} \frac{\partial p}{\partial s} = -\nu \mathbf{s} \cdot (\nabla \times \boldsymbol{\omega}) \quad (3.20)$$

which can be reduced to

$$\frac{1}{\rho} \frac{\partial p}{\partial s} = -\nu \frac{\partial \omega}{\partial n} \quad (3.21)$$

The term on the right-hand side of the equation represents the rate of vorticity creation per unit length at the body surface[108].

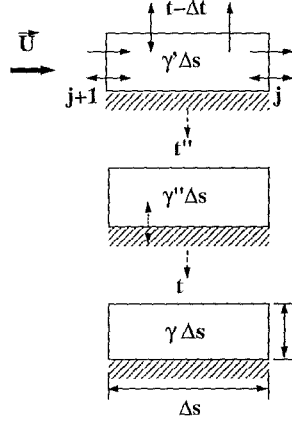


Figure 3.5: Calculation of newly created circulation from the body surface for each surface control volume

Considering a control volume with node points j and $j + 1$ shown in figure 3.5, the circulation at time $t - \Delta t$ is assumed to be $\gamma' \Delta s_j$. After convection and diffusion through the interfaces (not including the new vorticity generated at the body surface) during a time interval Δt , which is represented by the symbols \longrightarrow and \longleftarrow respectively, the residual circulation will be $\gamma'' \Delta s_j$. If the circulation of nascent vortices in the control volume at time t is calculated as $\gamma \Delta s_j$, then the newly created circulation from the body surface during the time interval Δt should be $\gamma \Delta s_j - \gamma'' \Delta s_j$. Thus for this panel we have

$$\frac{p_j - p_{j+1}}{\Delta s_j} = \frac{\gamma - \gamma''}{\Delta t} \quad (3.22)$$

Once the pressure value at a reference point is known, the entire pressure distribution along the body surface can be easily calculated by integrating equation 3.22

The aerodynamic force exerted on the aerofoil due to the surface pressure distribution is a summation of the forces exerted on each panel. By assuming a linear

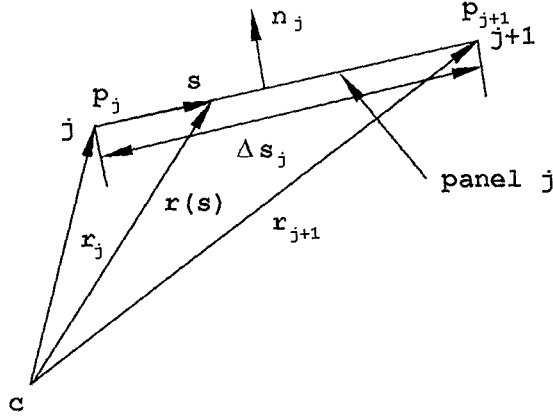


Figure 3.6: Calculation of the contribution to the aerodynamic force and moment from each panel

distribution of the surface pressure between nodes j and $j + 1$ of panel j , see figure 3.6, the force acting on this panel is

$$\mathbf{F}_j = -\frac{(p_j + p_{j+1})}{2} \Delta s_j \mathbf{n}_j \quad (3.23)$$

and the moment about a reference point, say the quarter-chord point $c_{\frac{1}{4}}$ of an aerofoil, can be calculated as

$$\mathbf{m}_j = \int_0^{\Delta s_j} \left[p_j \frac{\Delta s_j - s}{\Delta s_j} + p_{j+1} \frac{s}{\Delta s_j} \right] \mathbf{n}_j \times \left(\mathbf{r}_j \frac{\Delta s_j - s}{\Delta s_j} + \mathbf{r}_{j+1} \frac{s}{\Delta s_j} \right) ds \quad (3.24)$$

$$= \frac{\Delta s_j}{3} [(p_j + 0.5p_{j+1}) \mathbf{n}_j \times \mathbf{r}_j + (0.5p_j + p_{j+1}) \mathbf{n}_j \times \mathbf{r}_{j+1}] \quad (3.25)$$

Thus, the force acting on the aerofoil is

$$\mathbf{F}_b = (F_b)_x \mathbf{i} + (F_b)_y \mathbf{j} = \sum_{j=1}^{N_p} \mathbf{F}_j \quad (3.26)$$

and the moment about the reference point $c_{\frac{1}{4}}$ is

$$\mathbf{m}_{c_{\frac{1}{4}}} = m_{c_{\frac{1}{4}}} \mathbf{k} = \sum_{j=1}^{N_p} \mathbf{m}_j \quad (3.27)$$

The aerodynamic coefficients C_n , C_t and $C_{m_{\frac{1}{4}}}$ can now be defined as

$$C_n = \frac{(F_b)_y}{1/2 \rho U_{\infty}^2 c} \quad (3.28)$$

$$C_t = \frac{(F_b)_x}{1/2\rho U_\infty^2 c} \quad (3.29)$$

$$C_{m^{1/4}} = \frac{m_{c^{1/4}}}{1/2\rho U_\infty^2 c^2} \quad (3.30)$$

3.1.4 Controlling the total number of particles

The computational cost of evaluating the velocity of the system of vortices using the Biot-Savart Law is proportional to the square of the number of vortices ($O(N_v^2)$). Therefore when the total number of vortices in the flow becomes very large, the CPU time needed to carry out the computation will be prohibitive. Two measures are adopted in this study to limit the number of vortices in the wake.

Firstly, a different, usually larger, core radius is used when discretising the interaction vortex than that employed for the vortices shed from the aerofoil surface. To simulate high Reynolds number flow around the aerofoil, the control zone should be very thin, of order $O(\frac{1}{\sqrt{Re}})$ for a laminar flow, to reflect the boundary layer near the body surface. Hence the core radius for the nascent vortices should also be of the order of the control zone height. If this core radius was to be used to discretise the interaction vortex with relatively large radius, then the number of the vortices would be excessively large.

Secondly, an amalgamation scheme is used for vortices in the wake which are far from the surface. By using complex notation, the velocity at point Z induced by a vortex blob with circulation Γ_p and located at point Z_p can be calculated by a point vortex approximation, provided $\frac{|Z_p - Z|}{\sigma_p} \gg 1$.

$$V^*(Z) = \frac{i\Gamma_p}{2\pi} \frac{1}{Z - Z_p} \quad (3.31)$$

where Z is the complex position $x + iy$ and V^* the complex conjugate velocity of $V = u + iv$. Suppose two vortices with locations Z_j, Z_k and strengths Γ_j, Γ_k are merged into a new vortex with strength Γ' and location Z' , the difference between

the velocities at point Z induced by the new vortex and original two vortices is

$$\Delta V = \frac{\Gamma'}{Z - Z'} - \frac{\Gamma_j}{Z - Z_j} - \frac{\Gamma_k}{Z - Z_k} \quad (3.32)$$

in which some constant factors have been omitted.

If we assume Z is far from both points Z_j and Z_k , and another point Z_n is closer to Z_j, Z_k and Z' than Z , then equation 3.32 can be written as

$$\begin{aligned} \Delta V &= \frac{\Gamma'}{(Z - Z_n)(1 - \frac{Z' - Z_n}{Z - Z_n})} - \frac{\Gamma_j}{(Z - Z_n)(1 - \frac{Z_j - Z_n}{Z - Z_n})} - \frac{\Gamma_k}{(Z - Z_n)(1 - \frac{Z_k - Z_n}{Z - Z_n})} \\ &= \frac{1}{\tilde{Z}} \left[\frac{\Gamma'}{1 - \frac{\tilde{Z}'}{\tilde{Z}}} - \frac{\Gamma_j}{1 - \frac{\tilde{Z}_j}{\tilde{Z}}} - \frac{\Gamma_k}{1 - \frac{\tilde{Z}_k}{\tilde{Z}}} \right] \end{aligned}$$

Under the assumptions given above, we have $|\tilde{Z}'/\tilde{Z}| < 1$, $|\tilde{Z}_j/\tilde{Z}| < 1$ and $|\tilde{Z}_k/\tilde{Z}| < 1$, so we can perform the Laurent expansions for $\frac{1}{1 - \tilde{Z}'/\tilde{Z}}$, $\frac{1}{1 - \tilde{Z}_j/\tilde{Z}}$ and $\frac{1}{1 - \tilde{Z}_k/\tilde{Z}}$ respectively.

By keeping the first three terms of the series, ΔV can be approximated by

$$\Delta V = \frac{\Gamma' - \Gamma_j - \Gamma_k}{\tilde{Z}} - \frac{\Gamma' \tilde{Z}' - \Gamma_j \tilde{Z}_j - \Gamma_k \tilde{Z}_k}{\tilde{Z}^2} - \frac{\Gamma' \tilde{Z}'^2 - \Gamma_j \tilde{Z}_j^2 - \Gamma_k \tilde{Z}_k^2}{\tilde{Z}^3} + O(|\tilde{Z}|^3) \quad (3.33)$$

where $|\tilde{Z}| = \max\{|\frac{\tilde{Z}'}{\tilde{Z}}|, |\frac{\tilde{Z}_j}{\tilde{Z}}|, |\frac{\tilde{Z}_k}{\tilde{Z}}|\}$.

From the above equation, an obvious choice to remove the first two terms is to take

$$\Gamma' = \Gamma_j + \Gamma_k \quad (3.34)$$

and

$$Z' = (\Gamma_j Z_j + \Gamma_k Z_k) / \Gamma' \quad (3.35)$$

Thus, both the total vorticity and linear moment of vorticity are conserved. The last term in equation 3.33, however, cannot be removed which will be used as the merging criterion to ensure ΔV is below some tolerance. By inserting equations 3.34 and 3.35 into 3.33 and taking the modulus, this term can be written as

$$\frac{|\Gamma_j \Gamma_k| |Z_j - Z_k|^2}{|\Gamma_j + \Gamma_k| |\tilde{Z}|^3} \quad (3.36)$$

To ensure that the effect of merging on the induced velocity at the body surface is small, i.e. assuming that point Z is at the surface of the body, the following criterion is finally adopted:

$$\frac{|\Gamma_j \Gamma_k|}{|\Gamma_j + \Gamma_k|} \frac{|Z_j - Z_k|^2}{(D_0 + d_1)^{1.5} (D_0 + d_2)^{1.5}} \leq \epsilon \quad (3.37)$$

where d_1 and d_2 are distances from the two vortices to the closest wall respectively and D_0 is a safety factor. From this criterion for merging vortices, several points can be made. Firstly, it encourages merging of weak vortices with the same sign and discourages merging of vortices with nearly opposite circulations. Secondly, the vortices which are close to each other and far from the surface of the body are more likely to merge. However, because the merging process changes the local vorticity distribution, for instance the overlapping condition of the vortices is usually destroyed unless a bigger core radius is used after merging, it is not appropriate for applications where the local vorticity value is important.

Another possible method to reduce the computational cost of the vortex method without changing the local vorticity field is to employ a fast summation algorithm, which has operational count $O(N_v)$ or $O(N_v \log N_v)$ rather than $O(N_v^2)$ [38]. A fast algorithm based on the the domain decomposition and Laurent series has been incorporated into the code[113] and the detail of the method is given in Chapter 7.

3.2 Three dimensional case

3.2.1 Discretization and evolution of vorticity field

In 3-D, there are two main approaches by which the continuous vorticity field can be discretized into a finite number of smaller vortex elements. One is the so-called filament method(Leonard, 1985) in which the non-zero vorticity region is replaced by vortex lines(tubes) and these lines are treated as entities, i.e. they move as material volumes. The basis of this approach is the Helmholtz and Kelvin theory

which states that for inviscid flows, vortex lines move as material lines and the circulation of each vortex line(tube) is conserved. This method has been widely used in modelling potential steady and unsteady aerodynamic flow problems, as well as the unbounded vortex system such as vortex ring(s)(Leonard, 1985). The other is the vortex particle method which is the extended form of the 2-D singular or smoothed vortex point(blobs) method. As in the 2-D discrete vortex method, the entire vorticity field is represented by a large number of vortex particles with or without finite cores. The advantage of this approach lies in its flexibility and versatility in terms of simulating more general flow problems and inclusion of viscous effects. So this method has been adopted in the present study.

Corresponding to the 2-D point-vortex model, in 3-D, the vorticity field can be represented by singular vortex particles as

$$\bar{\omega}(\mathbf{x}, t) = \sum_{p=1}^{N_v} \omega_p(t) vol_p \delta(\mathbf{x} - \mathbf{x}_p(t)) \quad (3.38)$$

$$= \sum_{p=1}^{N_v} \alpha_p(t) \delta(\mathbf{x} - \mathbf{x}_p(t)) \quad (3.39)$$

where $\delta(x)$ is the 3-D Dirac function and $\alpha_p(t) = \omega_p(t) vol_p$ is the strength of the particle p which is associated with the vorticity $\omega_p(t)$ and volume vol_p . Inserting this equation into the Biot-Savart formula and by neglecting the contributions from the free stream and the boundary condition for the time being, one can obtain

$$\mathbf{u}(\mathbf{x}, t) = \sum_{p=1}^{N_v} K(\mathbf{x} - \mathbf{x}_p(t)) \times \alpha_p(t) \quad (3.40)$$

where $K(\mathbf{x}) = -\frac{\mathbf{x}}{4\pi|\mathbf{x}|^3}$ is the Biot-Savart kernel or singular kernel and the velocity at the position of particle q is calculated by

$$\mathbf{u}(\mathbf{x}_q, t) = \sum_{p=1, p \neq q}^{N_v} K(\mathbf{x} - \mathbf{x}_p(t)) \times \alpha_p(t) \quad (3.41)$$

As in the 2-D case, the singularity of the point vortex model can be removed by

using smoothed or regularized vortex particles:

$$\bar{\omega}_\sigma(\mathbf{x}, t) = \sum_{p=1}^{N_v} \alpha_p(t) \xi_\sigma(\mathbf{x} - \mathbf{x}_p(t)) \quad (3.42)$$

where the regularisation function ξ_σ is radially symmetric with a core radius σ , i.e. $\xi_\sigma(\mathbf{x}) = \frac{1}{\sigma^3} \zeta(\frac{|\mathbf{x}|}{\sigma})$ with $4\pi \int_0^\infty \zeta(\rho) \rho^2 d\rho = 1$. Accordingly, the velocity at any point \mathbf{x} in the flow field is:

$$\mathbf{u}(\mathbf{x}, t) = \sum_{p=1}^{N_v} K_\sigma(\mathbf{x} - \mathbf{x}_p(t)) \times \alpha_p(t) \quad (3.43)$$

and the kernel now has the form: $K_\sigma(\mathbf{x}) = q(|\mathbf{x}|/\sigma) K(\mathbf{x})$ and $q(|\mathbf{x}|/\sigma) = \int_0^\rho \zeta(t) t^2 dt$.

A number of choices are available, for example the 3-D Gaussian distribution, in selecting the regularization functions. In the present study, the so-called high order algebraic smoothing function which was put forward by Winkelmans and Leonard [120] has been adopted:

$$\zeta(\rho) = \frac{15}{8\pi} \frac{1}{(\rho^2 + 1)^{7/2}} \quad (3.44)$$

The stretching term, which is introduced by the gradient of the velocity field and is unique for 3-D flow problems can be calculated explicitly from the derivatives of the velocity given in equation 3.43. Thus, for inviscid flows, the evolution equations for the system of vortex particles can be described by the following ODEs:

$$\frac{d\mathbf{x}_p(t)}{dt} = \mathbf{u}_\sigma(\mathbf{x}_p(t), t) \quad (3.45)$$

$$\frac{d\alpha_p(t)}{dt} = [\alpha_p(t) \cdot \nabla] \mathbf{u}_\sigma(\mathbf{x}_p(t), t) \quad (3.46)$$

According to the analysis in Chapter 2, the equation 3.46, which is referred to as the classical scheme, can also be written in the following forms:

$$\frac{d\alpha_p(t)}{dt} = [\alpha_p(t) \cdot \nabla^T] \mathbf{u}_\sigma(\mathbf{x}_p(t), t) \quad (3.47)$$

$$\frac{d\alpha_p(t)}{dt} = (\alpha_p(t) \cdot \left(\frac{\nabla + \nabla^T}{2}\right) \mathbf{u}_\sigma(\mathbf{x}_p(t), t)) \quad (3.48)$$

which are called the transpose scheme and the mixed scheme respectively.

The three equations given above for calculating the stretching term are equivalent provided the vorticity field is divergence-free. However, as shown in [120], the vorticity field represented by equation 3.39 or 3.42 is not divergence-free, i.e. $\nabla \cdot \bar{\omega}(\mathbf{x}, t) \neq 0$. The effect of this unphysical representation of the vorticity field on its subsequent development and hence the solution of entire flow problem is no doubt a drawback of the 3-D vortex particle method and some methods have been proposed to maintain the divergence-free condition of the vorticity field. For example, by considering the curl of the velocity field represented by equation 3.43, a procedure can be implemented as follows: if and when $\bar{\omega}(\mathbf{x}, t)$ becomes a poor representation of the divergence-free field $\omega(\mathbf{x}, t)$, assign new particle strength $\alpha_p^{new}(t)$ by imposing that $\bar{\omega}(\mathbf{x}(t), t) = \omega(\mathbf{x}(t), t)$, which leads to a solution of the system of linear equations for $\alpha_p^{new}(t)$ for all particles p :

$$\sum_{q=1}^{N_v} \alpha_p^{new}(t) \zeta(\mathbf{x}_p(t) - \mathbf{x}_q(t)) = \nabla \times \mathbf{u}_\sigma(\mathbf{x}_p(t), t) \quad (3.49)$$

If the divergence-free condition of the vorticity field cannot be guaranteed, however, according to the analysis by Winkelmann et al [120], only the transpose scheme leads to the exact conservation of the total vorticity and a weak solution of equation 3.47, which is, therefore, used exclusively for the present computation.

The effects of viscous diffusion can be considered by the use of an integral representation for the Laplacian operator $\nabla^2 \omega$. A detailed discussion on the method was given in [120] and essentially, the viscous diffusion is modelled by exchanging vorticity between vortex particles, which gives

$$\nabla^2 \omega \approx \frac{2\nu}{\sigma^2} \sum_{q=1}^{N_v} (vol_p \alpha_q(t) - vol_q \alpha_p(t)) \eta_\sigma(\mathbf{x}_p(t) - \mathbf{x}_q(t)) \quad (3.50)$$

where $\eta_\sigma(\mathbf{x}) = \eta(|\mathbf{x}|/\sigma)/\sigma^3$ and $\eta(\rho) = -\frac{1}{\rho} \frac{d}{d\rho} \zeta(\rho)$.

By using the high order algebraic smoothing function (equation 3.44) and including the viscous diffusion term, the final expressions for the evolution of a set of vortex particles $p = 1, 2, \dots, N_v$ are

$$\begin{aligned} \frac{d}{dt} \mathbf{x}_p &= -\frac{1}{4\pi} \sum_{q=1}^{N_v} \frac{(|\mathbf{x}_p - \mathbf{x}_q|^2 + 2.5\sigma^2)}{(|\mathbf{x}_p - \mathbf{x}_q|^2 + \sigma^2)^{5/2}} (\mathbf{x}_p - \mathbf{x}_q) \times \alpha_q \quad (3.51) \\ \frac{d}{dt} \alpha_p &= \frac{1}{4\pi} \sum_{q=1}^{N_v} \left[\frac{(|\mathbf{x}_p - \mathbf{x}_q|^2 + 2.5\sigma^2)}{(|\mathbf{x}_p - \mathbf{x}_q|^2 + \sigma^2)^{5/2}} \alpha_p \times \alpha_q \right. \\ &\quad + 3 \frac{(|\mathbf{x}_p - \mathbf{x}_q|^2 + 3.5\sigma^2)}{(|\mathbf{x}_p - \mathbf{x}_q|^2 + \sigma^2)^{7/2}} (\alpha_p \cdot ((\mathbf{x}_p - \mathbf{x}_q) \times \alpha_p)) (\mathbf{x}_p - \mathbf{x}_q) \\ &\quad \left. + 105\nu \frac{\sigma^4}{(|\mathbf{x}_p - \mathbf{x}_q|^2 + \sigma^2)^{9/2}} (vol_p \alpha_q - vol_q \alpha_p) \right] \end{aligned}$$

From the viewpoint of physics, viscous diffusion in a fluid results from the random interaction of molecules and the non-uniformity of the fluid motion. The molecular interactions extend a small distance depending on the Reynolds number of the flow, so the amount of viscous diffusion at a point is determined only by the fluid in the neighbourhood of that point. In the present vortex particle method, it can be shown from equation 3.52 that for any point \mathbf{x}^p , only the nearby particles make significant contributions to its viscous term because the function $\sigma^4/(|\mathbf{x}_p - \mathbf{x}_q|^2 + \sigma^2)^{9/2}$ decays very fast (by the order of $1/|\mathbf{x}|^9$) as the distance $|\mathbf{x}_p - \mathbf{x}_q|$ increases. So when the viscous term at a point \mathbf{x}^p is calculated the summation is only applied to those particles q which satisfy $|\mathbf{x}_p - \mathbf{x}_q| \leq 5\sigma$. Thus, some reductions in the computational cost can be achieved.

As in the 2-D case, the equations 3.51 and 3.52 for moving the vortex particles and updating the vorticity field respectively, can be advanced in time by the first order Euler or the second order Adams-Bashforth scheme.

In figure 3.7, an example is given in using the vortex particle method to calculate the interaction and fusion of two vortex rings. Each vortex ring of Gaussian cross

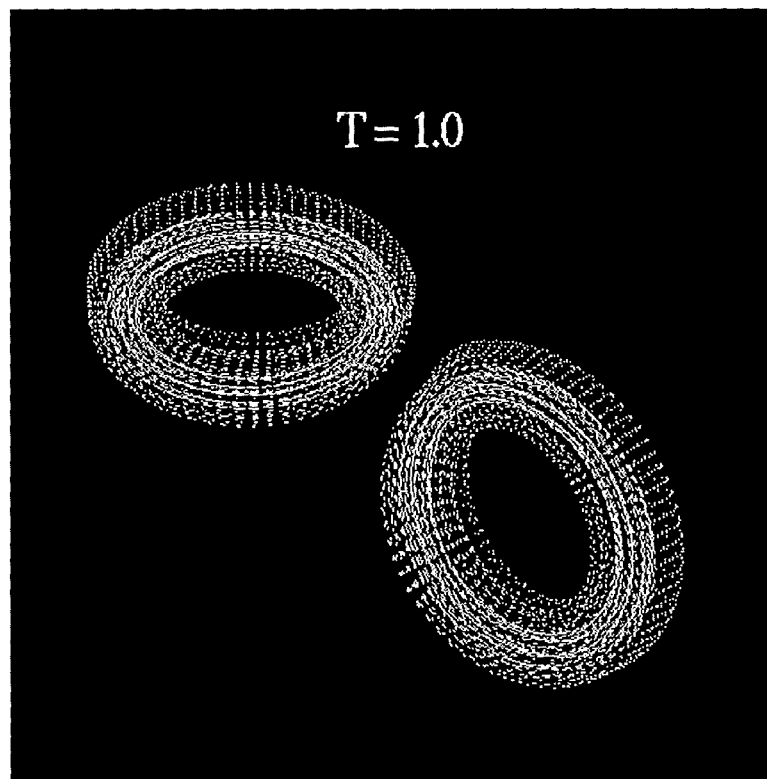
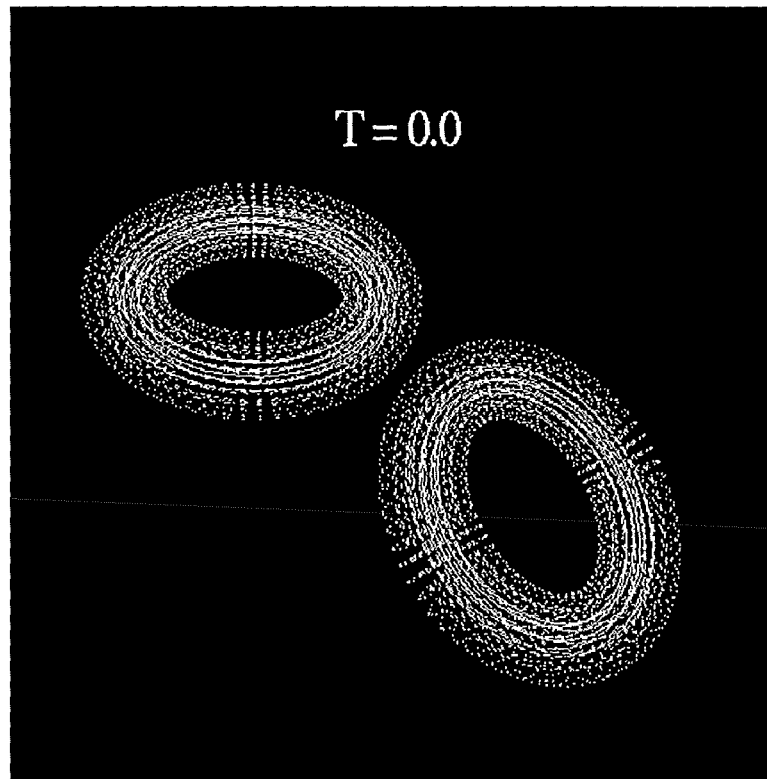


Figure 3.7: Results for the interaction and fusion of two vortex rings using the 3-D vortex particle method

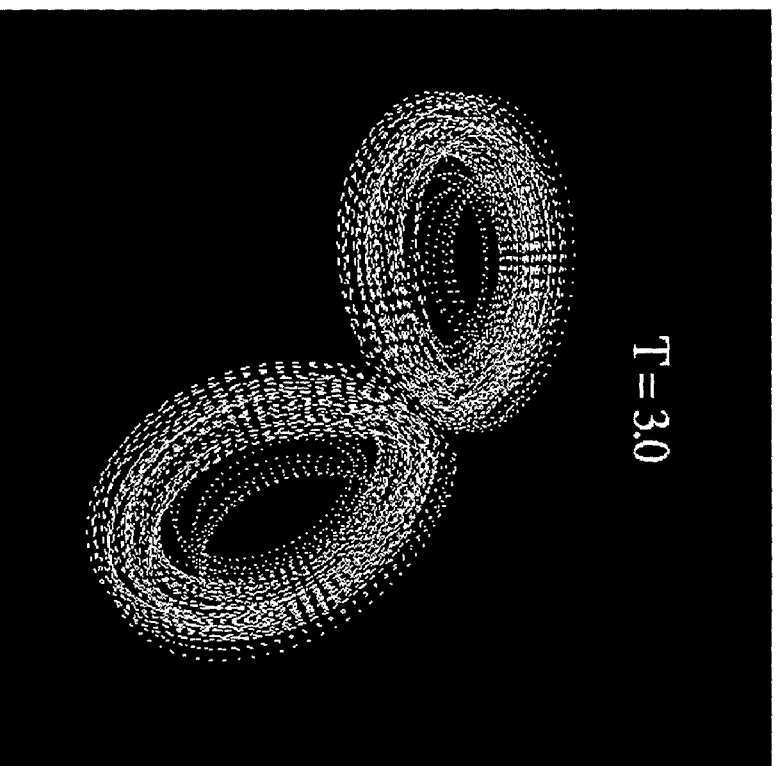
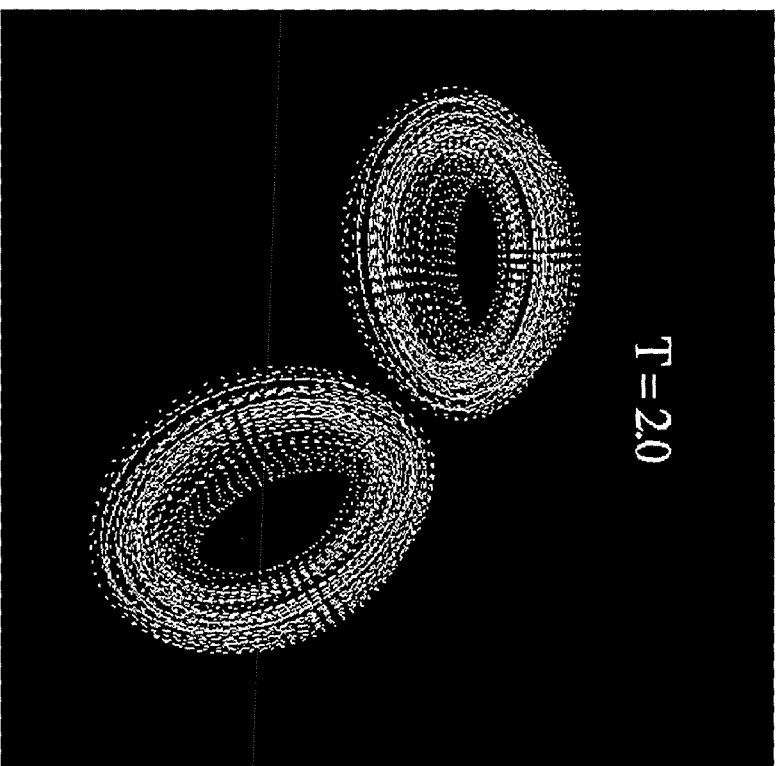


Figure 3.7: Continued

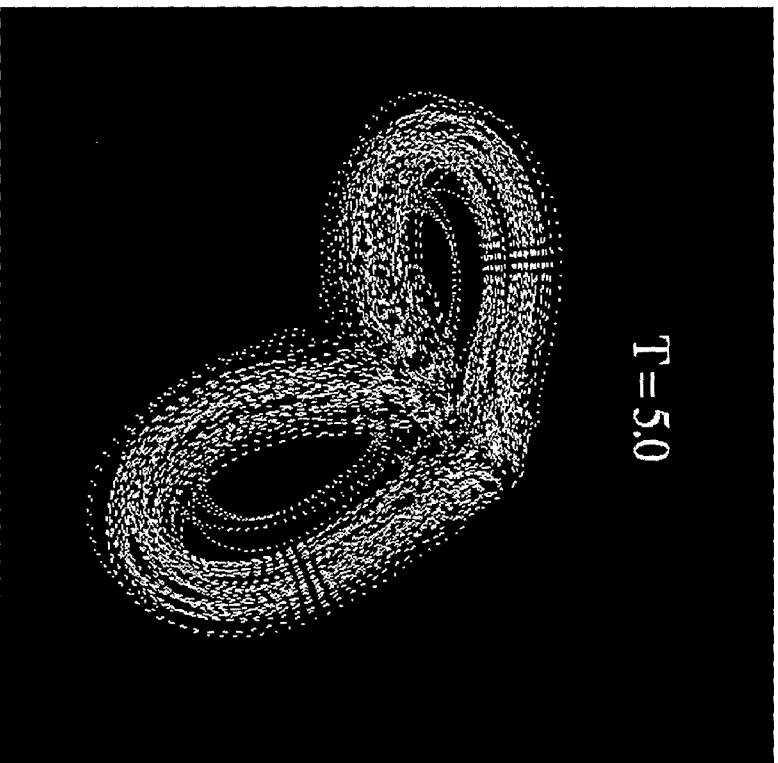
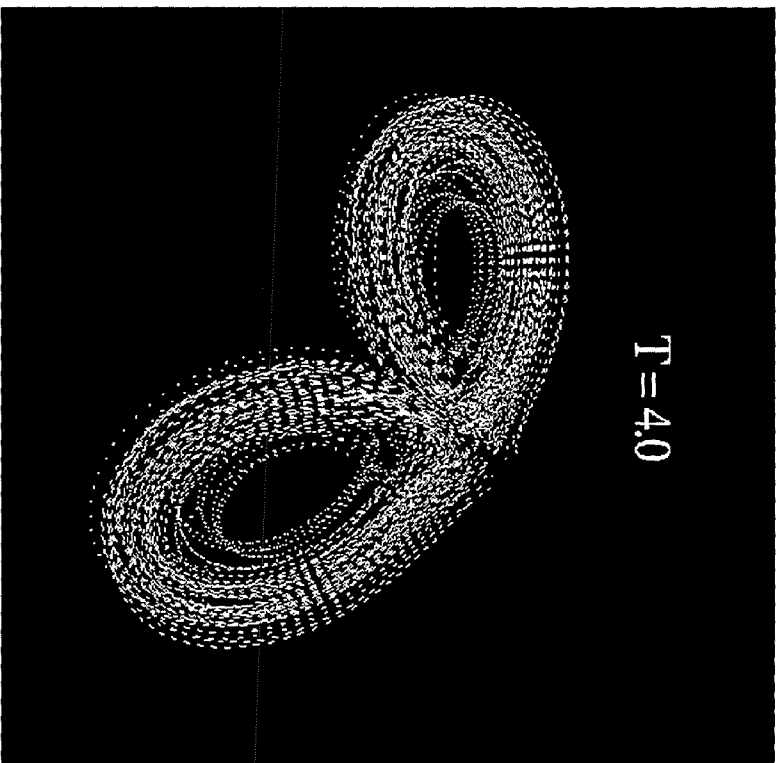


Figure 3.7: Continued

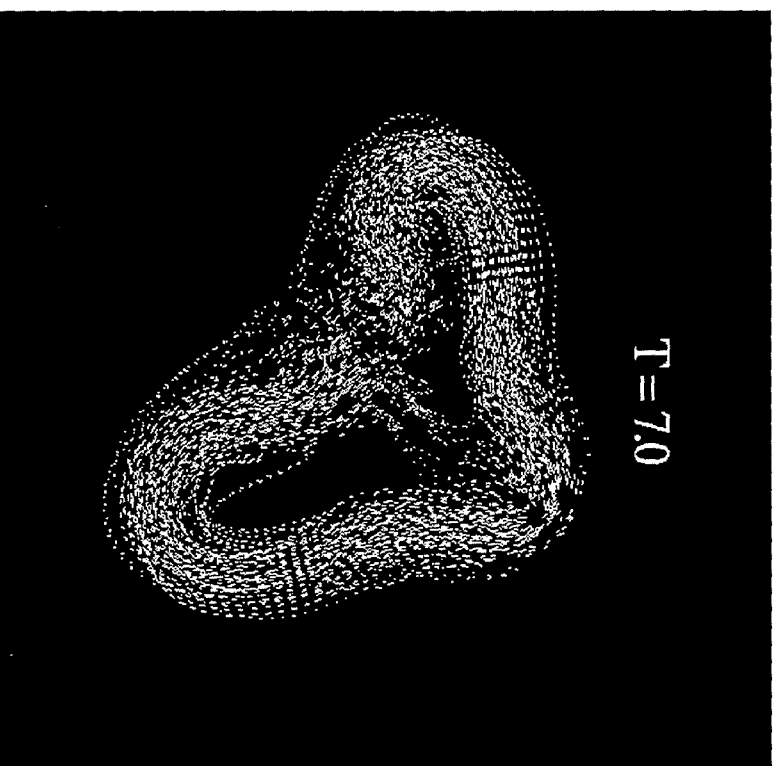
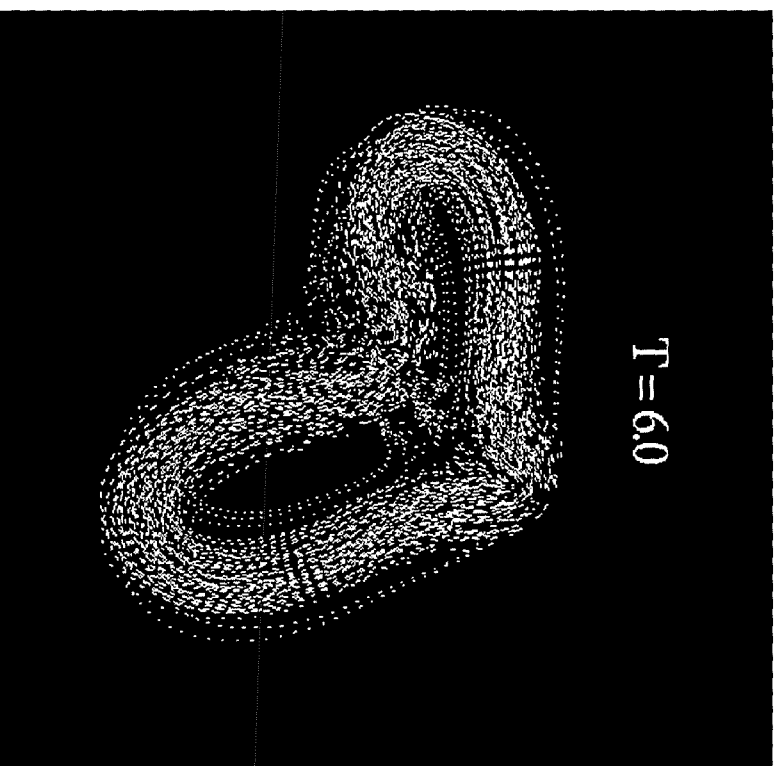


Figure 3.7: Continued

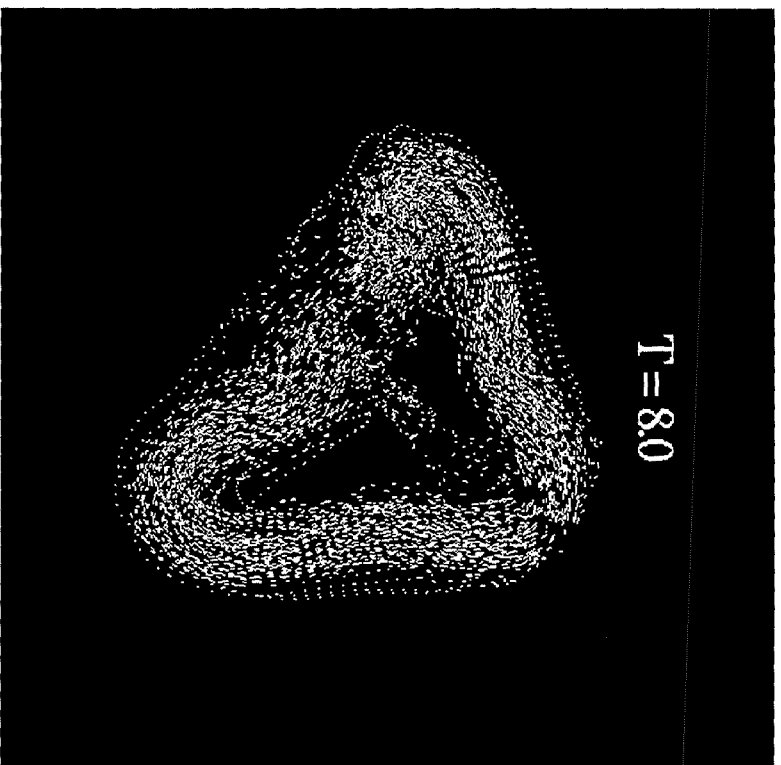


Figure 3.7: Continued

section is represented by a number of vortex particles. To discretise the core of the vortex ring, a mesh system is constructed using N_ϕ cross sections of a torus separated by an angle $\Delta\phi = 2\pi/N_\phi$ and N_s cells within each cross section, see figure 3.2. The elements within each cross section of the ring are arranged on n_c radial locations and each cell has an equal area πr_l^2 . The center of each vortex element is located at its centroid x_i and the initial strength vector of the vortex element is set equal to $\omega(x_i, 0)dv_i$, where dv_i is the volume of each vortex element. Nine snapshots have been given which show that at first the two vortex rings approach each other and then fuse into another bigger ring with an irregular shape.

3.2.2 Discretization of 3-D body surface - source panel method

The source panel method has been used to represent the body(wing) surface and to implement relevant boundary conditions. The entire surface of the body is divided into a number of quadrilateral panels as shown in figure 3.8. For the sake of simplicity, planar panels were used in most applications. In this case, the features of each panel, such as the normal unit vector, geometrical centre and the area etc. can be determined by the coordinates of its four node points $\mathbf{x}_1, \mathbf{x}_2, \mathbf{x}_3, \mathbf{x}_4$. For example, the unit normal vector \mathbf{n} of the panel is

$$\mathbf{n} = \frac{(\mathbf{x}_4 - \mathbf{x}_2) \times (\mathbf{x}_3 - \mathbf{x}_1)}{|(\mathbf{x}_4 - \mathbf{x}_2) \times (\mathbf{x}_3 - \mathbf{x}_1)|} \quad (3.52)$$

and the geometrical center \mathbf{x}_c of the panel is

$$\mathbf{x}_c = \frac{\mathbf{x}_1 + \mathbf{x}_2 + \mathbf{x}_3 + \mathbf{x}_4}{4} \quad (3.53)$$

The velocity at point p induced by a point source of strength σ located at point q is

$$\mathbf{u}_s(\mathbf{x}_p) = \frac{\sigma}{4\pi} \frac{\mathbf{x}_p - \mathbf{x}_q}{|\mathbf{x}_p - \mathbf{x}_q|^3} \quad (3.54)$$

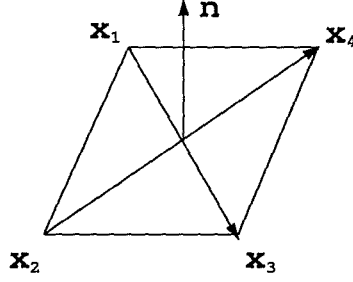


Figure 3.8: Illustration of a planar surface panel for 3-D calculation

For cases in which the source is distributed on a given surface S' such as a surface panel, the induced velocity can be integrated as

$$\mathbf{u}_s(\mathbf{x}_p) = \frac{1}{4\pi} \int_{\mathbf{x}_q \in S'} \frac{\sigma(\mathbf{x}_q)(\mathbf{x}_p - \mathbf{x}_q)}{|\mathbf{x}_p - \mathbf{x}_q|^3} ds \quad (3.55)$$

provided that \mathbf{x}_p is not on the surface S' . When point \mathbf{x}_p is located on the surface S' , the above integral is not defined. Fortunately, this problem can be solved by evaluating a singular Fredholm equation of the second kind, which gives[42]:

$$\mathbf{u}_s(\mathbf{x}_p) = \mathbf{n}(\mathbf{x}_p) \frac{\sigma(\mathbf{x}_p)}{2} + \lim_{\epsilon \rightarrow 0} \frac{1}{4\pi} \int_{\mathbf{x}_q \in S', \mathbf{x}_q \notin B_\epsilon} \frac{\sigma(\mathbf{x}_q)(\mathbf{x}_p - \mathbf{x}_q)}{|\mathbf{x}_p - \mathbf{x}_q|^3} ds \quad (3.56)$$

where B_ϵ is a small area surrounding the point p with radius ϵ and $\mathbf{n}(\mathbf{x}_p)$ is the outward normal vector of the surface at \mathbf{x}_p .

For panel methods, by using equations 3.55 and 3.56, the induced velocity by all the panels can be calculated as

$$\mathbf{u}_s(\mathbf{x}_p) = \frac{1}{4\pi} \sum_{i=1}^{N_p} \int_{S_i} \frac{\sigma(\mathbf{x}_q)(\mathbf{x}_p - \mathbf{x}_q)}{|\mathbf{x}_p - \mathbf{x}_q|^3} ds \quad (3.57)$$

for point \mathbf{x}_p which is not on the surface of the panels, and

$$\mathbf{u}_s(\mathbf{x}_p) = \frac{1}{2} \sigma(\mathbf{x}_p) \mathbf{n}_j + \frac{1}{4\pi} \sum_{i=1, i \neq j}^{N_p} \int_{S_i} \frac{\sigma(\mathbf{x}_q)(\mathbf{x}_p - \mathbf{x}_q)}{|\mathbf{x}_p - \mathbf{x}_q|^3} ds \quad (3.58)$$

for point \mathbf{x}_p which is on the surface of the j th panel, where \mathbf{n}_j denotes the outward normal vector on the j th panel and N_p is the total number of panels. If we assume

that the strength of the source distribution within each panel is constant, then the integral in equations 3.57 and 3.58 can be evaluated analytically for a planar panel. However, in the present study, to better represent the surface of a finite body, particularly in the region with rapid change of configuration such as the leading edge area of a finite wing, each panel is further divided into multiple subpanels with local curvatures instead of the planar panels. The contribution of the source distribution within a panel is then obtained from its subpanels which are considered point sources. Furthermore, a panel is also considered a point source when calculating the velocity at a point which is far from the center of the panel.

When a non-zero vorticity region exists in the flow field, which is the case for the present study, the contribution of the surface source distribution to the vorticity stretching term is

$$(\boldsymbol{\omega}(\mathbf{x}_p) \cdot \nabla_p) \mathbf{u}_s(\mathbf{x}_p) = \frac{1}{4\pi} \sum_{i=1}^{N_p} \int_{S_i} \left[\frac{\boldsymbol{\omega}(\mathbf{x}_p)}{|\mathbf{x}_p - \mathbf{x}_q|^3} - \frac{3(\mathbf{x}_p - \mathbf{x}_q)[(\mathbf{x}_p - \mathbf{x}_q) \cdot \boldsymbol{\omega}(\mathbf{x}_p)]}{|\mathbf{x}_p - \mathbf{x}_q|^5} \right] \sigma(\mathbf{x}_q) ds \quad (3.59)$$

For unsteady flows, at each time-step, the source strength of each panel can be calculated by ensuring the normal velocity at a control point of the panel to be zero, which results in linear algebraic equations with σ_i as unknowns:

$$\sum_{i=1}^{N_p} A_{ki} \sigma_i + \mathbf{u} \cdot \mathbf{n}_k + \left[\sum_{j=1}^{N_v} B_{kj} \cdot \boldsymbol{\alpha}_j \right] \cdot \mathbf{n}_k = 0 \quad (3.60)$$

where $k = 1 \rightarrow N_p$ and the coefficients A_{ki} represent the contribution of the i_{th} panel to the normal velocity at the control point of the k_{th} panel and the second and third terms on the left-hand side are the contributions from the free-stream and the vorticity field outside the body surface respectively.

The matrix of the influence coefficients reflects the interaction between panels, therefore it is not time-dependent for solid bodies as long as there are no relative motions among them. So the matrix only needs to be inverted once during the calculation. The Gauss elimination method is used for this purpose, which is efficient

and accurate for a number of unknowns less than 2000. The time dependent part of the problem, namely the evolution of the vorticity field, should be modified at each time-step.

Due to the difficulties in the 3-D vortex particle method in terms of modelling the vorticity shedding from the body surface, in the present study, no vortices are allowed to shed from the surface. Furthermore, because of the configuration of both vortex ring and body, the flow is symmetric about the central plane of the body, so no vorticity will shed from the trailing edge either. Otherwise a proper form of Kutta condition should be applied to determine the shedding rate of vorticity at the trailing edge.

3.2.3 Calculation of aerodynamic forces

As to the calculation of the unsteady forces exerted on a body, generally, two methods can be used. In the first method, the forces are integrated from the calculated surface pressure distribution as discussed for the 2-D vortex method. A 3-D version of this method was given in reference[72], which is rather complicated due to the fact that if the flow is no longer irrotational, then the unsteady Bernoulli equation will not be a viable choice. The second method, referred to here as the global method, is based on Newton's second law and the vorticity distribution in the wake. Consider a body moving with speed $U_b(t)$ in an otherwise stationary fluid, the net force exerted on the body from surrounding fluid(of unit density) may be expressed as

$$\mathbf{F}_b = -\frac{d}{dt} \int_{fluid} \mathbf{u} dx = -\frac{d}{dt} \mathbf{I} \quad (3.61)$$

where the integral \mathbf{I} is the total momentum of the fluid, which can be calculated from the vorticity distribution in the flow[121]. For two-dimensional problems,

$$\mathbf{I} = \int_{fluid} \mathbf{x} \times \omega ds = \alpha \quad (3.62)$$

and for three-dimensional problem,

$$\mathbf{I} = \frac{1}{2} \int_{fluid} \mathbf{x} \times \omega ds = \frac{\alpha}{2} \quad (3.63)$$

where α is defined as the linear moment of vorticity. So, we have

$$\mathbf{F}_b = -\frac{d\alpha}{dt} \quad (3.64)$$

for two dimensional flows and

$$\mathbf{F}_b = -\frac{1}{2} d\alpha/dt \quad (3.65)$$

for three dimensional flows.

In the context of the discrete vortex particle method, it is convenient to evaluate α at each time step by the following equation, which approximates the integral in equation 3.63, using quadrature methods:

$$\alpha = \sum_{i=1}^{N_v} \mathbf{x}_i \times \alpha_i \quad (3.66)$$

where \mathbf{x}_i and α_i are the location and the strength of vortex particle i respectively and N_v is the total number of the vortex particles in the flow field.

Chapter 4

Results and Discussion for Vortex-Body Interaction

4.1 Parallel Blade-Vortex Interaction: Single Vortex

To show the feasibility and accuracy of the method, a number of BVI test cases have been calculated and the results are compared with other numerical and experimental results. The dominant mechanisms during a BVI event are also analysed using the illustration of the unsteady surface pressure distribution and the trajectory of the interaction vortex. For all the cases discussed herein, the interaction vortex is introduced five chord lengths upstream of the leading edge and 160 surface panels are used to represent the contour of the aerofoil.

4.1.1 Rankine vortex model: comparison with the panel method

Three typical cases are calculated for the interaction between a NACA 0012 aerofoil and a vortex modelled by the Rankine core in which the constant distribution of vorticity is assumed. The strength Γ_v and the core radius R_v of the clockwise vortex are 0.2 and 0.1 respectively. The only difference among these cases is the initial vertical position Y_v of the vortex: for the first two cases, the interaction vortex is positioned either slightly below the aerofoil ($Y_v/c = -0.26$) or above the

aerofoil($Y_v/c = 0.26$), while for the third test case, the vortex approaches the aerofoil along the chordline($Y_v/c = 0$ or head-on case). In the calculation, the vortex is represented by 961 vortex particles with $\sigma_v = 0.0032$.

Figures 4.1 and 4.2 show the development of the unsteady pressure distribution along the lower surface and the upper surface of the aerofoil respectively for all the cases, which indicates two distinct effects of the interaction vortex on the surface pressure distribution. Firstly, as the vortex approaches the leading edge of the aerofoil, its clockwise circulation induces a downwash on the flow around the aerofoil, particularly near the leading edge, which decreases the incidence of the local flow. As a result, a leading edge suction peak develops on the lower surface, reaching a maximum just before the vortex passes the leading edge. Then, the effective incidence begins to reduce in magnitude and subsequently change sign, resulting in a rapid collapse and reversal of the peak leading edge surface pressure. On the upper surface of the aerofoil, however, an opposite trend is exhibited in the leading edge surface pressure development. Meanwhile, the magnitude of the suction peak and its location are also affected by vortex induced changes in the local speed of the leading edge flow as sketched in figure 4.3 Secondly, as the vortex convects downstream along the surface of the aerofoil, it either accelerates or decelerates the flow close to the surface. As a result, on the lower surface of the aerofoil, a low pressure ridge is clearly visible for cases of $Y_v/c = -0.26$ and $Y_v/c = 0$; on the upper surface, a high pressure ridge can be identified for the cases of $Y_v/c = -0.26$ and $Y_v/c = 0$.

All the surface pressure distributions shown above are integrated from the pressure coefficient at a reference point calculated by the method developed in the present study. If the pressure coefficient at the stagnation point is still assumed to be 1.0 as the vortex approaches the leading edge, then another pressure ridge will appear as shown in figure 4.4 for the head-on case.

Figure 4.5 illustrates the integrated forces and quarter chord moment on the

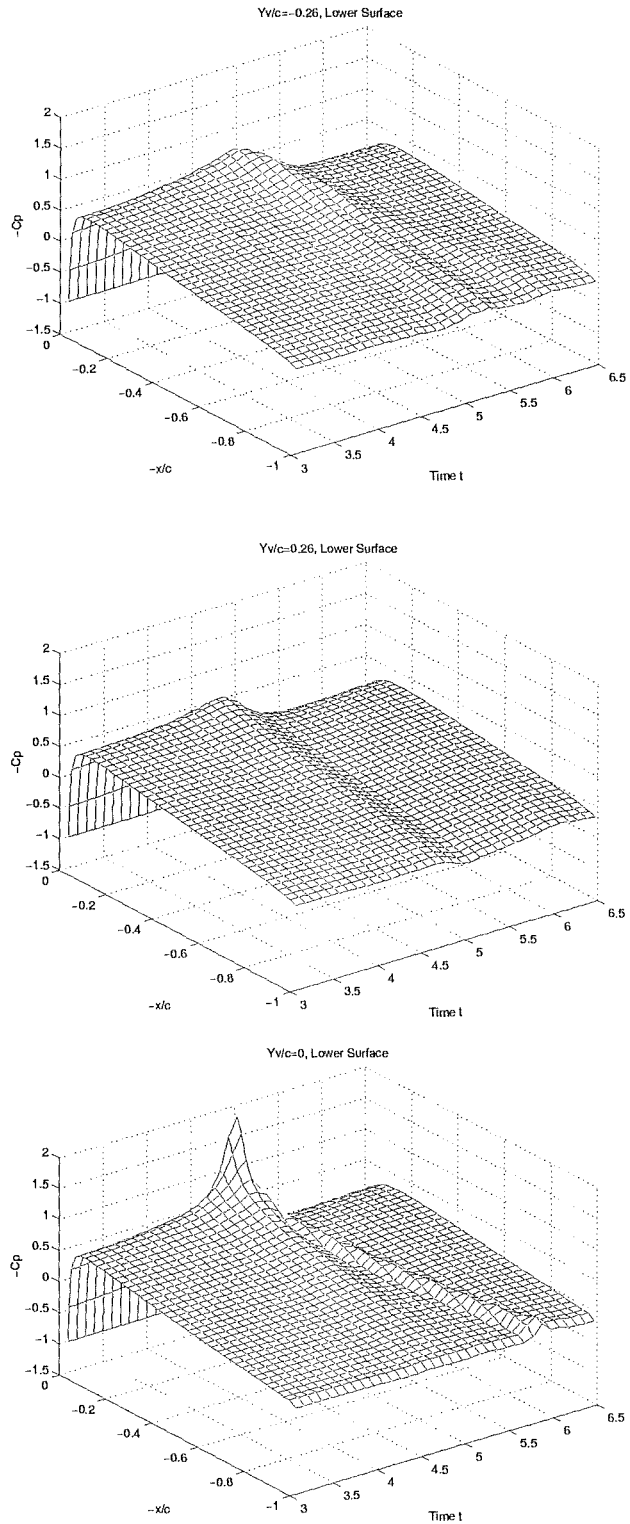


Figure 4.1: Surface pressure distribution during BVI at the lower surface of a NACA 0012 aerofoil for three initial vertical positions of the interaction vortex

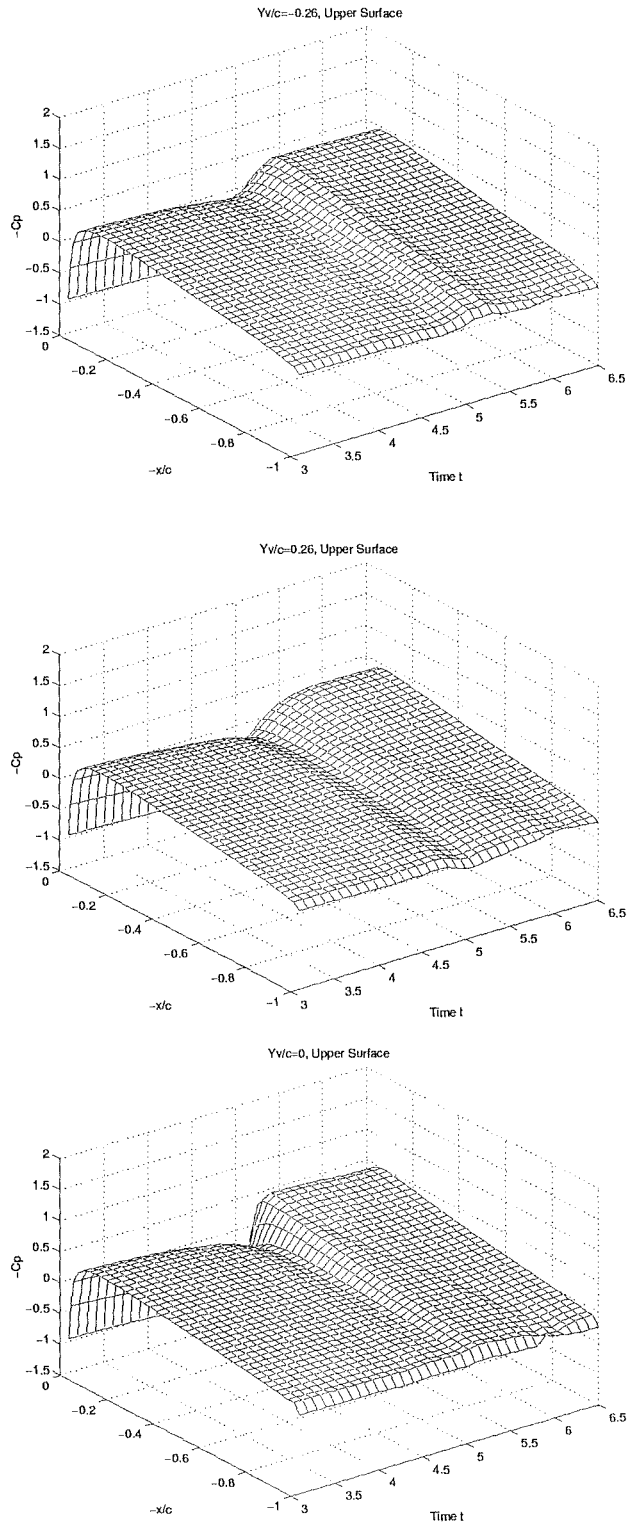


Figure 4.2: Surface pressure distribution during BVI at the upper surface of a NACA 0012 aerofoil for three initial vertical positions of the interaction vortex

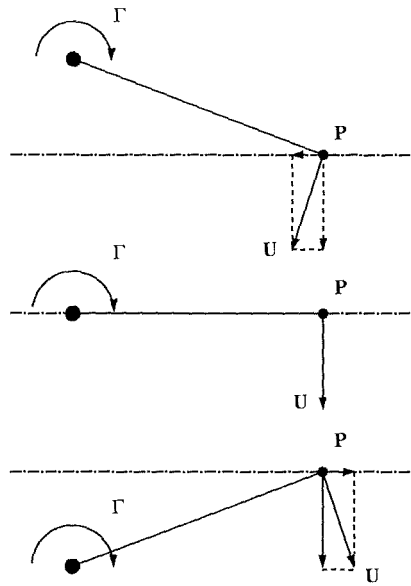


Figure 4.3: Effects of initial vertical position of the oncoming vortex on the induced velocity near the leading edge

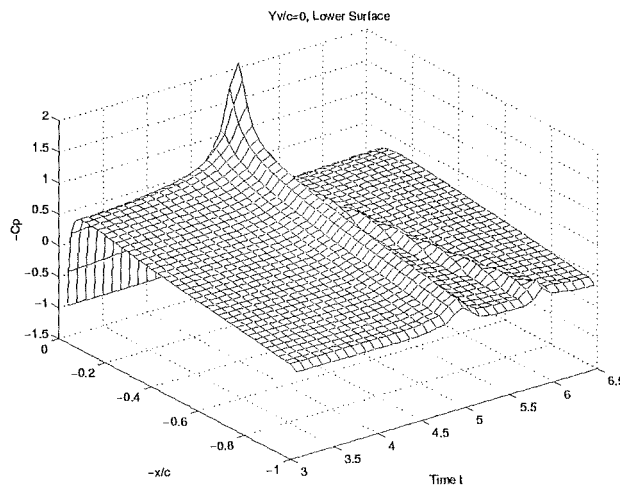


Figure 4.4: Surface pressure distribution during BVI at the lower surface of a NACA 0012 aerofoil without modification of stagnation point pressure coefficient

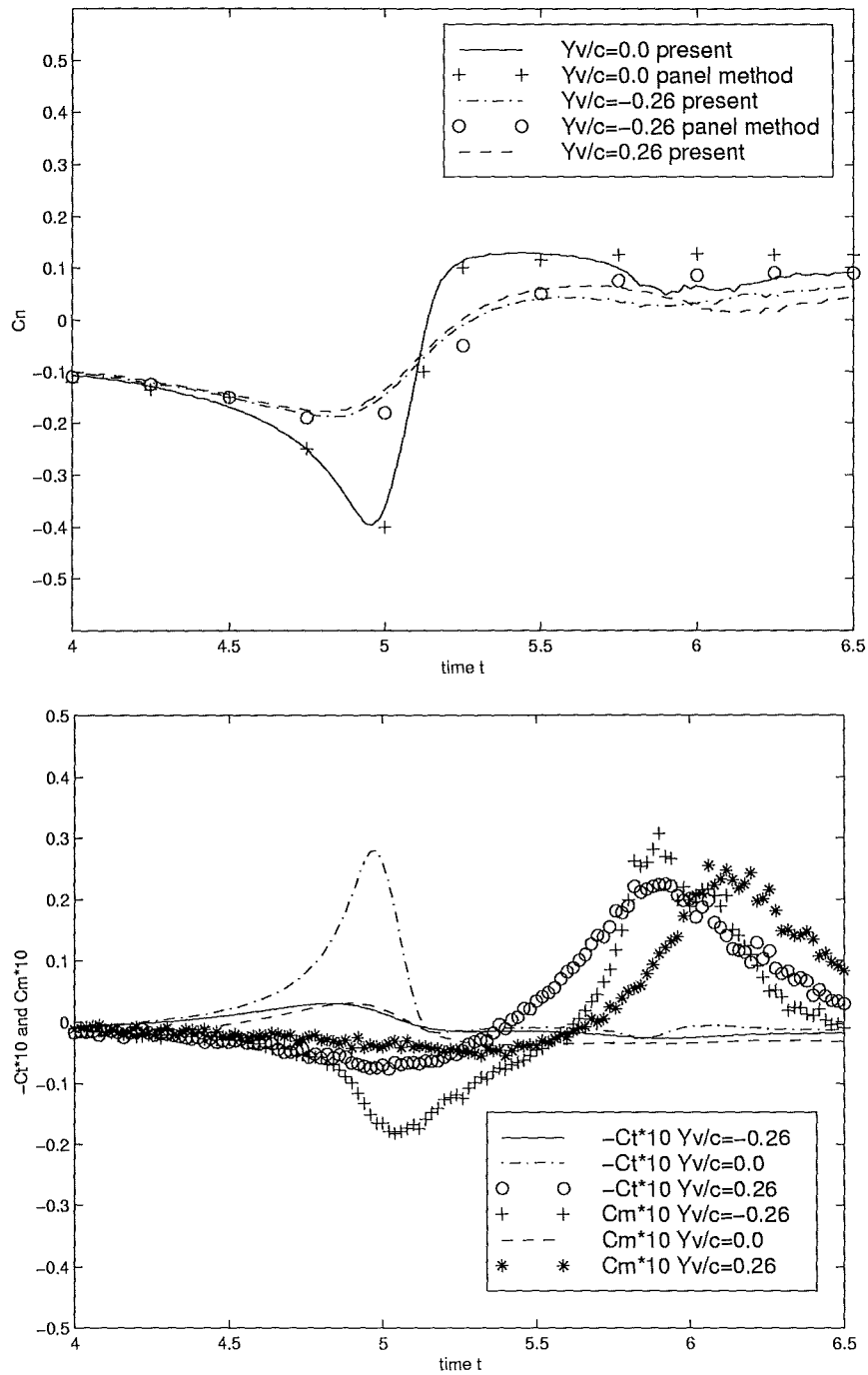


Figure 4.5: Evolution of the aerodynamic coefficients during BVI for three initial vertical positions of the interaction vortex and comparison with the panel method[63]

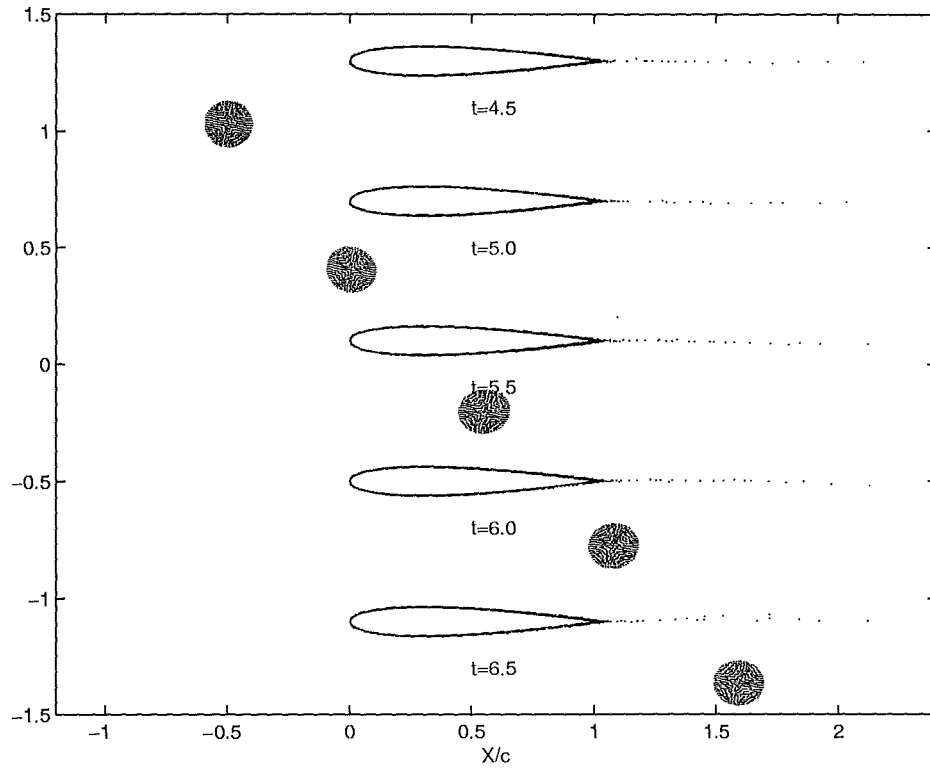


Figure 4.6: The trajectory of vortex particles during BVI for $Y_v/c = -0.26$

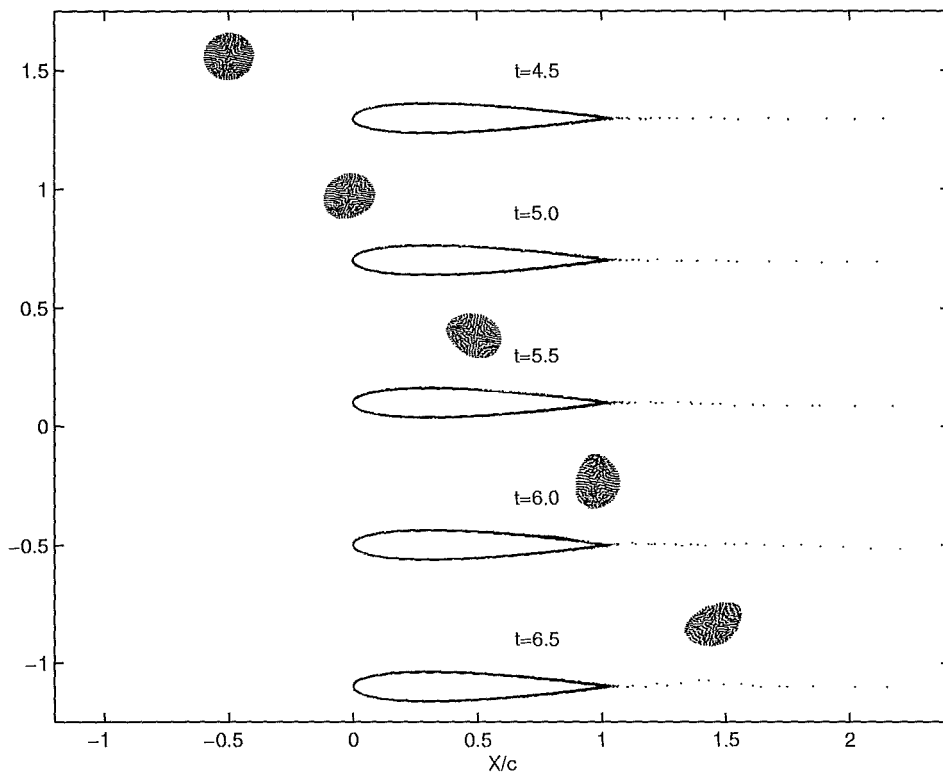


Figure 4.7: The trajectory of vortex particles during BVI for $Y_v/c = 0.26$

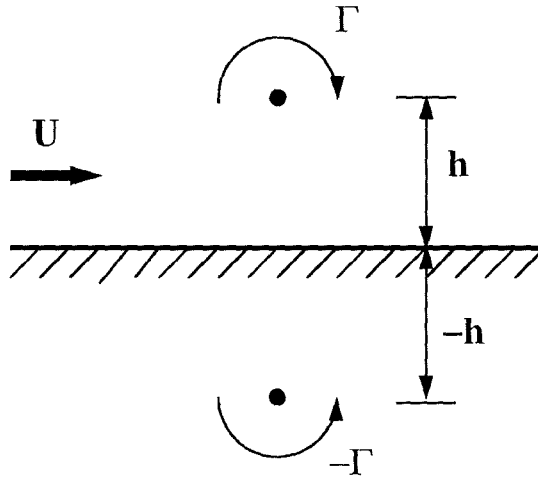


Figure 4.8: Effect of induced surface vorticity on convection velocity of the vortex

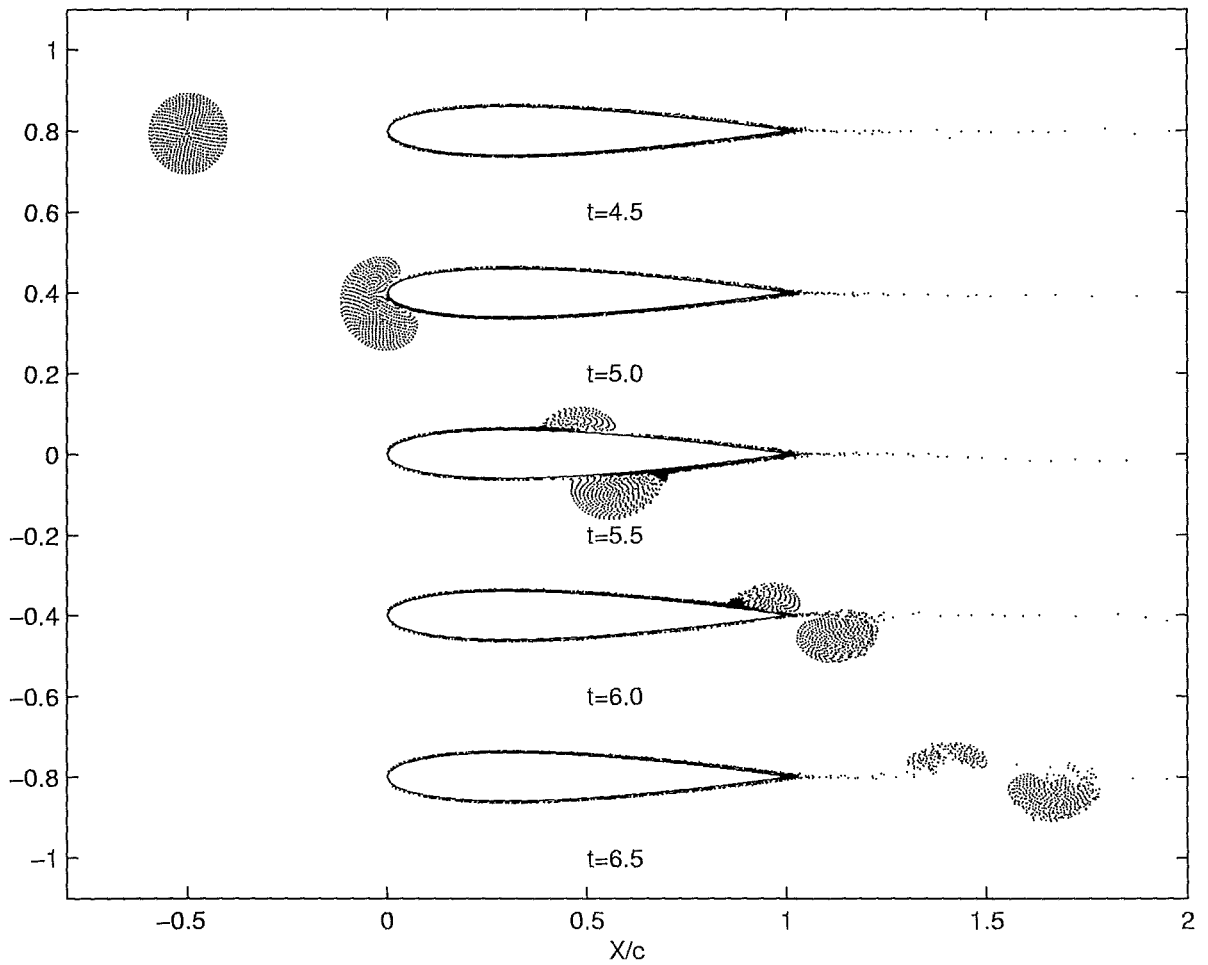


Figure 4.9: The trajectory of vortex particles during BVI for $Y_v/c = 0.0$

aerofoil during the interaction. The development and collapse of the C_n and C_t as well as the first peak in $C_{m\frac{1}{4}}$ can be explained by the effective incidence induced by the vortex, while the second and opposite peak in $C_{m\frac{1}{4}}$ is due to the extended moment arm as the low pressure wave travels along the aerofoil surface. The results also demonstrate the effect of the vortex height Y_v/c on the strength of the interaction: the closer the vortex is to the aerofoil, the stronger are its effects on the aerofoil forces and moment. In figure 4.5, normal force coefficients from the unsteady panel method[63] for the two cases are also given, indicating good agreement between the two methods.

Figure 4.6 and 4.7 give five snapshots of the trajectory of the vortex during the interaction for the first two cases. By comparing these pictures, it can be seen that for the case of $Y_v = 0.26$ the vortex travels above the aerofoil at a speed slightly lower than that for the case of $Y_v = -0.26$. This can be explained by the mutual interaction between the passing vortex and the induced surface vorticity. A simple model problem for a two-dimensional vortex with clockwise rotation convected in a uniform flow above a wall is sketched in figure 4.8. To satisfy the no-penetration condition at the wall, a mirror vortex is placed beneath the wall with the opposite rotation, thus qualitatively, the vortex will convect at a reduced speed. If the rotation of the original vortex is anticlockwise, then it will travel above the wall with an increased velocity. This fact is also attributed to the lag in the second peak of the $C_{m\frac{1}{4}}$ for $Y_v = 0.26$ case. Another phenomenon associated with the close interaction, particularly for the head-on case, is the vortex striking the leading edge of the aerofoil and subsequently deforming and splitting into two fragments, see figure 4.9. Again, the two separate parts of the vortex convect along the upper and lower surfaces with different velocities due to the reason discussed above[31]. Moreover, due to the strong interaction between the oncoming vortex and the surface vorticity, a small local separation is predicted on the aft part of both surfaces where the

adverse pressure gradient dominates. This phenomenon could not be predicted in the panel method, in which the vorticity is shed from the trailing edge only, and is probably responsible for the small discrepancy in C_n between the two methods as the vortex travels off the aerofoil.

4.1.2 Scully vortex model: Comparison with experimental data

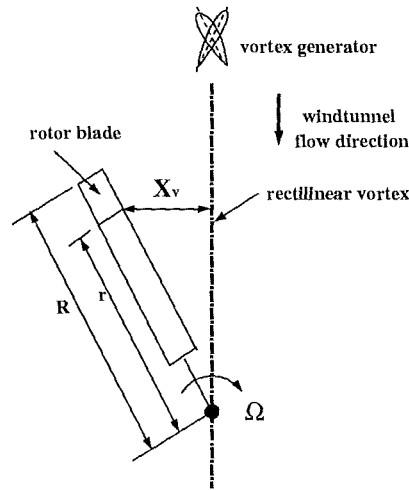


Figure 4.10: The set-up of BVI wind tunnel test at Glasgow University

The set up of the Glasgow BVI experiment [43][44][74] is sketched in figure 4.10. The interaction vortex is generated by two adjoining wings of NACA 0015 aerofoil section set at equal but opposite incidence, with the magnitude of the incidence controlling the vortex strength. The circumferential velocity distribution in the isolated interaction vortex is measured using both hot wire and PIV techniques, which gives an average value of the vortex strength $\Gamma_v = 5.8\text{m}^2/\text{s}$ and core radius $R_v = 25\text{mm}$. These data are then used as the input parameters for the present simulation by employing the Scully vortex model. Although the flow around the rotating rotor is generally three-dimensional, it could be considered approximately two-dimensional as the rotor blade at zero angle of attack approaches and passes through the inter-

action region near the center line of the wind tunnel. In the following discussion, the data collected from the blade at $r/R = 0.785$ are used for the comparison. The pressure and the integrated aerodynamic forces and moment are nondimensionalised using the tip velocity of the rotor which gives a nominal Reynolds number of 600,000. In these calculations, the entire interaction vortex is discretized into 7569 vortex particles with a core radius $\sigma_v = 0.0060$.

Figure 4.11 illustrates the results for three typical BVI cases with different interaction heights, from which it can be seen that C_n and C_t agree well with the experiments, whereas there are some discrepancies in the $C_{m\frac{1}{4}}$ data for all cases as the vortex passes the aft part of the aerofoil surface. Due to the fact that the present prediction gives results consistent with the mechanisms discussed in the previous section, the difference in $C_{m\frac{1}{4}}$ may be due to the relatively small number of pressure transducers (only twenty-six for this case) used for measuring the pressure distribution around the aerofoil, while the $C_{m\frac{1}{4}}$ value itself is very small and is therefore sensitive to the resolution of the pressure measuring points. Another possibility is the physical restrictions in placing the transducers at the trailing edge of the blade [74]. Nevertheless, further study is needed to clarify this aspect.

In figure 4.12, two snapshots of the vortex passage for the head-on case are given, which also show that the interaction vortex is deformed and split into two parts which convect along the upper and lower surface at different speeds. On the aft part of the aerofoil surface, the vortex induced local flow separation is clearly visible, which is consistent with the PIV results[44] for the same case.

Figure 4.13 gives the upper surface pressure distribution for the $Y_v/c = 0.1$ case, which compares well with the experimental result given in [74]. The leading edge pressure suction peak and low pressure convection ridge are also well predicted.

To examine the effect of initial vertical position of the vortex on the strength of interaction, a number of calculations have been carried out for different values

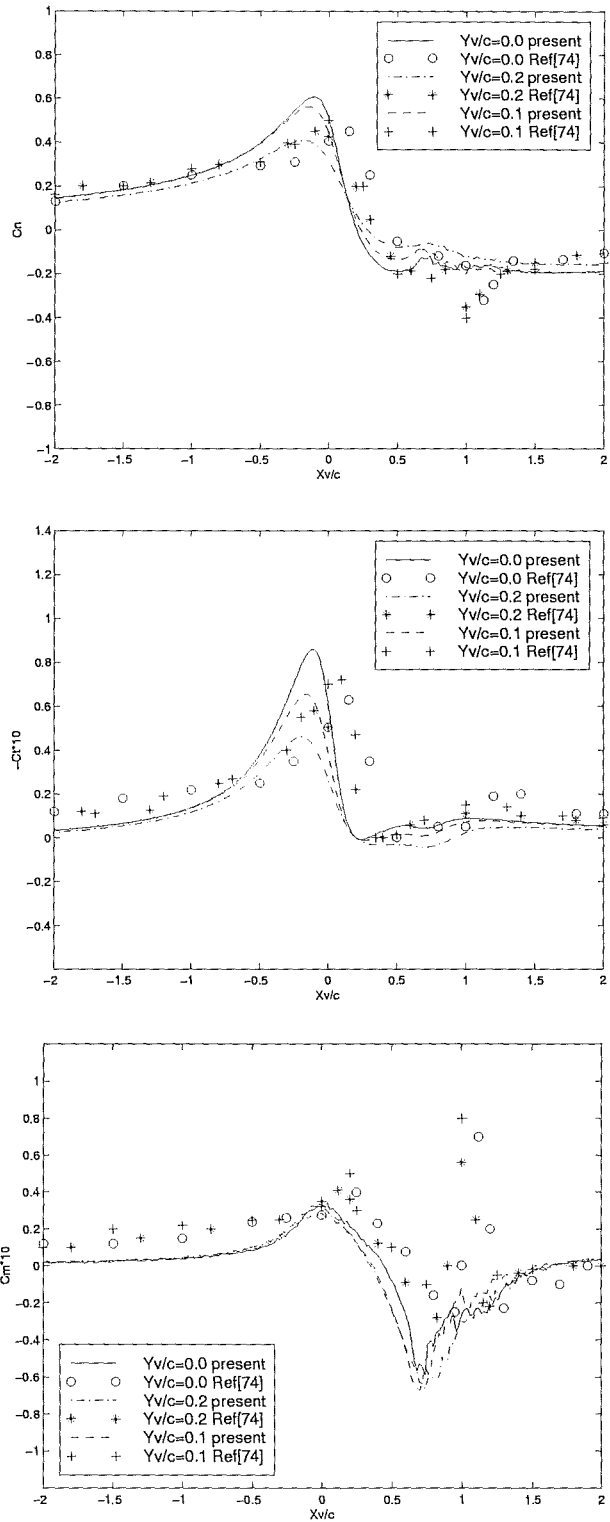


Figure 4.11: Evolution of aerodynamic coefficients during the BVI and comparison with the BVI test from [74]

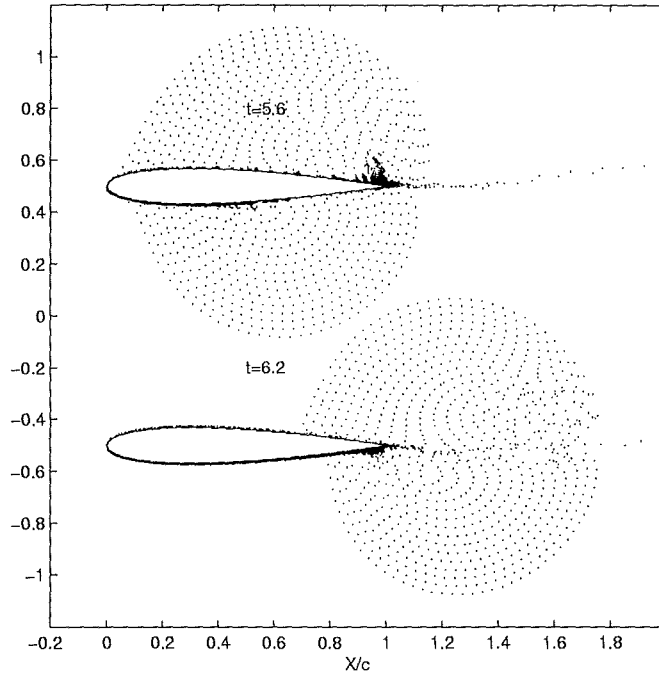


Figure 4.12: Vortex induced local flow separation: trajectory of the vortex particles for $Y_v/c = 0.0$

of Y_v/c . The strength of interaction is measured by ΔC_n which is the absolute difference between the maximum and minimum C_n values. The results are illustrated in figure 4.14, from which it is shown that for the flow with zero angle of incidence, the strongest interaction happens in the head-on BVI case. As the absolute value of Y_v/c increases, the value of ΔC_n at first decreases quickly, then at a reduced rate. It is also found that the ΔC_n curve is not symmetric about the origin point $Y_v/c = 0$, particularly when the value of $|Y_v/c|$ is greater than 0.2, which may be explained by the vortex induced asymmetric effect on the flow velocity near the leading edge as shown in figure 4.3. The results from the BVI test have also been plotted in figure 4.14, in which the maximum ΔC_n , which is slightly bigger than the present prediction, occurs at the $Y_v/c = 0.1$ test setting. This difference is mainly due to the fact that in the results of the BVI tests, a further dip in C_n occurs as the vortex travels off the trailing edge of the aerofoil, see figure 4.11, which is not predicted in

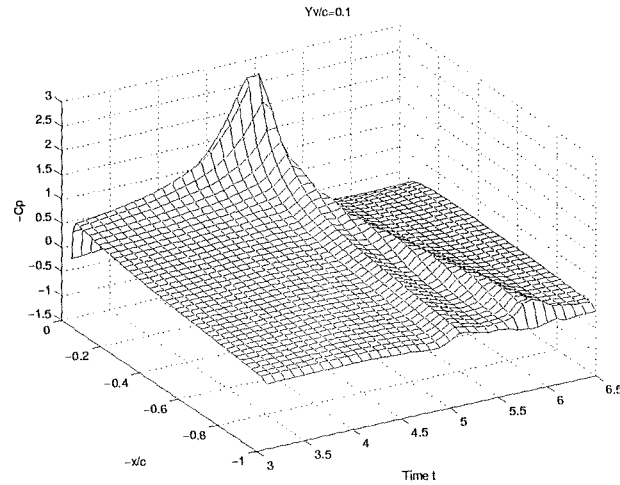


Figure 4.13: Upper surface pressure distribution during BVI for $Y_v/c = 0.1$

the numerical results.

In figure 4.14, the ΔC_n vs Y_v/c for cases with non-zero incidence are also illustrated. While a small successive increase in the maximum ΔC_n can be found for $\alpha = 6^\circ$ and 12° cases, a noticeable shift in its location is predicted, which conflicts with the experimental results shown in the same figure. One problem associated with the BVI wind tunnel test is that, due to vortex meander during the test, it is difficult to determine the exact value of Y_v/c and hence the location of the maximum ΔC_n . This is particularly the case for a close interaction[74], which could be responsible for the difference between the numerical results and the experiments.

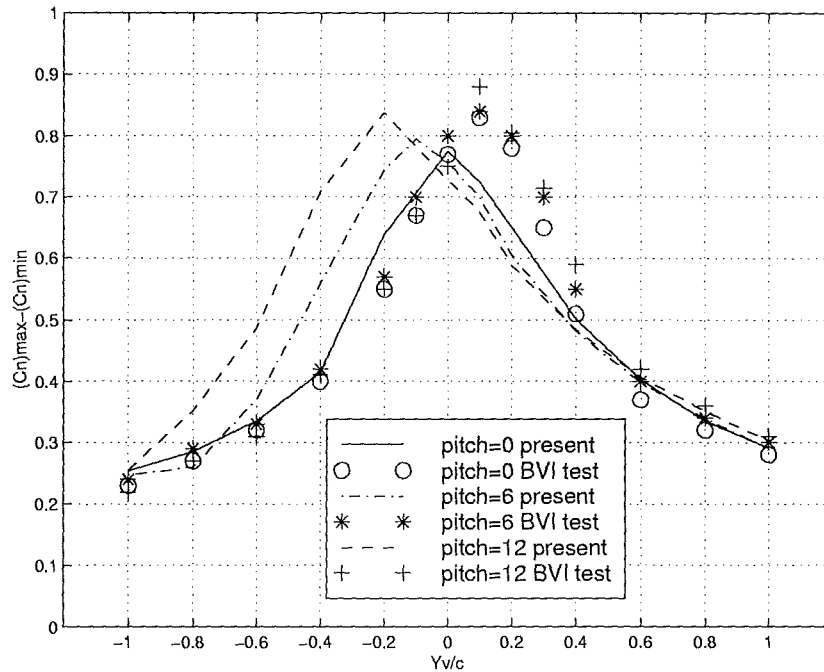


Figure 4.14: Effects of initial vertical position and flow incidence on ΔC_n : a comparison with the BVI test[71]

4.2 Parallel Blade-Vortex Interaction: Twin Vortices

In this section, some results for a twin vortex system interacting with a NACA 0015 aerofoil set at zero angle of incidence are presented.

Two vortices with finite core radii and same direction of rotation are shown to interact with each other in a complicated way. Depending on the initial separation distance and the strength and core radius of the vortex, they may rotate around each other as do two point vortices, or merge into a single vortex[23]. Between these two situations, a critical distance exists, at which the vortices alternately approach each other and draw apart; in this process, they exchange vorticity. For the cases in which two vortices are close enough to each other, a substantial deformation of the vorticity field will normally occur during the evolution of the twin vortex system. Therefore, unlike a single vortex BVI event, a twin vortex system interacting with an

aerofoil will very much depend on the initial location of the vortices. In the present study, this can be described by the position of the center of the twin vortex system (x_c, y_c) , the separation distance between vortices S_l and the angle θ between the line through the centres of the two vortices and the horizontal, as shown in figure 4.15.

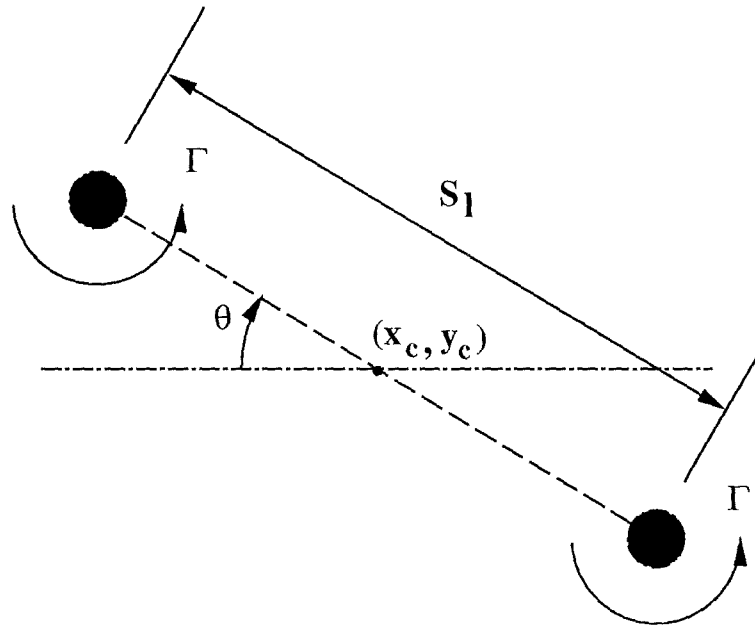


Figure 4.15: Definition sketch of initial position of the twin vortex system

To resemble the twin BVI tests carried out at Glasgow University, the unsteady development of a twin vortex system with anticlockwise rotation of vorticity and separation distance of a chord length are studied. The strength Γ of each vortex is $2.9m^2/s$, half that of the single vortex used in the previous section and the core radius R_v is 20mm, which is smaller than the single vortex. Like the single vortex, the twin vortices are also modelled by the Scully vortex model and each vortex is represented by 5041 vortex particles. Figure 4.16 gives 6 snapshots of the trajectory of the vortex particles, which shows that under the given conditions, the two vortices rotate about the center of the system at a very low frequency: the half period is about 24-25 in nondimensional time. The center of the system is initially placed at the point $(-4.5, 0)$, thus as the first vortex reaches the leading edge of the aerofoil,

the system will have rotated anticlockwise about 30° .

To examine the effect of the initial position of the twin vortices, namely the value of θ , on the strength and characteristics of the interaction, six cases with $\theta = 0^\circ, 30^\circ, 60^\circ, 90^\circ, 120^\circ, 150^\circ$, have been calculated. Figure 4.17 gives the aerodynamic forces during the interaction for all the cases, from which two extreme cases can be identified. In the first case, which is represented by $\theta = 30^\circ$, two peaks in C_n and C_t are predicted, which correspond to the arrival of the tandem vortices at the leading edge of the aerofoil at a time interval of nearly 1.0. Figure 4.19 gives several snapshots of the vortex trajectory for this particular case, which clearly shows that the two vortices reach the leading edge nearly along the chord line and then each splits into two segments. The absolute value of the first peak in the aerodynamic force is far greater than the second one due to the combined contribution from both vortices as the first vortex reaches the leading edge area while, as the second vortex reaches the leading edge of the aerofoil, it is already under the negative influence of the first vortex. Consistent with the head-on single vortex BVI, this case, in terms of ΔC_n , also corresponds to the strongest interaction. In the second typical twin vortex BVI case, illustrated here by $\theta = 90^\circ, 120^\circ, 150^\circ$ cases, only one peak in C_n and C_t history is present, a situation quite similar to the single vortex BVI. By examining the trajectory of the vortices for $\theta = 120^\circ$ case, see figure 4.20, it is revealed that two vortices arrive at the leading edge of the aerofoil nearly at the same time: one is above the aerofoil, the other is below the aerofoil. So there is no time lag effect of the vortices as presented in the first case. The effects of the initial position of the vortices are also reflected in the quarter chord moments $C_{m_{\frac{1}{4}}}$, which are presented in figure 4.18 .

Figure 4.21 illustrates the upper and lower surface pressure data for the $\theta = 30^\circ$ case. The passage of the two vortices is clearly visible from the twin suction peaks and subsequent vortex convection ridges. The relative magnitudes of the convection

ridge implies that the first vortex passes closer to the upper surface of the aerofoil, which is evidenced in figure 4.19. For the purpose of comparison, a similar C_p result from the BVI test is shown in figure 4.22. A good agreement has been achieved, in terms of the values of the suction peaks and the convection ridges, between the numerical result and the test. While in the numerical simulation, the vortex separation remains approximately constant during the interaction, the BVI test gives a slightly increased distance between the vortices which was thought to be due to the influence of the rotor on the twin vortex system[28].

In figure 4.23, the surface C_p distribution for the $\theta = 120^\circ$ case is shown. The passage of both vortices is also visible from the upper surface low pressure ridge and low surface high pressure valley. Because the vortices travel above the upper surface and below the lower surface simultaneously, only one pressure suction peak is present in this case.

In figure 4.17, the C_n data corresponding to the pressure distribution in figure 4.22 from the BVI test are also plotted, which compares well in trend with the $\theta = 30^\circ$ case. Because of the unsteady development of the twin vortex system and the strong interference of the rotor blade on the surrounding flow field, in the twin BVI wind tunnel tests it is extremely difficult to determine the twin vortex locations during the interaction and remove the 3-D effect of the rotor blade. Therefore some differences in C_n , in both magnitude and the location of peak values, between the simulation and the BVI tests are not unexpected. Indeed, each run of the twin BVI test gives a different C_n result [74] and the differences caused by the effects mentioned above are further evidenced by comparing the twin BVI test with the results for single BVI: the maximum value of C_n obtained in twin BVI test is nearly the same as the single vortex BVI. However, in the present numerical simulation, substantial reductions in both the maximum C_n value and ΔC_n value are predicted for most twin BVI cases compared with the corresponding single BVI cases.

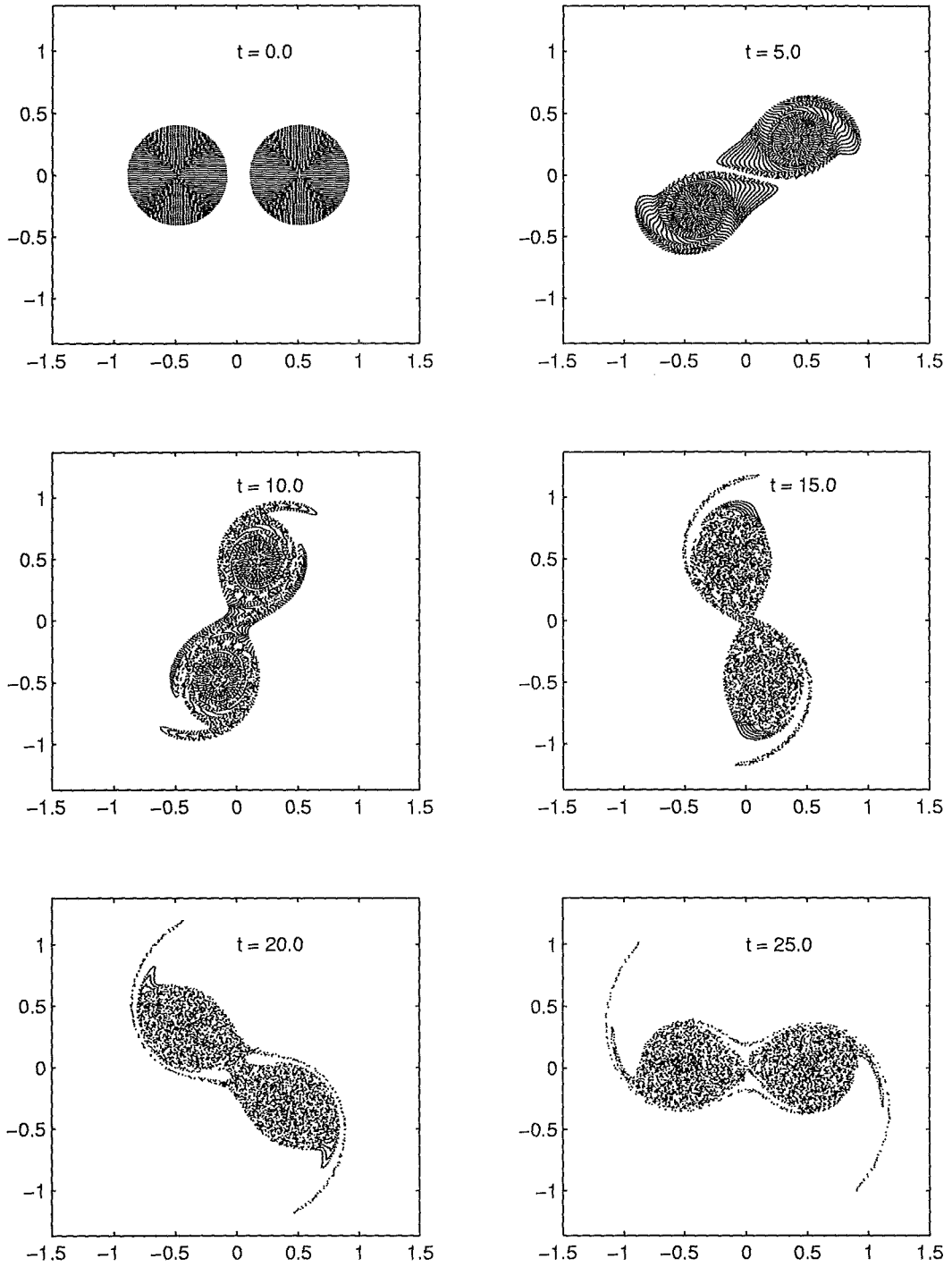


Figure 4.16: Deformation and rotation of a twin vortex system

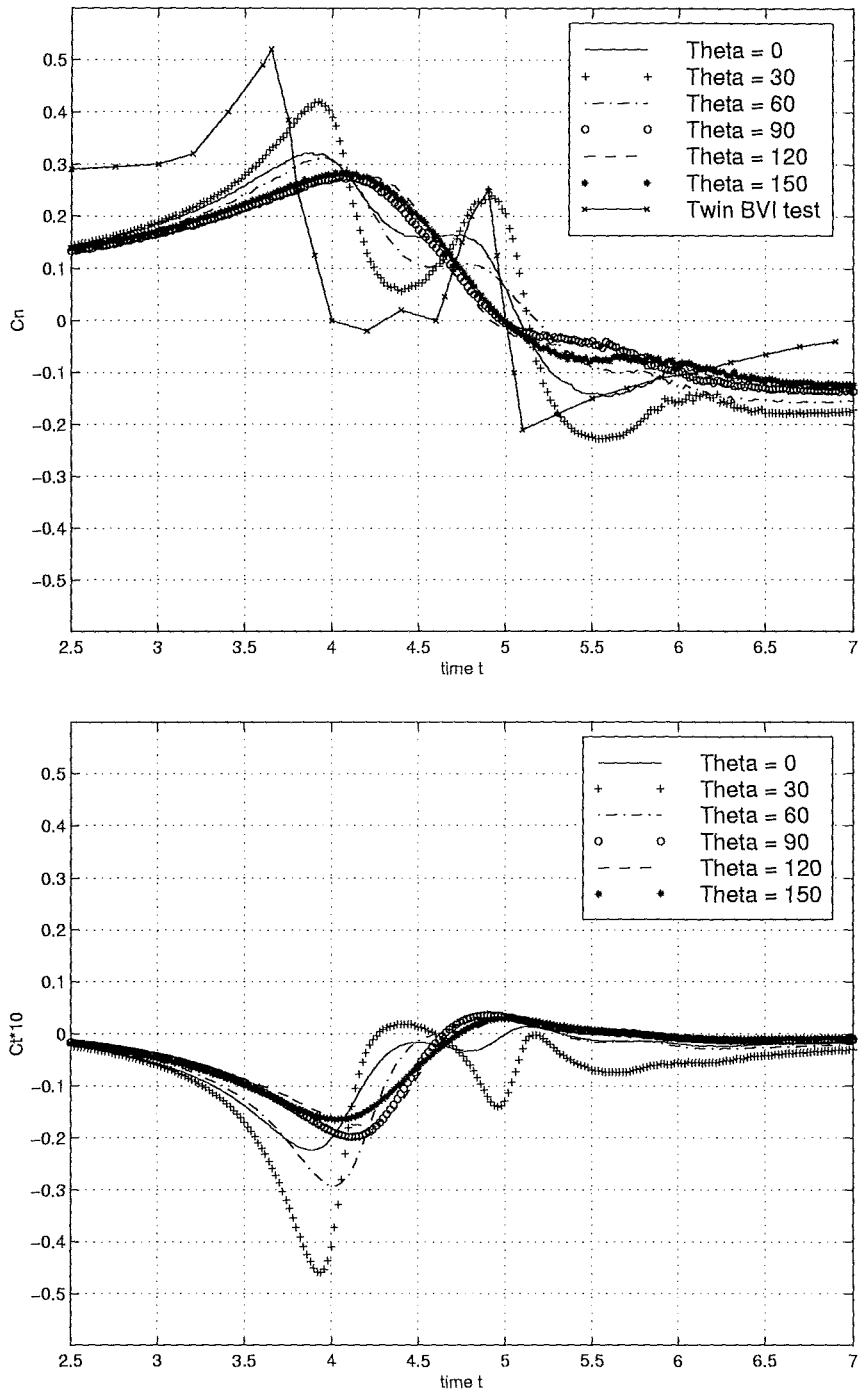


Figure 4.17: Evolution of the aerodynamic forces during the twin BVI and comparison with the wind tunnel test[74]

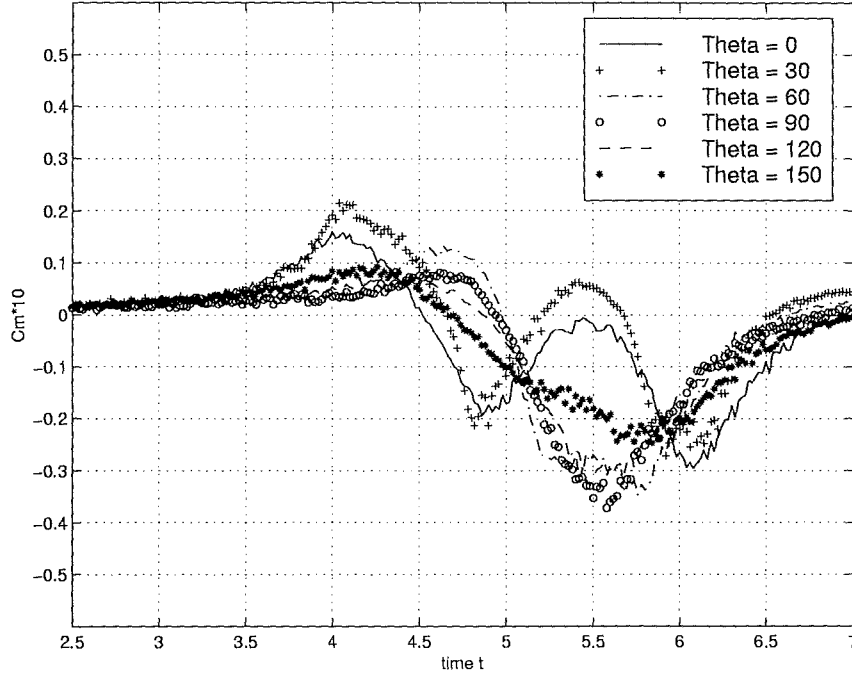


Figure 4.18: Evolution of the quarter chord moments during the twin BVI

4.3 Normal vortex-ring body interaction

4.3.1 Validation of the numerical method

To validate the 3-D vortex particle method discussed in the previous chapter, several test calculations have been carried out.

In the first test, the self-induced velocity or the propagation velocity of a series of thin vortex rings is calculated to examine the accuracy of the velocity computation from a given vorticity field. The strength or the circulation Γ of the ring is set equal to unity and the ratio R/σ varies from 2 to 10. The vortex ring is discretised into N elements along its axis and the number of elements is chosen to yield a given value of overlap ratio. Under the assumption that both σ and σ/R are small, the propagation velocity for vortex rings with a Gaussian cross-section can be calculated by the following analytical formula(Saffman, 1970[94]):

$$\frac{\sigma U}{\Gamma} = \frac{\sigma}{4\pi} \left[\ln\left(\frac{8R}{\sigma}\right) - 0.558 \right] \quad (4.1)$$

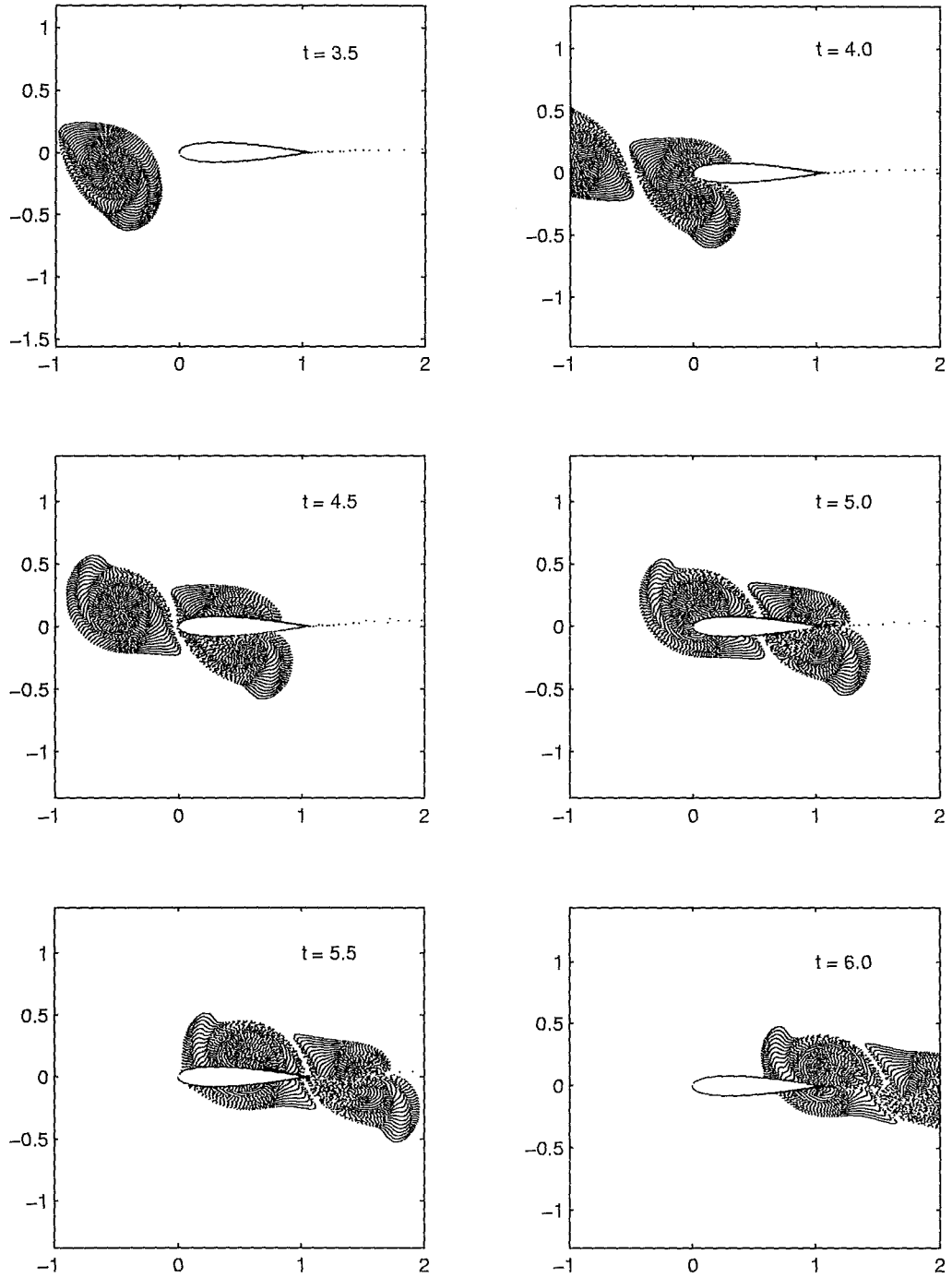


Figure 4.19: Trajectory of vortices during a twin bvi event: $\theta = 30^\circ$

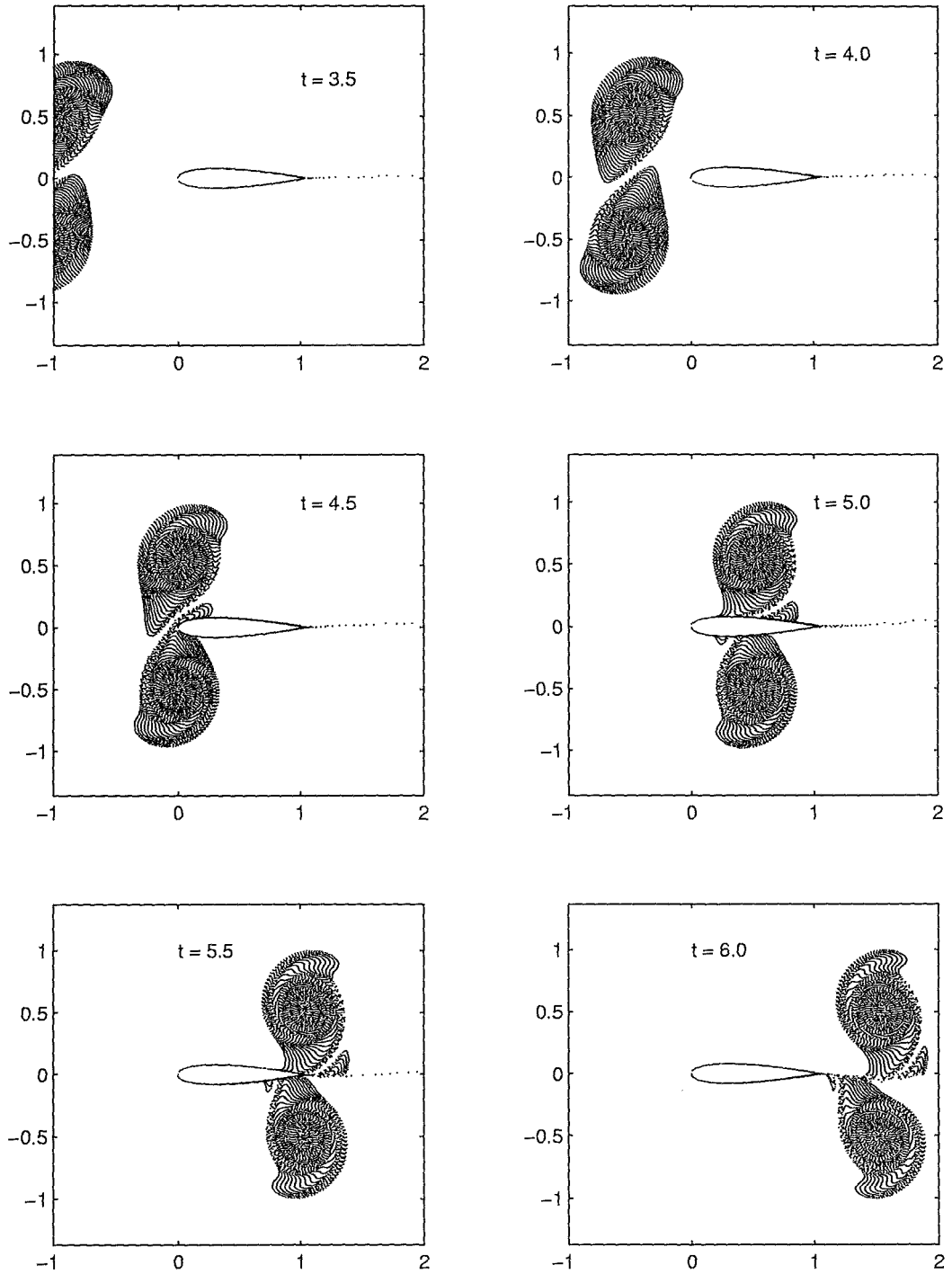


Figure 4.20: Trajectory of vortices during a twin bvi event: $\theta = 120^\circ$

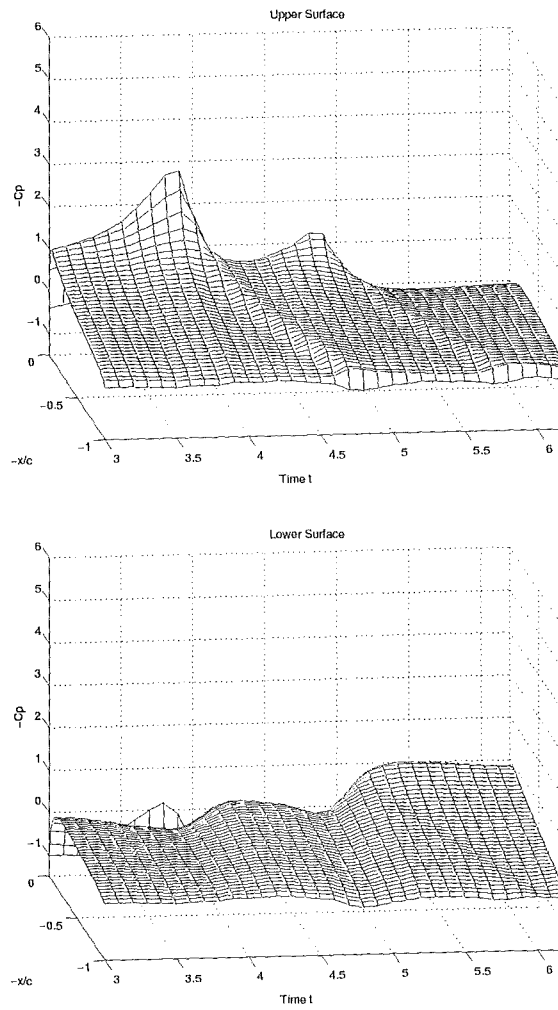
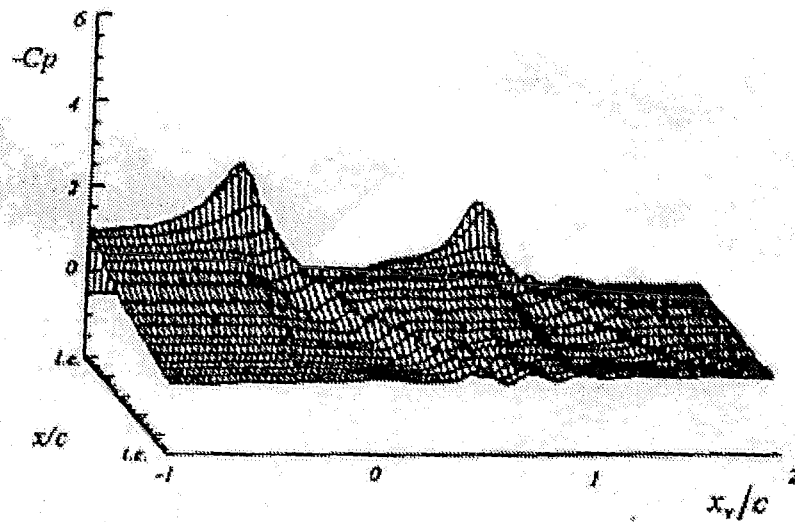
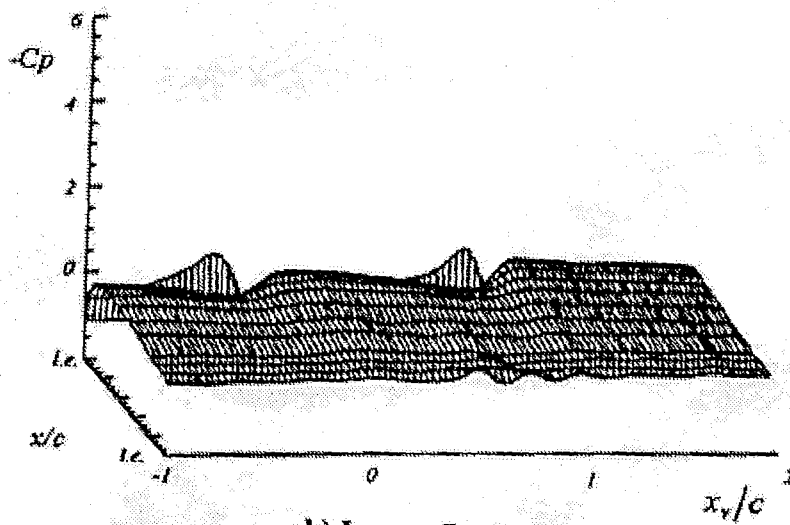


Figure 4.21: Surface pressure distribution during a twin BVI event: $\theta = 30^\circ$



a) Upper Surface



b) Lower Surface

Figure 4.22: Surface pressure distribution during a twin BVI event from the wind tunnel test[71]

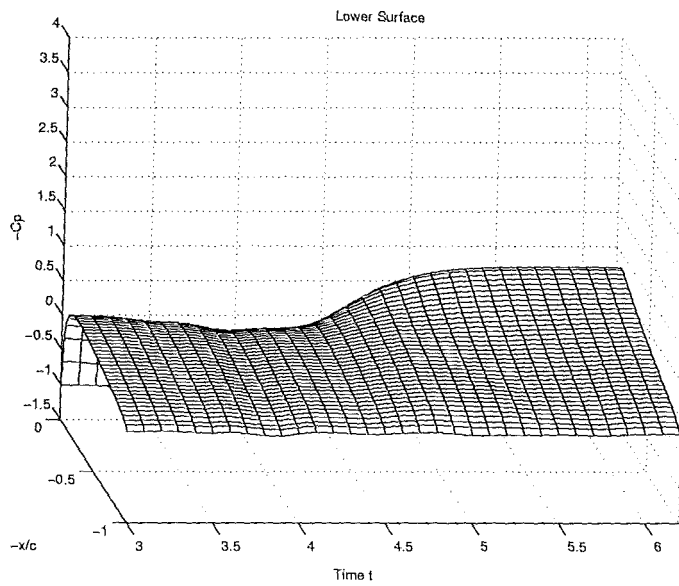
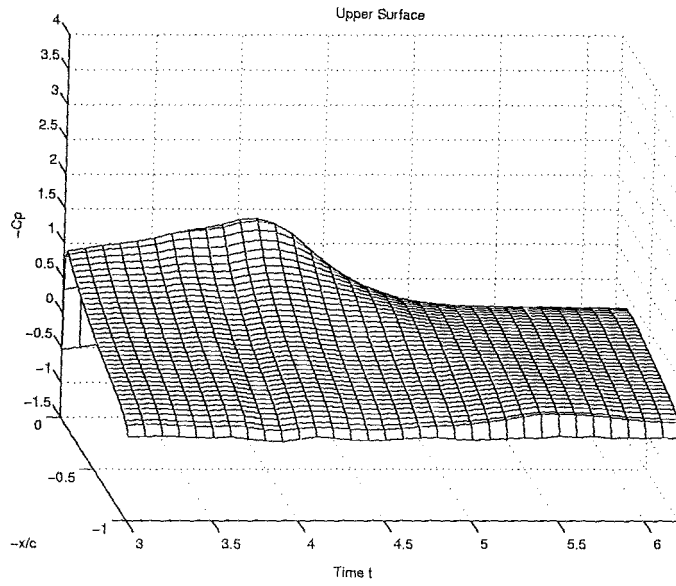


Figure 4.23: Surface pressure distribution during a twin BVI event: $\theta = 120^\circ$

which will be used for comparison with the numerical result. The results from both vortex method and the analytical solution are plotted in figure 4.24 for an overlap of 3, which shows good agreement. The effect of the overlap ratio of vortex particles on the velocity calculation is given in figure 4.25 for a vortex ring with $R/\sigma = 5$, which demonstrates that a certain degree of overlapping is essential for an accurate calculation.

The velocity at the center of the vortex ring is also calculated for $\Gamma = 1$ and $R = 1$, which gives a value of 0.497, very close to the analytical result of 0.5.

In the second test case, the problem of induced force on a sphere due to a vortex ring was studied, as shown in figure 4.26. The radius of the sphere and the vortex ring are 0.5 and 1.0 respectively. The ring vortex is represented by 100 vortex particles with a core radius $\sigma = 0.1$ and the sphere surface is simulated using 1200 source panels. In this calculation, the flow is assumed inviscid and the pressure at the surface is calculated by using the Bernoulli equation under the assumption that the sphere is stationary. This problem can also be solved analytically using Helmholtz's solution for flow induced by a vortex ring together with Butler's sphere theorem[11]. In figure 4.27, both the numerical and analytical solutions are given for the drag coefficient $C_D = drag/2\Gamma^2\pi a^2$, which shows that both the velocity calculation and the body surface discretization algorithms used in the present study are reliable.

4.3.2 Inviscid normal vortex-body interactions

In this section, some preliminary results are presented for normal vortex ring-body interaction problems. In the first case, a circular vortex ring interacting with a blade of NACA 0016 cross-section is studied. As shown in figure 4.29, the vortex ring of ring radius $R = 0.5$ is represented by 6272 vortex particles, which are distributed within the ring in a torus formed of 49 circular curves with 128 vortex particles along each curve. A constant vorticity distribution is assumed within the cross-section of

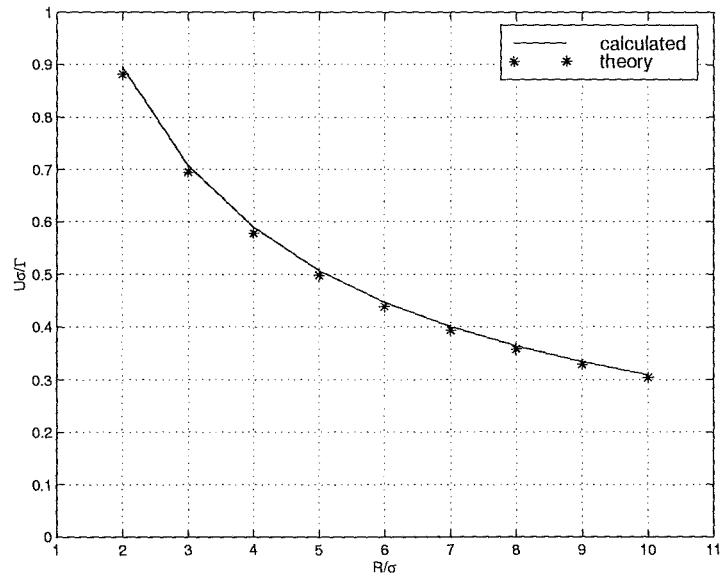


Figure 4.24: Dimensionless self-induced propagation speed of a vortex ring

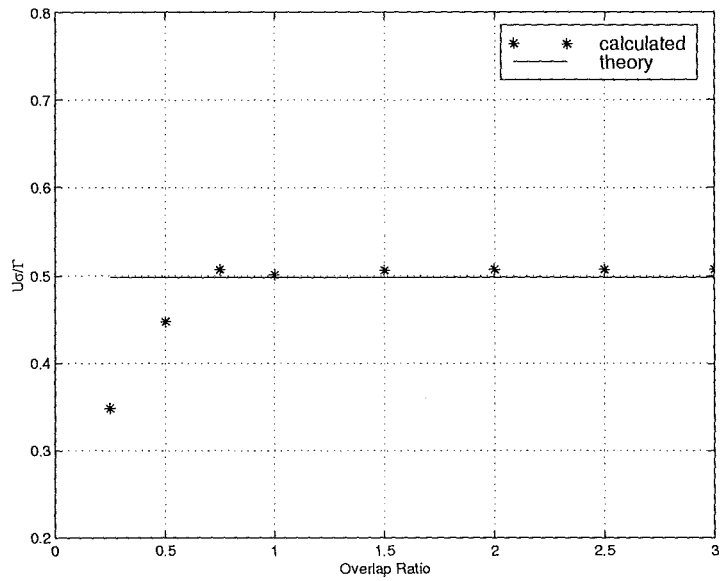


Figure 4.25: Effect of particle overlapping condition on the accuracy of velocity calculation in 3-D vortex particle method

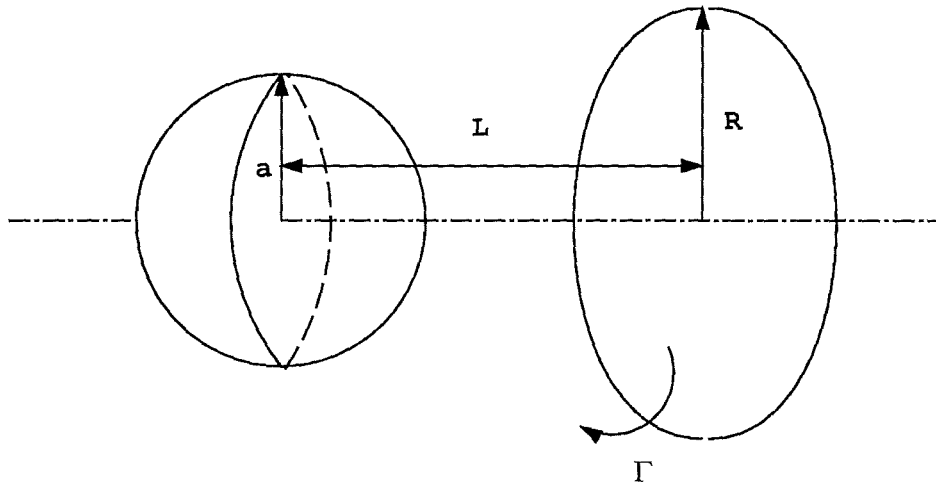


Figure 4.26: Illustration of vortex ring-sphere interaction problem

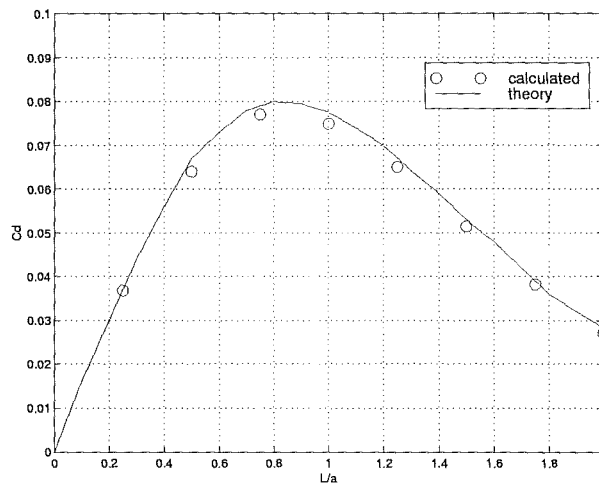


Figure 4.27: Comparison of vortex induced force on body for the vortex ring-sphere interaction problem between present study and Butler's sphere theorem[10]

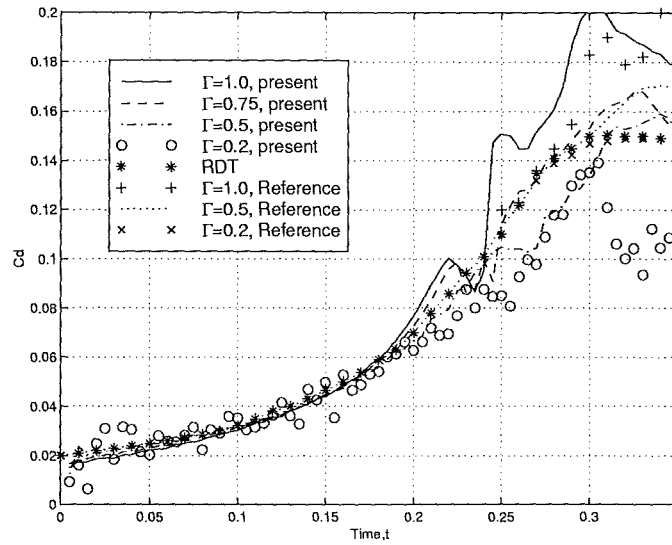


Figure 4.28: Prediction of drag coefficients for the normal blade-vortex ring interaction and comparison with the numerical results from the vorticity collocation method[69]

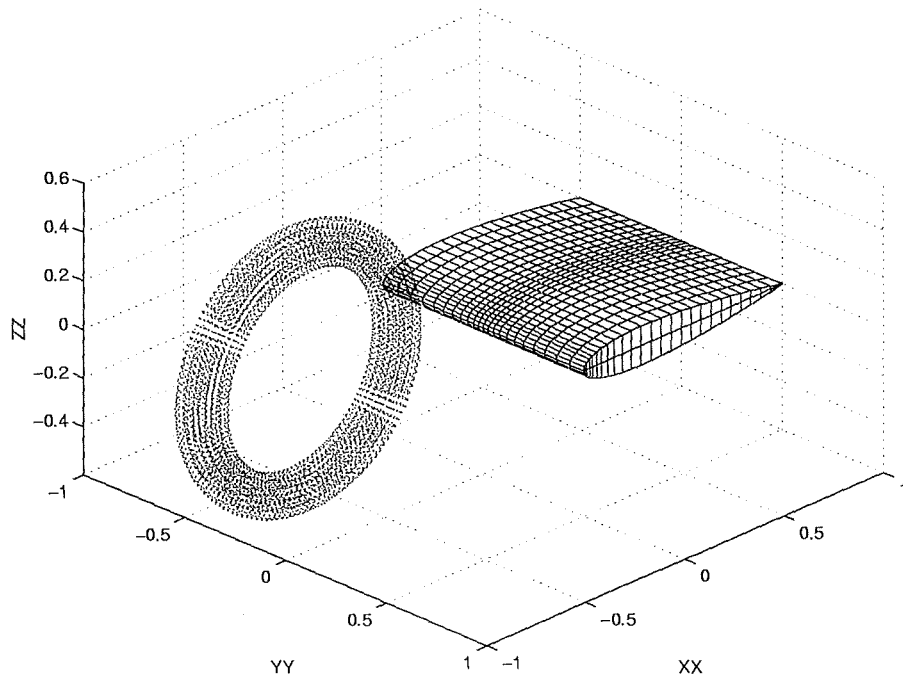


Figure 4.29: Initial position of the vortex ring and surface discretization of the wing for the normal vortex ring-blade vortex interaction problem

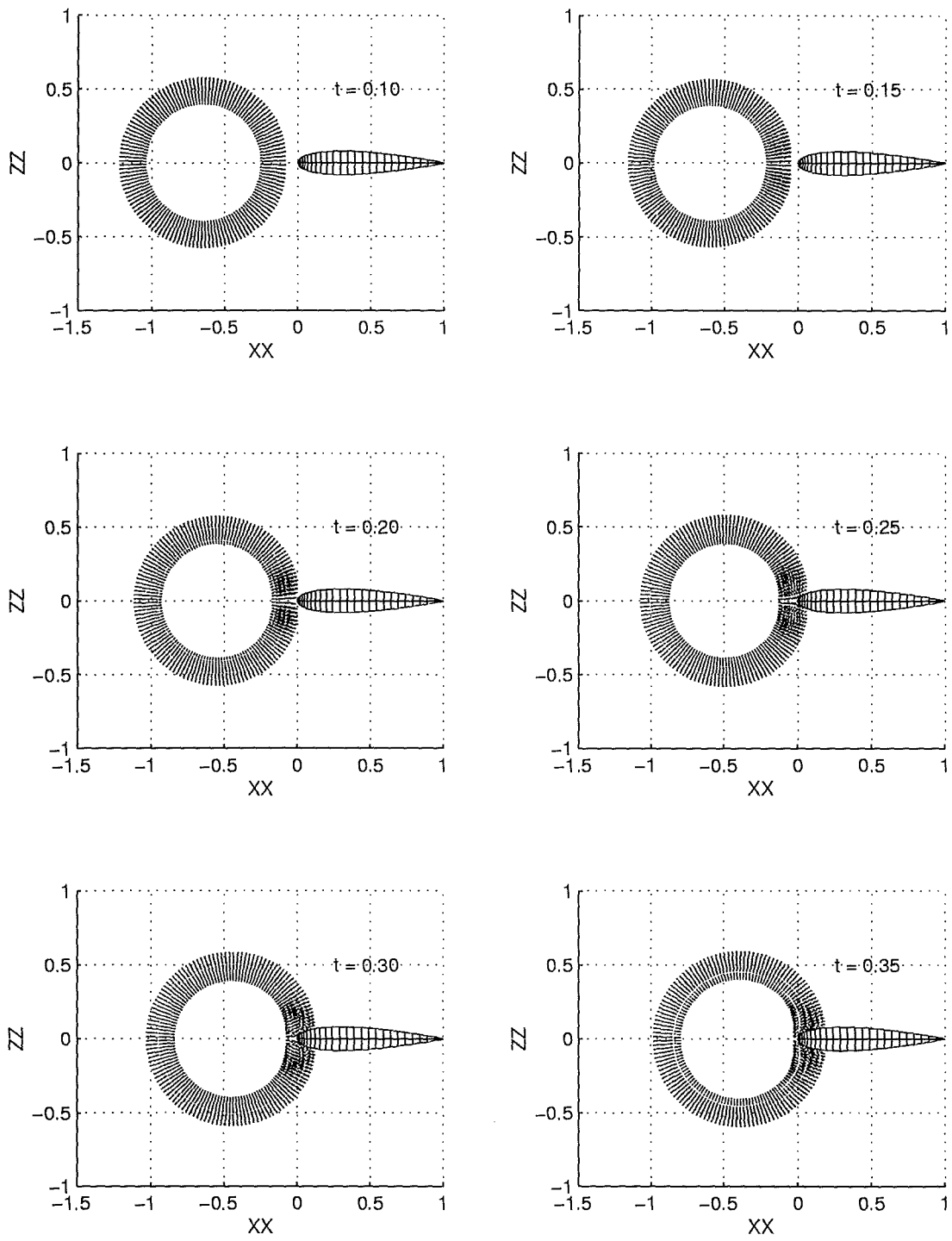


Figure 4.30: Trajectory of the vortex particles during the normal vortex ring-blade interaction

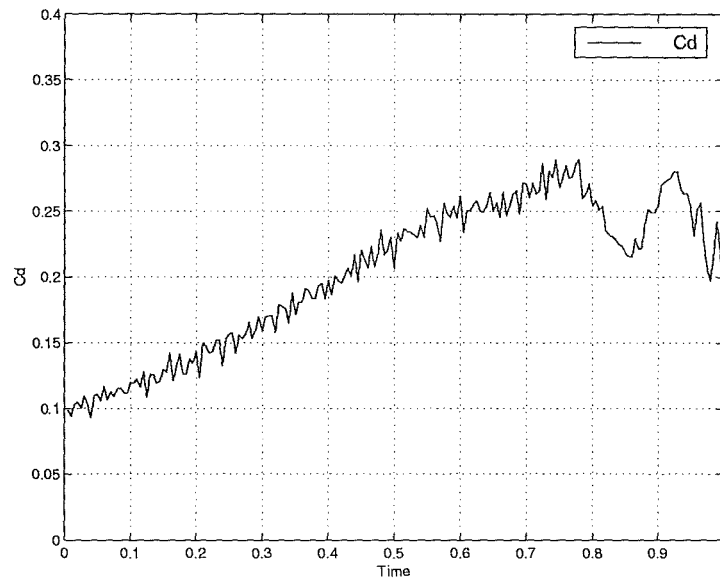


Figure 4.31: Prediction of drag coefficient of the normal interaction between a vortex ring and a sphere

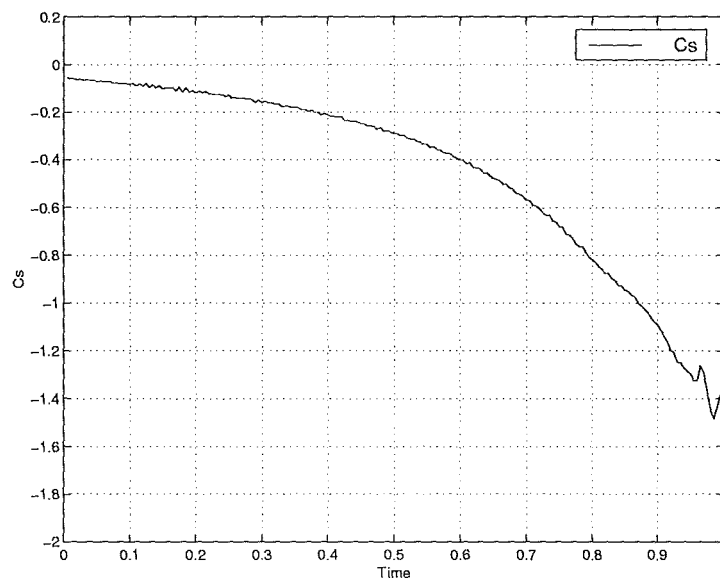


Figure 4.32: Prediction of side force coefficient of the normal interaction between a vortex ring and a sphere

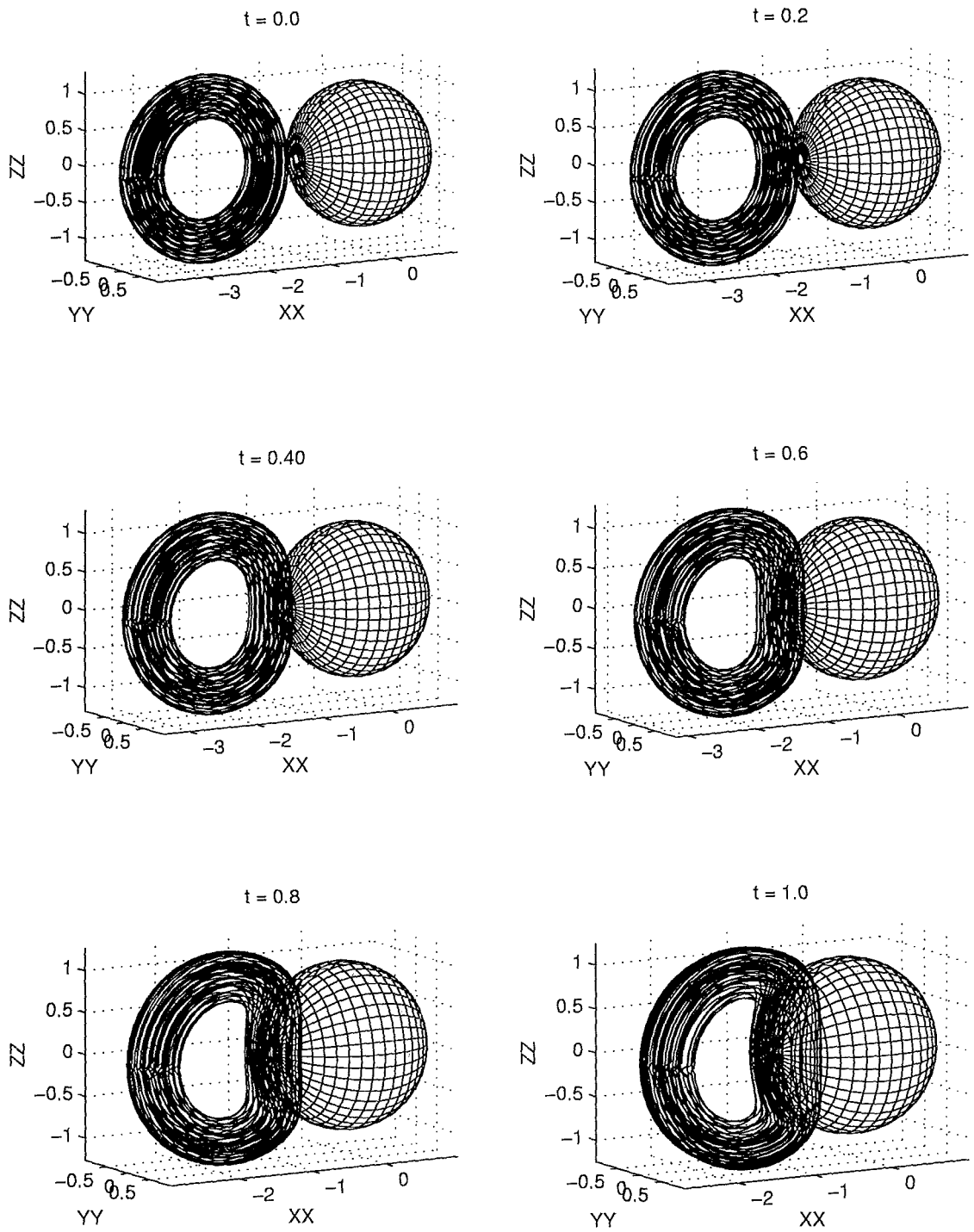


Figure 4.33: Trajectory of the vortex particles during the normal interaction between a vortex ring and a sphere

the ring vortex and the radius of the cross section is 0.1. Throughout the calculation, the core radius of vortex particles is 0.035. The surface of the blade is discretised into 1250 panels and each panel is further divided into 6×6 subpanels. The center of the vortex ring is initially located at a distance of $X_v = -0.75$ upstream of the blade leading edge. Since the ring also moves in the y -direction due to its self-induced velocity, an initial spanwise offset of the ring is introduced such that the vortex will collide with the blade close to the blade center ($y = 0$). The time step employed for advancing the solution is 0.005. Four cases have been calculated for values of the vortex circulation Γ of 0.2, 0.5, 0.75, 1.0. In figure 4.30, six snapshots of sideview of the vortex passage during the interaction are shown for the case of $\Gamma = 1.0$. As the vortex approaches the leading edge of the blade, because of the interference of the blade, part of the vortex ring which is close to the blade begins to deform and compress. Then, as the leading edge of the blade penetrates into the vortex core, the vortex ring splits into two parts and a substantial compression of the nearby vorticity field is clearly visible from the density of the vortex particles. After this stage, however, the solution begins to diverge and the calculation is terminated. There are several reasons which may be attributed to this situation. Firstly, the penetration of the blade into the vortex core and the subsequent splitting of the vortex ring are viscous processes, in which vorticity interchange between the boundary layer and the vortex ring occurs. In fact, according to the inviscid theory, a vortex line will only be stretched under the influence of a body and will never be cut by a blade. However, in the present study, neither the viscous effect nor the boundary layer around the wing surface is properly modelled due to the difficulties in existing standard 3-D vortex particle methods. Secondly, the overlapping condition of vortex particles is hard to maintain in the calculation due to the deformation and the splitting of the vortex ring during a close interaction, which manifests a need to add new particles during the calculation once the distances between neighbouring vortex particles become

large enough. Figure 4.28 gives the predicted suction forces on the blade due to the approaching vortex ring for all the cases, which compares well with the results from the rapid deformation theory and the vorticity collocation method[72]. The coefficients of the suction force shown in this picture are nondimensionalized by the square of the strength of the vortex ring, so it can be concluded that before the vortex ring touches the leading edge of the blade, the suction force is proportional to square of the strength of the vortex ring and is also in compliance with the RDT theory.

In the second case, the problem of vortex ring-sphere interaction is simulated. In this calculation, both the radii of the vortex ring and the sphere are 1.0 and the Gaussian distribution of the vorticity is assumed within the cross-section of the vortex ring with a radius of 0.1. The vortex ring is modelled by 3272 vortex particles of core radius of 0.064 and the sphere is represented by 861 surface panels. The nondimensional time step used for calculation is 0.01. Figure 4.33 illustrates several snapshots of the filament representation of the vortex ring during the interaction. The difference between the vortex ring-sphere interaction and the previous case is that in the present case, the vortex ring is never cut by the sphere, instead the vortex ring is firstly flattened as it approaches the leading edge of the sphere, then it wraps around the forward part of the sphere. This result is consistent with previous theoretical and experimental results conducted by Marshall et al[71], in which it was found that as the vortex interacts with a thick body, the vortex filaments will not be cut through by the body. Shown in figure 4.31 and 4.32 are integrated suction force and side force exerted on the sphere during the normal vortex-body interaction.

Chapter 5

Fast summation algorithm

5.1 Basic idea

The basic idea behind fast algorithms based on the N-body tree codes is as follows.

Suppose that we need to compute the sums

$$S(\mathbf{x}_i) = \sum_{j=1, j \neq i}^n w_j f(\mathbf{x}_i, \mathbf{x}_j), i = 1, \dots, n, \quad (5.1)$$

where \mathbf{x}_i are n given points in a domain $\mathfrak{R} \subset \mathbf{R}^d$, $d = 1, 2, 3$, $f : \mathbf{R}^d \times \mathbf{R}^d \rightarrow \mathbf{R}$ is a given function, and $w_j \in \mathbf{R}$ are some coefficients. Usually $f(\mathbf{x}, \mathbf{y})$ is either singular or very large at $\mathbf{x} = \mathbf{y}$ and decaying fast from this point. The computational domain \mathfrak{R} is covered by a hierarchy of meshes of height H . On each mesh cell τ such that $\mathbf{x} \in \tau$, $f(\mathbf{x}, \mathbf{y})$ is approximated by a weighted sum of functions $\phi_{k,\tau}(\mathbf{y})$, achieving a "separation" of variables:

$$f(\mathbf{x}, \mathbf{y}) \simeq \sum_{k=0}^{\lambda(\mathbf{x}, \tau)} F_{k,\tau}(\mathbf{x}) \phi_{k,\tau}(\mathbf{y}), \mathbf{y} \in \tau. \quad (5.2)$$

Several choices are available for this purpose, for example, in the multipole expansion method, Legendre polynomials are used for a singular kernel in the form of $f(\mathbf{x}, \mathbf{y}) = \frac{1}{|\mathbf{x}-\mathbf{y}|}$. This method has been very successful in two dimensional problems including the discrete vortex method and has been thoroughly tested and parallelized. One restriction of the approach, however, is that it can only be used for

the singular kernel and in 3-D, it is complicated in terms of mathematical formulation. Another more general choice to separate the variables is employing a Taylor expansion around the centre \mathbf{y} of τ as used in [33]:

$$f(\mathbf{x}, \mathbf{y}) \simeq \sum_{k=0}^{\lambda(\mathbf{x}, \tau)} F_{k, \tau}(\mathbf{x})(\mathbf{y} - \mathbf{y}_\tau)^k, \mathbf{y} \in \tau. \quad (5.3)$$

One of the advantages of using Taylor expansion is that it can be used not only for singular kernels but also for a general kernel such as the smoothed kernel for calculating both potential and velocity in the context of vortex particle methods. The accuracy of this approximation can be estimated based on convergence of the series and the terms used in the expansion.

The above separation of variables is used as follows: for each \mathbf{x}_i partition \mathfrak{R} into a collection $\mathfrak{S}(\mathbf{x}_i)$ of mesh cells(at different levels in the hierarchy) and write equation 5.1 as

$$S(\mathbf{x}_i) = \sum_{\tau \in \mathfrak{S}(\mathbf{x}_i)} \sum_{\mathbf{x}_j \in \tau} w_j f(\mathbf{x}_i, \mathbf{x}_j) \quad (5.4)$$

The second sum is approximated by

$$\begin{aligned} \sum_{\mathbf{x}_j \in \tau} w_j f(\mathbf{x}_i, \mathbf{x}_j) &\simeq \sum_{\mathbf{x}_j \in \tau} w_j \sum_{k=0}^{\lambda(\mathbf{x}, \tau)} F_{k, \tau}(\mathbf{x}_i) \phi_{k, \tau}(\mathbf{x}_j) \\ &= \sum_{k=0}^{\lambda(\mathbf{x}, \tau)} F_{k, \tau}(\mathbf{x}_i) \sum_{\mathbf{x}_j \in \tau} w_j \phi_{k, \tau}(\mathbf{x}_j) \\ &= \sum_{k=0}^{\lambda(\mathbf{x}, \tau)} F_{k, \tau}(\mathbf{x}_i) c_{k, \tau} \end{aligned}$$

for some functions $F_{k, \tau}$ and coefficients $c_{k, \tau}$ which do not depend on \mathbf{x}_i . The reduction in the complexity for the evaluation of sums (equation 5.1) for $i = 1, \dots, n$ is achieved by precomputing $c_{k, \tau}$ for all k and all possible cells τ and thus the point-point(pairwise) interaction problem has been transformed into point-group of points interaction problem. Detailed discussions on the complexity of fast algorithms based

on the complete treecode were provided in [38][32][33] and generally, these kind of algorithms have a computational cost proportional to $O(N \log N)$ or $O(N)$ rather than $O(N^2)$.

A 2-D example of the fast algorithm based on Taylor expansion was given in [33]. This chapter is mainly concerned with 3-D cases, in which the method has been extended to approximate the velocity calculation in the 3-D vortex particle method.

As shown before, the smooth kernel for evaluating velocity field $\mathbf{U}_\sigma(\mathbf{x}, t)$ by using the high order smoothing function (equation 3.44) has the form

$$K_\sigma(\mathbf{x}, \mathbf{y}) = \frac{|\mathbf{x} - \mathbf{y}|^2 + 2.5\sigma^2}{(|\mathbf{x} - \mathbf{y}|^2 + \sigma^2)^{5/2}} (\mathbf{x} - \mathbf{y}) \quad (5.5)$$

The purpose of introducing the core size σ is to avoid the infinite self-induced velocity in the singular kernel. As the value of $K|\mathbf{x} - \mathbf{y}|$ becomes large, the smooth kernel will be equivalent to the singular kernel

$$(\mathbf{x}, \mathbf{y}) = \frac{\mathbf{x} - \mathbf{y}}{|\mathbf{x} - \mathbf{y}|^3} \quad (5.6)$$

Furthermore, as will be shown later, only the effect of vortices separated relatively large distances will be approximated by the fast (indirect) method, where the singular kernel is eligible, whereas the effect of the vortex points in the neighbourhood of a point is summarised using the direct method (smooth kernel). Therefore, to avoid the unnecessary complexity of mathematical formulation without losing generality of the method, only the singular kernel is considered in the following fast summation algorithm.

5.2 Taylor expansion

Fix point \mathbf{x} and $\tau \in \mathfrak{S}(\mathbf{x})$, the kernel (equation 34), $\mathbf{y} \in \tau$ will be approximated by its Taylor polynomial of degree $\lambda - 1$. The 3-D Taylor expansion of degree $\lambda - 1$ of

$f(\mathbf{x}, \mathbf{y}) = \frac{\mathbf{x}-\mathbf{y}}{|\mathbf{x}-\mathbf{y}|^3}$ with respect to \mathbf{y} about \mathbf{y}_τ is

$$f(\mathbf{x}, \mathbf{y}) = P_{\lambda-1}(\mathbf{x}, \mathbf{y}, \mathbf{y}_\tau) + R_{\lambda-1}(\mathbf{x}, \mathbf{y}, \mathbf{y}_\tau) \quad (5.7)$$

where

$$P_{\lambda-1}(\mathbf{x}, \mathbf{y}, \mathbf{y}_\tau) = \sum_{|k| \leq \lambda-1} \frac{1}{k!} D_{\mathbf{y}}^k f(\mathbf{x}, \mathbf{y})_{\mathbf{y}=\mathbf{y}_\tau} (\mathbf{y} - \mathbf{y}_\tau)^k \quad (5.8)$$

$$= \sum_{|k| \leq \lambda-1} a_k(\mathbf{x}, \mathbf{y}_\tau) (\mathbf{y} - \mathbf{y}_\tau)^k \quad (5.9)$$

and $k = (k_1, k_2, k_3)$, $|k| = k_1 + k_2 + k_3$, $k! = k_1!k_2!k_3!$, $D_{\mathbf{y}}^k = \partial^{k_1}/\partial y_1^{k_1} \partial y_2^{k_2} \partial y_3^{k_3}$, $\mathbf{y}^k = y_1^{k_1} y_2^{k_2} y_3^{k_3}$.

The coefficients $a_k(\mathbf{x}, \mathbf{y}_\tau) = \frac{1}{k!} D_{\mathbf{y}}^k f(\mathbf{x}, \mathbf{y})_{\mathbf{y}=\mathbf{y}_\tau}$ can be calculated using the recurrence given in Appendix A, which is crucial for an efficient implementation of the algorithm. From the recurrence, it can be shown that the remainder $|R_{\lambda-1}|$ has the order $O(\frac{|\mathbf{y}-\mathbf{y}_\tau|^\lambda}{|\mathbf{x}-\mathbf{y}|^{\lambda+3}})$ and the relative error $|R_{\lambda-1}|/f(\mathbf{x} - \mathbf{y}_\tau)$ has the order $O(\frac{|\mathbf{y}-\mathbf{y}_\tau|^\lambda}{|\mathbf{x}-\mathbf{y}_\tau|^\lambda})$, or $O((\frac{\rho}{d})^\lambda)$, where the ρ is the radius of box τ with the definition $\rho(\tau) = \sup\{|\mathbf{y} - \mathbf{y}_\tau| : \mathbf{y} \in \tau\}$ and d the distance from point \mathbf{x} to the centre \mathbf{y}_τ of the box. Thus, if $d \geq M\rho$, $(\frac{\rho}{d})^\lambda \rightarrow 0$ as $\lambda \rightarrow \infty$, where M is a given constant larger than one. So for a given small number ϵ , we can choose λ to be the smallest positive integer such that the relative error $|R_{\lambda-1}|/f(\mathbf{x} - \mathbf{y}_\tau) \sim \epsilon$.

Let $k^{\lambda, \tau}(\mathbf{x}, \mathbf{y}) = P_{\lambda-1}(\mathbf{x}, \mathbf{y}, \mathbf{y}_\tau)$, then the calculation of the velocity $\mathbf{u}_\sigma(\mathbf{x}, t)$ at point \mathbf{x} (time t will be fixed and omitted) can be divided into the following two parts:

$$\tilde{\mathbf{u}}(\mathbf{x}) = \sum_{\tau \in \mathfrak{S}(\mathbf{x})} \tilde{\mathbf{u}}^\tau(\mathbf{x}) + \tilde{\mathbf{u}}'(\mathbf{x}) \quad (5.10)$$

where $\mathfrak{S}(\mathbf{x})$ is a set consisting of hierarchical boxes which are eligible for the indirect summation (far field) and will be defined later and the second term represents the effects from those boxes which are either too close to the point \mathbf{x} (near field) or contain too few particles.

The expression for $\tilde{u}^\tau(X)$ is given by

$$\begin{aligned}
\tilde{u}^\tau(\mathbf{x}) &= -\frac{1}{4\pi} \sum_{\mathbf{y}_j \in \tau} K^{\lambda, \tau}(\mathbf{x}, \mathbf{y}_j) (\mathbf{x} - \mathbf{y}_j) \times \alpha_j \\
&= -\frac{1}{4\pi} \sum_{\mathbf{y}_j \in \tau} [(x_2 - y_{j2})\alpha_{j3} - (x_3 - y_{j3})\alpha_{j2}, \\
&\quad (x_3 - y_{j3})\alpha_{j1} - (x_1 - y_{j1})\alpha_{j3}, \\
&\quad (x_1 - y_{j1})\alpha_{j2} - (x_2 - y_{j2})\alpha_{j1}] \sum_{|k| \leq \lambda-1} a_k(\mathbf{x}, \mathbf{y}_\tau) (\mathbf{y}_j - \mathbf{y}_\tau^k) \\
&= -\frac{1}{4\pi} \sum_{|k| \leq \lambda-1} a_k(\mathbf{x}, \mathbf{y}_\tau) [(x_2 A_\tau^k - B_\tau^k - x_3 C_\tau^k + D_\tau^k), \\
&\quad (x_3 E_\tau^k - F_\tau^k - x_1 A_\tau^k + G_\tau^k), (x_1 C_\tau^k - H_\tau^k - x_2 E_\tau^k + I_\tau^k)].
\end{aligned}$$

and

$$\begin{aligned}
A_\tau^k &= \sum_{\mathbf{y}_j \in \tau} \alpha_{j3} (\mathbf{y}_j - \mathbf{y}_\tau)^k, B_\tau^k = \sum_{\mathbf{y}_j \in \tau} y_{j2} \alpha_{j3} (\mathbf{y}_j - \mathbf{y}_\tau)^k, \\
C_\tau^k &= \sum_{\mathbf{y}_j \in \tau} \alpha_{j2} (\mathbf{y}_j - \mathbf{y}_\tau)^k, D_\tau^k = \sum_{\mathbf{y}_j \in \tau} y_{j3} \alpha_{j2} (\mathbf{y}_j - \mathbf{y}_\tau)^k, \\
E_\tau^k &= \sum_{\mathbf{y}_j \in \tau} \alpha_{j1} (\mathbf{y}_j - \mathbf{y}_\tau)^k, F_\tau^k = \sum_{\mathbf{y}_j \in \tau} y_{j3} \alpha_{j1} (\mathbf{y}_j - \mathbf{y}_\tau)^k, \\
G_\tau^k &= \sum_{\mathbf{y}_j \in \tau} y_{j1} \alpha_{j3} (\mathbf{y}_j - \mathbf{y}_\tau)^k, H_\tau^k = \sum_{\mathbf{y}_j \in \tau} y_{j1} \alpha_{j2} (\mathbf{y}_j - \mathbf{y}_\tau)^k, \\
I_\tau^k &= \sum_{\mathbf{y}_j \in \tau} y_{j2} \alpha_{j1} (\mathbf{y}_j - \mathbf{y}_\tau)^k.
\end{aligned}$$

The sums in above equations are evaluated for all boxes τ and indices k before the velocity calculation is performed and in parallel with the vortex sorting and grid generation process which will be described in the next section. These results are stored as they are needed for velocity calculation.

In 3-D applications, because of the existence of the stretching term in the vorticity transport equation, the derivative of the velocity is also required. This can be obtained from the derivative of the right-hand term in the equation for calculating

$\tilde{\mathbf{u}}^\tau(\mathbf{x})$. For example

$$\begin{aligned} \frac{\partial \tilde{\mathbf{u}}^\tau(\mathbf{x})}{\partial x_1} = & -\frac{1}{4\pi} \sum_{|k| \leq \lambda-1} \left\{ \frac{\partial a_k(\mathbf{x}, \mathbf{y}_\tau)}{\partial x_1} [(x_2 A_\tau^k - B_\tau^k - x_3 C_\tau^k + D_\tau^k), \right. \\ & (x_3 E_\tau^k - F_\tau^k - x_1 A_\tau^k + G_\tau^k), (x_1 C_\tau^k - H_\tau^k - x_2 E_\tau^k + I_\tau^k)] \\ & \left. + a_k(\mathbf{x}, \mathbf{y}_\tau) [0, -A_\tau^k, C_\tau^k] \right\} \end{aligned}$$

where the calculation of $\frac{\partial a_{k_1, k_2, k_3}}{\partial x_i}$, $i = 1, 2, 3$ can be simplified by virtue of the symmetry of the function $f(\mathbf{x}, \mathbf{y}) = \frac{1}{|\mathbf{x}-\mathbf{y}|^3}$, i.e. $f(\mathbf{x}, \mathbf{y}) = f(\mathbf{y}, \mathbf{x})$ and $\frac{\partial^n f}{\partial \mathbf{x}^n} = -\frac{\partial^n f}{\partial \mathbf{y}^n}$, which yields, for example:

$$\frac{\partial a_{k_1, k_2, k_3}}{\partial x_1} = -(k_1 + 1) a_{k_1+1, k_2, k_3} \quad (5.11)$$

5.3 Mesh structure and sorting of vortices

One of the key issues in using the fast algorithm effectively is that the vortices must be spatially grouped together. One way in doing this is to employ a hierarchical grid system based on the complete binary tree code as shown in figure 5.1 for a 2-D problem. For 3-D, another direction should be added in figure 5.1. The root of the tree is the smallest box that encloses all vortex particles in the flow field. Then each node of the tree is divided into two equal sub-boxes by cutting the longest side of the box. This process continues until the top of the tree has been reached (the height of the tree is given either a priori or calculated by some other means). The relationship between the parent and children nodes can be easily constructed by using the following numbering system:

$$parent(i) = integer(i/2) \quad (5.12)$$

and

$$child(i) = 2i + k, k = 1, 2. \quad (5.13)$$

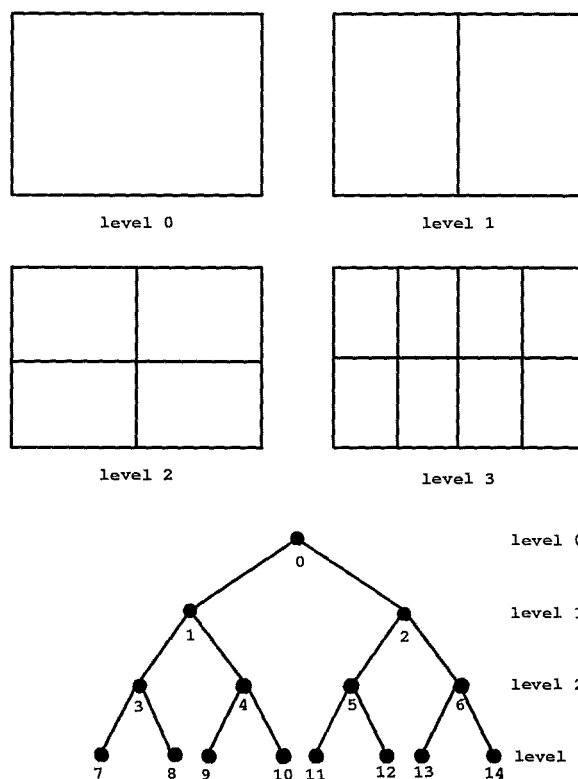


Figure 5.1: Illustration of a complete three-level binary tree in the context of vortex sorting

This tree code is very effective for uniform distribution of vortex particles, but it is not recommended for a highly non-uniform distribution, which is usually the case for most applications, where many of the boxes may be empty or only contain a small number of vortices. An alternative is to employ an adaptive grid system based on the incomplete treecode, in which a decision is made during the grid generation process whether a box should be further divided, based on the number of vortex particles it contains. The structure of this tree code is illustrated in figure 5.2: the boxes with no vortex or only a small number of vortices have been excluded from the tree. Now, the numbering system for the boxes has a more complex form, as shown in figure 5.2: the box numbering remains continuous and increases during the division process; once a box is divided into two sub-boxes, the total number of the boxes will be increased by two. In such a numbering system, the number of a box is always bigger than that of its parent box and boxes at the same level as its

parent box. The order of the two children boxes is determined by the coordinates of their centers, the larger the coordinate in the direction of the longest side of their parent box, the bigger the number of the box. A pointer is also needed for each box to record the numbers of its parent box and its children boxes respectively. The two children boxes of a box are distinguished by the first child box(left leaf) and the second child box(right leaf).

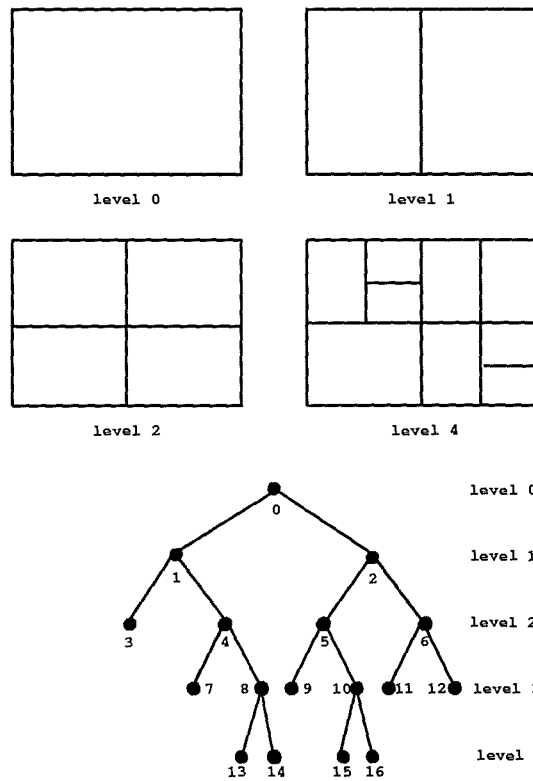


Figure 5.2: Illustration of an incomplete four-level binary tree in the context of vortex sorting

The sorting process, in which the vortices are allocated to each box is accomplished at the same time as the grids are generated. To reduce the memory requirement for sorting vortices, the vortices are reordered so as to group the vortices in each of the two sub-boxes together. Thus, the vortices in a box can be identified by the first and last vortex within the box in the entire vortex list which records the locations and strengths of all the vortices in the flow field.

The logic chart based on the adaptive grid generation and vortex sorting is shown

in figure 5.3 . The process starts with the first box which covers the entire collection of vortices and continues until the last box in the tree is encountered.

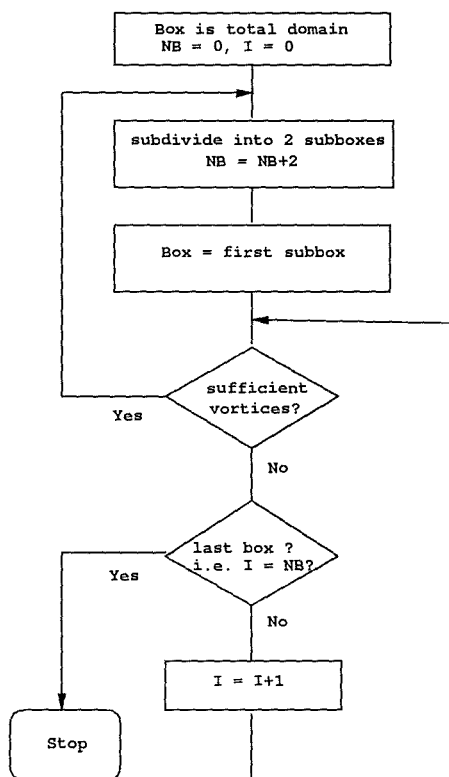


Figure 5.3: Logic flow chart for adaptive grid generation and vortex sorting

5.4 Velocity calculations

Once the sorting and grid generation process, which includes calculation of the sums for each box(preprocessing) is accomplished, the calculation of the velocity at a point x in the flow field can be simply achieved in a single pass over all boxes but in a different order in which they were generated. For a specific point, only part of the boxes in the entire tree will be used for its velocity calculation. The procedure is outlined in figure 5.4, which starts from the first box which contains all particles in the flow domain. Only the boxes with enough vortex particles will be considered for indirect summation. The minimum number of particles in a box for indirect summation, which is an indicator of when the indirect summation starts becoming

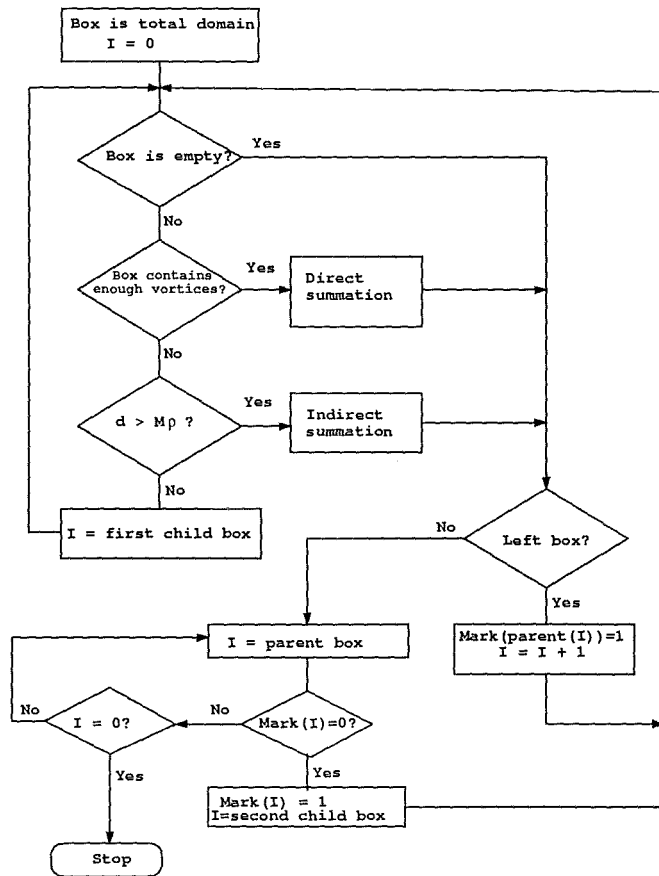


Figure 5.4: Logic flow chart for calculating velocity using the fast summation algorithm

faster than the direct summation due to the overheads introduced in calculating the coefficients of Taylor series and the preprocessing for each box, can be determined and optimized by numerical experiments. The other criterion to determine whether a box will be used for fast summation is the relative distance between the point and the centre of the box d/ρ as required by the convergence of the Taylor series and accuracy of the approximation. If $d/\rho \geq M$, then the box will be used for fast summation, otherwise, the first child of the box will be checked. In the following calculation, $M = 2$ is adopted, which ensures the convergence rate of the Taylor series is proportional to $(\frac{1}{2})^{\lambda+1}$. In figure 5.4, the value of the array $mark(I)$ is used to change the route for checking if a box is eligible for indirect summation, which is initially set to be zero for all the boxes. When the two children of box i have been

checked, the value of $mark(I)$ becomes unity. The process of velocity calculation also starts from the first box which covers all the particles in the flow domain and continues until the $mark(I)$ values for all parent boxes of a right box are units.

5.5 Performance of the algorithm

5.5.1 Accuracy of the algorithm

To verify that the program is running correctly and to test the accuracy of the fast summation algorithm, the self-induced velocity at the centre of a vortex ring of Gaussian distribution of vorticity within the cross section has been calculated using the fast algorithm. The vortex ring is represented by vortex particles. To discretise the core of the vortex ring, a mesh system is constructed using N_ϕ cross sections of torus separated by an angle $\Delta\phi = 2\pi/N_\phi$ and N_s cells within each cross section, see figure 3.2. The elements within each cross section of the ring are arranged on n_c radial locations and each cell has an equal area πr_l^2 . The center of each vortex element is located at its centroid x_i and the initial strength vector of the vortex element is set equal to $\omega(x_i, 0)dv_i$, where dv_i is the volume of each vortex element.

The results for a number of λ values have been given in table 5.1, which shows that by increasing the λ value, the results from the fast algorithm approach gradually the 'exact value' calculated from the direct summation method.

In figure 5.5 and 5.6, the results from a long time(400 timesteps) calculation of the interaction of two vortex rings are presented for direct summation and fast algorithm($\lambda = 7$) respectively. The nearly identical results show that for most applications, high accuracy can be achieved using the fast summation without employing too many terms in the Taylor series.

λ	U_c	CPU(seconds)
1	-0.4881384	0.92
2	-0.4971417	2.68
3	-0.4978105	5.25
4	-0.4979530	9.05
5	-0.4979540	15.70
6	-0.4979719	25.17
7	-0.4979776	38.74
8	-0.4979798	60.15
9	-0.4979801	83.02
10	-0.4979804	115.48
'exact'	-0.4979874	0.54

Table 5.1: Convergence study of the fast algorithm in terms of the order of Taylor expansion λ

λ	1	2	3	4	5	6	7	8	9	10
CPU(seconds)	158.	163.	171.	177.	196.	213.	241.	270.	318.	382.

Table 5.2: Effect of λ value on timing of the fast algorithm

5.5.2 Timing of the fast algorithm

In this section, the timing of the fast algorithm is examined by calculating the interaction of two vortex rings as described in the previous section. In these calculations, the timing results for only one time step are used for comparison. Firstly, in table 5.2, the effect of λ value on the used CPU time are given, from which it can be seen that as the value of λ increases, a substantial rise in the CPU time occurs due to the rapid increase in the terms used in Taylor expansion. A strategy based on this fact can be used during the early stage of code development and test to reduce time consumption: i.e. using lower order of Taylor expansion (small λ). However, as a compromise between the accuracy and efficiency, in the following calculations, the value of λ is set at 7.

The criterion for box subdivision, i.e. the number of vortices in a box, which eventually determines the total number of boxes in the incomplete tree code, also has some effects on the timing result. The optimum value for the case tested is

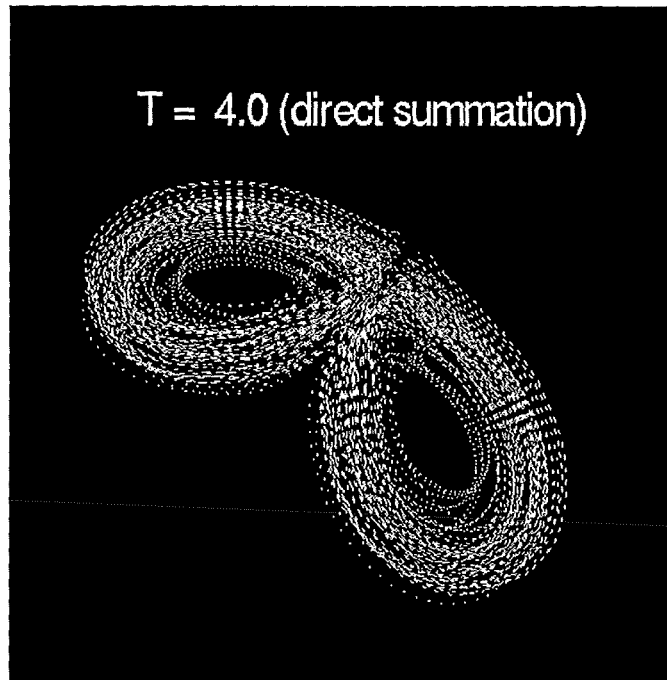


Figure 5.5: Vortex particle distribution at $T = 4.0$ from the direct summation method for the two vortex ring interaction problem

around 350-500 depending on the total number of vortices.

In figure 5.7, the timing results vs number of particles are shown for both direct summation and fast algorithm, which gives a breakeven point around 5000-6000. As the number of vortex particles is increased to about 62720, the speed-up ratio for the fast summation method is around 5.

5.5.3 High resolution calculation of twin vortex ring interaction

In this section, the interaction and fusion of two vortex rings has been studied by using a large number of vortex particles. This problem is of both fundamental and numerical interest in the field of fluid dynamics. The two vortex rings are represented by 13,222 vortex particles ($81 \times 81 \times 2$), and the initial conditions of the vortex rings are the same as those given in [120]. Figure 5.8 gives 8 snapshots of the interaction and fusion process of the twin vortex ring, which show that better results have been obtained by using higher resolution of vortex particles in terms of the reconnection

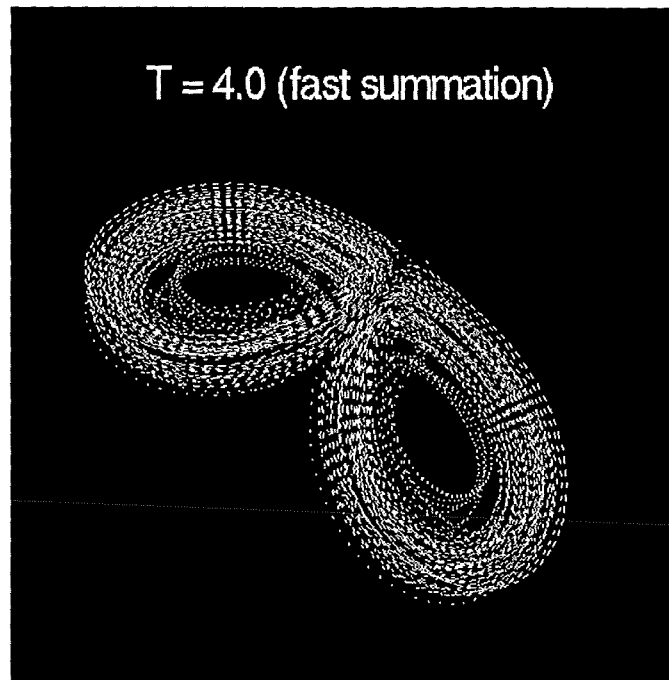


Figure 5.6: Vortex particle distribution at $T = 4.0$ from the fast summation method for the two vortex ring interaction problem

of the vortex rings.

5.6 Conclusions

A 3-D version of the fast summation algorithm based on the general Taylor expansions has been developed for the vortex particle method. High efficiency of the code is achieved by employing the incomplete tree-code for vortex sorting and velocity calculations. The adaptivity of the code reduces memory requirement, which is essential for the method to be applied to a large number of vortex particles.

The performance of the fast summation is tested by calculating the interaction of two vortex rings. The results show that the present method provides a simpler alternative to the fast multipole method and has the potential to be applied to practical flow problems.

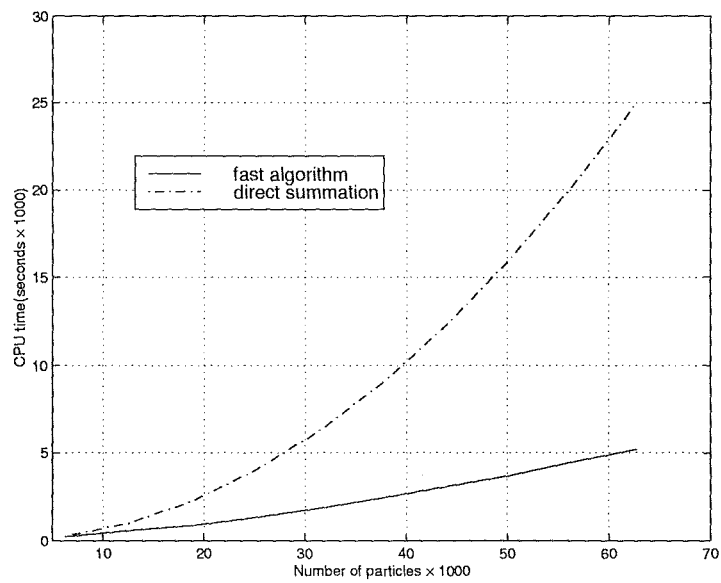


Figure 5.7: Comparison of CPU timing between the fast algorithm and the direct summation method for the two vortex ring interaction problem

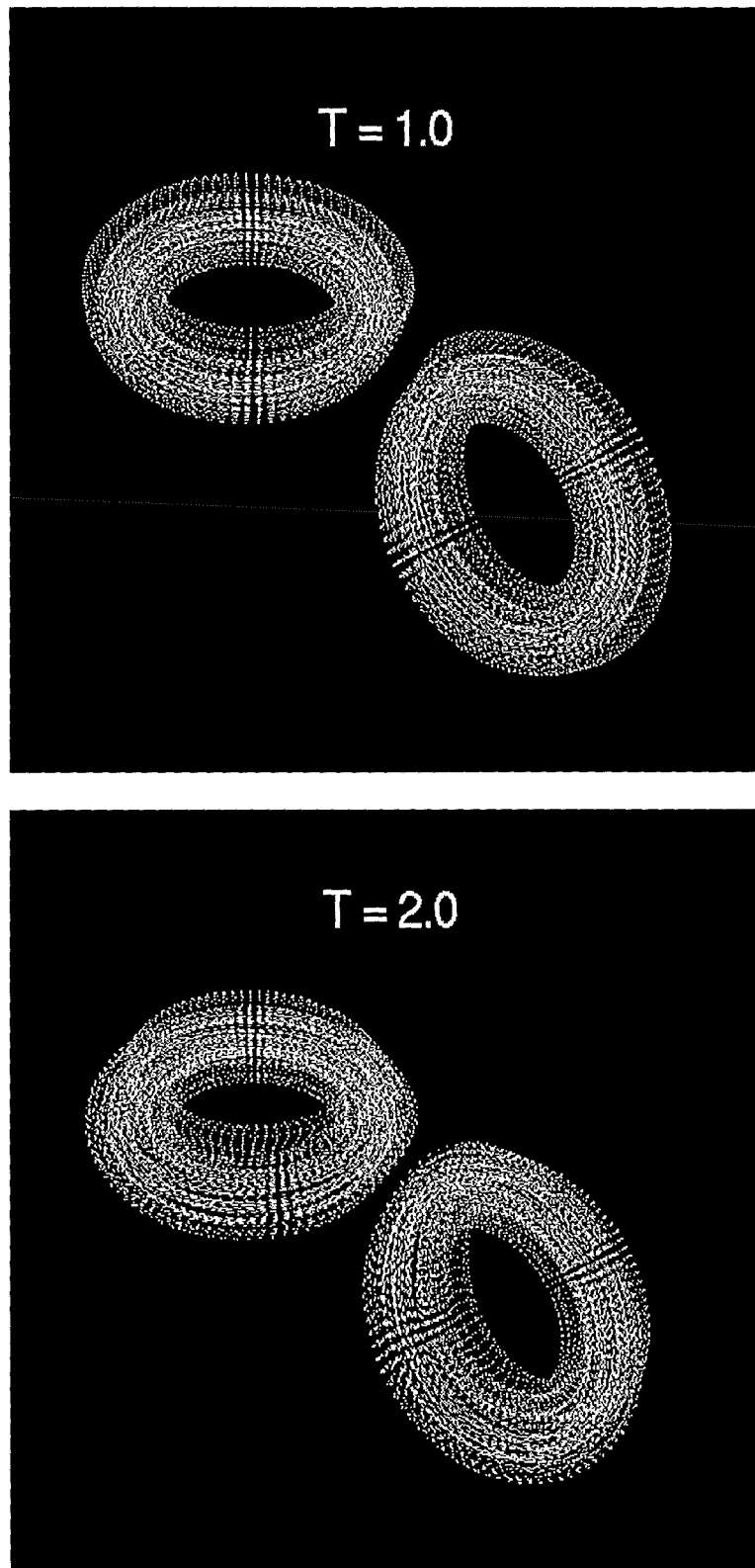


Figure 5.8: Results for the interaction and fusion of two vortex rings using the fast summation algorithm

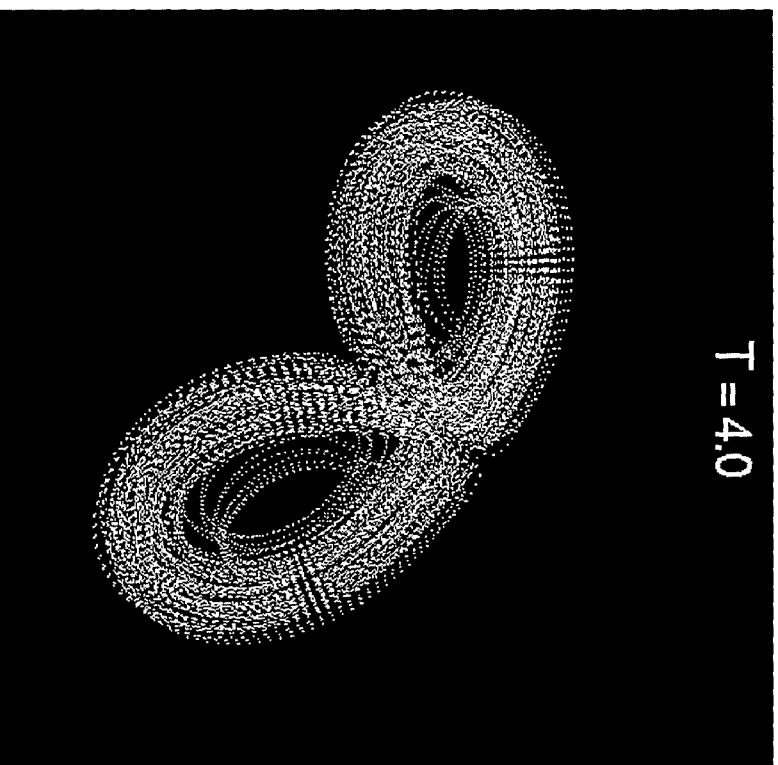
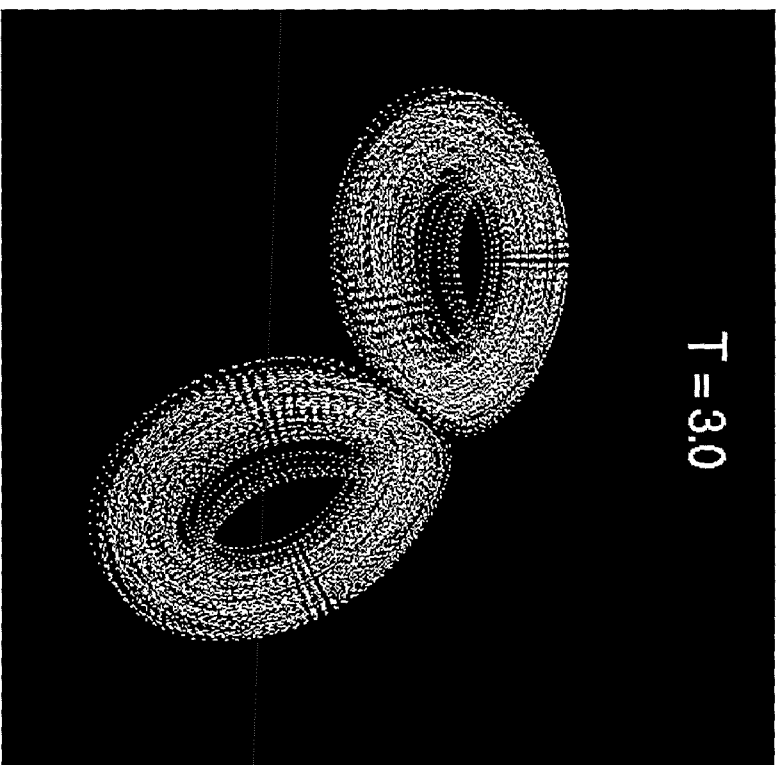


Figure 5.8: Continued

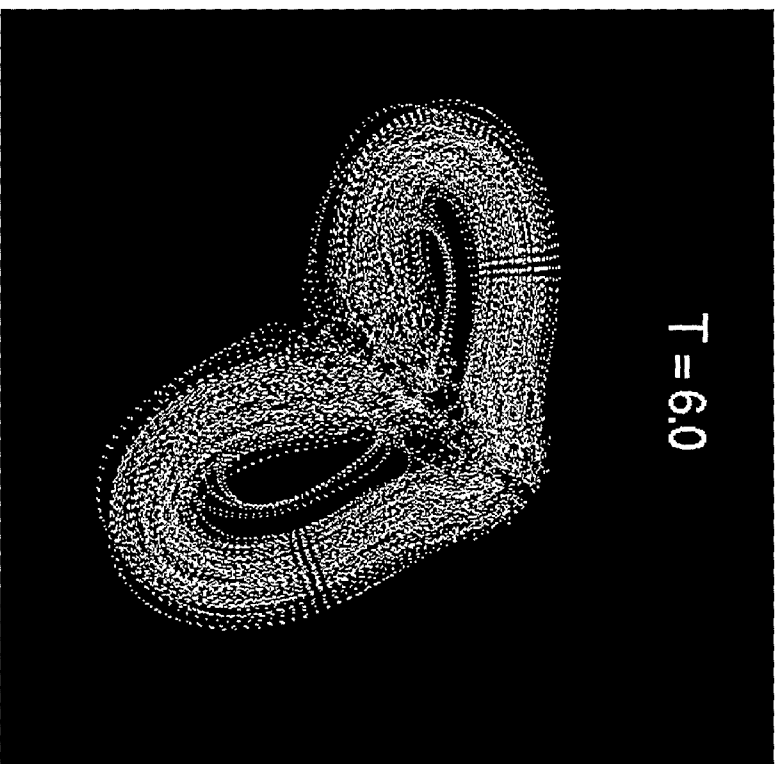
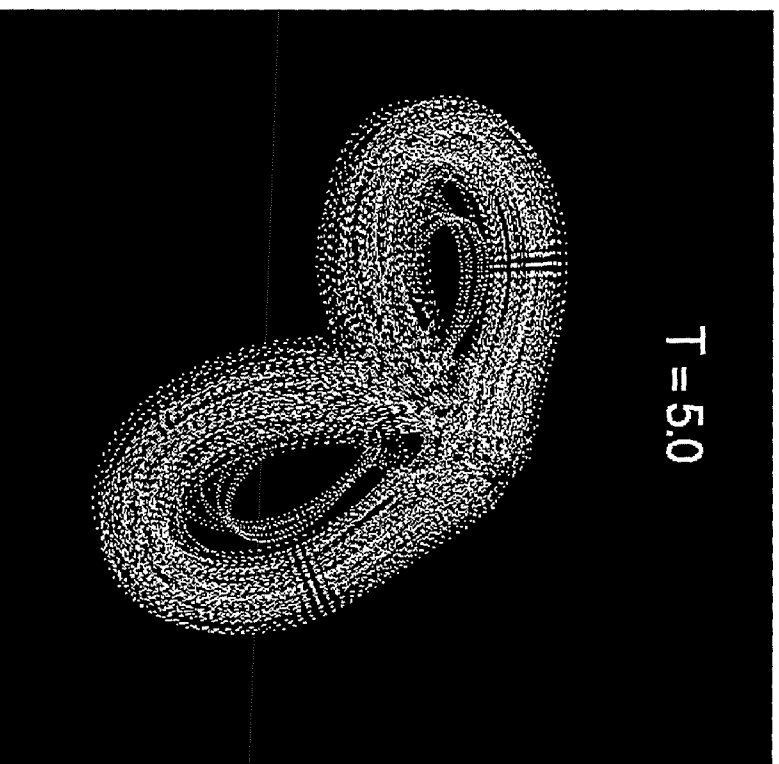


Figure 5.8: Continued

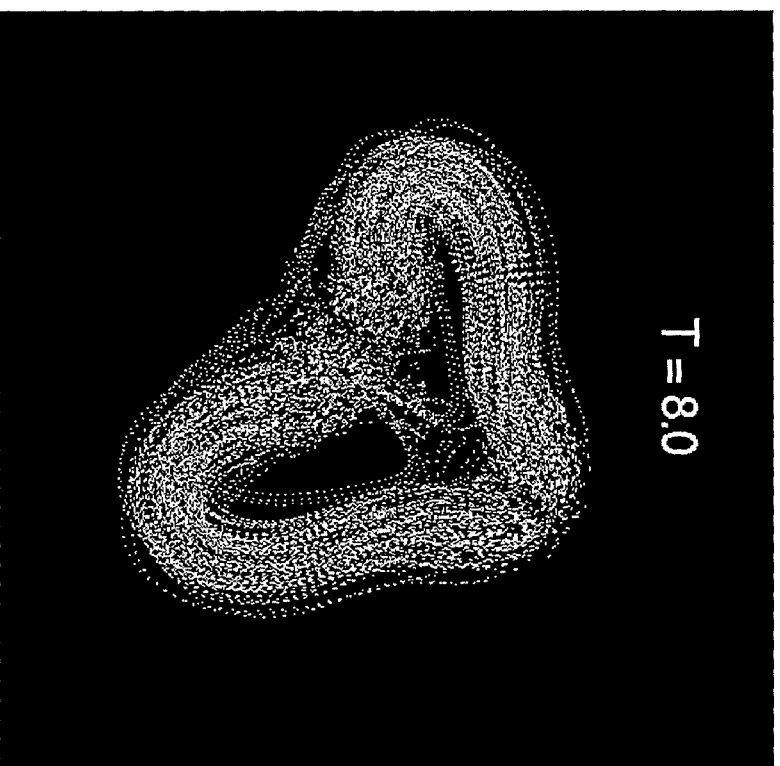
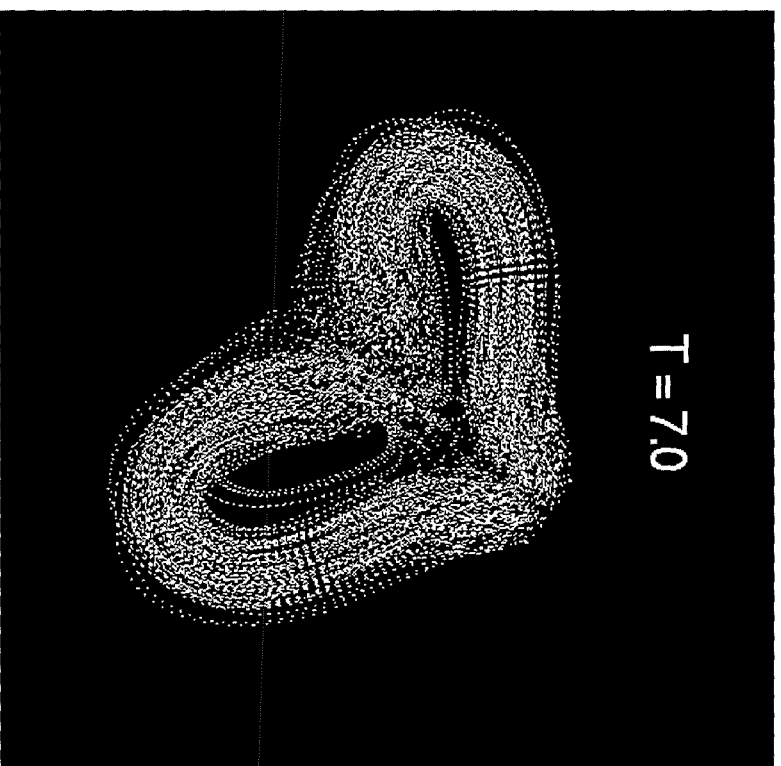


Figure 5.8: Continued

Chapter 6

Implementation of the New Hybrid Vorticity-based Method

6.1 Basic idea of the method

The main purpose of developing the new vorticity-based method is to overcome some difficulties in the discrete vortex method as outlined in Chapter 1. The basic idea of the method, including governing equations and solution procedure, is the same as the discrete vortex method except that in the new method, a grid system is reintroduced and the vorticity transport equation is solved by using the cell-centred finite volume method. In the present study, the formulation and results are presented for 2-D cases only.

6.2 Solution of vorticity transport equation

The solution of the vorticity transport equation using the cell-centred finite volume method is straightforward. For each control volume Ω_c , see figure (6.1), the vorticity transport equation can be written in the integral form:

$$\frac{\partial}{\partial t} \int_{\Omega_c} \omega d\Omega + \int_s \mathbf{u}\omega \cdot \mathbf{n} ds = \nu \int_s \nabla\omega \cdot \mathbf{n} ds \quad (6.1)$$

where \mathbf{n} is the unit normal vector of the control volume surface s .

By using the second-order Adams-Bashforth scheme, equation (6.1) can be advanced in time to obtain the new values of vorticity for cell (i,j) as shown in figure

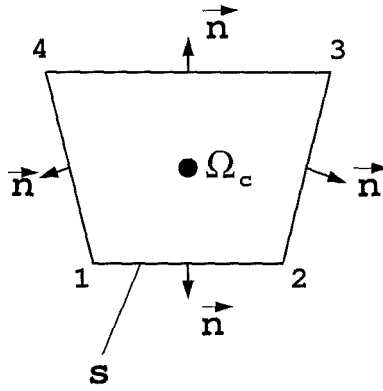


Figure 6.1: Definition sketch of a control volume in the hybrid vortex method

(6.2):

$$(\omega V)_{i,j}^{n+1} = (\omega V)_{i,j}^n + \frac{\Delta}{2} [3H_{i,j}(t_n, \omega^n, \mathbf{u}^n) - H_{i,j}(t_{n-1}, \omega^{n-1}, \mathbf{u}^{n-1})] \quad (6.2)$$

where V is the area of cell (i,j) and $H_{i,j} = -\int_s (\mathbf{u}\omega - \nu \nabla \omega) \cdot \mathbf{n} ds$. For quadrilateral cell (i,j) , H is a summation of the convective and viscous fluxes through its four sides, i.e. $H_{i,j} = (H_{i,j})_e + (H_{i,j})_s + (H_{i,j})_w + (H_{i,j})_n$.

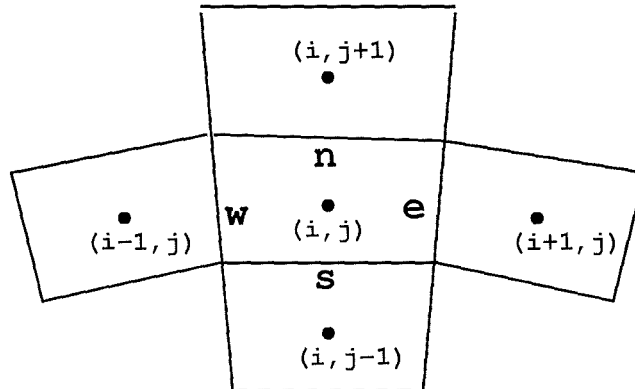


Figure 6.2: Illustration for a control volume and its four neighbouring cells in the context of calculating convective and viscous fluxes

By assuming a linear distribution of flow variables between two neighbouring cells, the gradients of the flow variables across the boundary of the two cells can be easily calculated. For example, for the east side of cell (i,j) , we have

$$(\nabla\omega)_e = \frac{\omega_{i+1,j} - \omega_{i,j}}{x_{i+1,j} - x_{i,j}} \mathbf{i} + \frac{\omega_{i+1,j} - \omega_{i,j}}{y_{i+1,j} - y_{i,j}} \mathbf{j} \quad (6.3)$$

$$(\nabla u)_e = \frac{u_{i+1,j} - u_{i,j}}{x_{i+1,j} - x_{i,j}} \mathbf{i} + \frac{u_{i+1,j} - u_{i,j}}{y_{i+1,j} - y_{i,j}} \mathbf{j} \quad (6.4)$$

$$(\nabla v)_e = \frac{v_{i+1,j} - v_{i,j}}{x_{i+1,j} - x_{i,j}} \mathbf{i} + \frac{v_{i+1,j} - v_{i,j}}{y_{i+1,j} - y_{i,j}} \mathbf{j} \quad (6.5)$$

The values of flow variables at the middle point of side e can then be interpolated from the values at the cell centre:

$$\mathbf{u}_e = \mathbf{u}_{i,j} + \nabla \mathbf{u} \cdot \mathbf{r}_e \quad (6.6)$$

$$\omega_e = \omega_{i,j} + \nabla \omega \cdot \mathbf{r}_e \quad (6.7)$$

where \mathbf{r}_e is the vector from the cell centre to the middle point of the side e. Thus, the flux across the east side of the cell can be calculated:

$$(H_{i,j}) = [(-\mathbf{u}\omega + \nu \nabla \omega) \cdot \mathbf{n}]_e l_e \quad (6.8)$$

and similar results can be obtained for the remaining sides of the control volume.

Since the vorticity transport equation, which redistributes the vorticity within the fluid domain, is solved in the conservative form by using the finite volume approach, no vorticity will be generated in this process by numerical errors and the only concern of vorticity conservation will lie entirely on the process of vorticity generation at the solid boundaries, which will be discussed later.

6.3 Velocity calculation

Once the vorticity distribution in the flow is known, the velocities needed at the centers of the control volumes with non-zero vorticity and some neighbouring control volumes with zero vorticity can be calculated by using the Biot-Savart law described in Chapter 2. By assuming the vorticity has a uniform distribution within each control volume, which is consistent with the cell-centred finite volume approach, the velocity at a point \mathbf{x}_j , in particular at the centre of each control volume, is given by

$$\mathbf{u}_j(\mathbf{x}_j, t) = \frac{1}{2\pi} \sum_{i=1}^{N_v} \int_{\Omega_i} \frac{\omega_i(t) \mathbf{k} \times (\mathbf{x}_j - \mathbf{x}')}{|\mathbf{x}_j - \mathbf{x}'|^2} d\Omega_i + \mathbf{u}_\infty \quad (6.9)$$

where N_v is the total number of the control volumes on which the integral is performed.

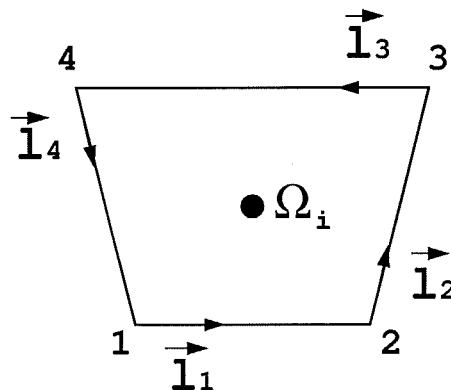


Figure 6.3: Velocity contribution from each control volume using the modified Biot-Savart law

For each control volume Ω_i , by virtue of the following vector identities, $\nabla \times (f\mathbf{G}) = f\nabla \times \mathbf{G} + \nabla f \times \mathbf{G}$ and $\iint \nabla \times \mathbf{G} d\Omega = -\int \mathbf{G} \times \mathbf{n} ds$, the integral in equation (6.9) can be transformed into the circuit integral around the cell, see figure

(6.3),

$$\int_{\Omega_i} \frac{\omega_i(t) \mathbf{k} \times (\mathbf{x}_j - \mathbf{x}')}{|\mathbf{x}_j - \mathbf{x}'|^2} d\Omega_i \quad (6.10)$$

$$= - \int_{\Omega_i} \omega_i(t) \mathbf{k} \times \nabla' \ln |\mathbf{x}_j - \mathbf{x}'| d\Omega_i \quad (6.11)$$

$$= \int_{\Omega_i} \nabla' \times (\omega_i(t) \mathbf{k} \ln |\mathbf{x}_j - \mathbf{x}'|) d\Omega_i \quad (6.12)$$

$$= - \int_{S_i} \omega_i(t) \mathbf{k} \times \mathbf{n} \ln |\mathbf{x}_j - \mathbf{x}'| ds \quad (6.13)$$

$$= -\omega_i(t) \sum_{k=1}^4 \mathbf{l}_k \int_{l_k} \ln |\mathbf{x}_j - \mathbf{x}'| dl_k \quad (6.14)$$

$$= -\omega_i(t) \vec{S}_i \quad (6.15)$$

where \mathbf{l}_k is the unit direction vector of the cell segment l_k and quadrilateral cells have been assumed. To evaluate the integral, either an analytic expression or numerical approximation can be used and for the neighbouring cells, the integral needs to be calculated only once for their common segment.

It is easy to check that in calculating the velocity at a point (cell centre), the influence of all the cells with non-zero vorticity must be taken into account. This involves a calculation of $O(N_v^2)$ interactions for N_v control volumes with non-zero vorticity, which can lead to a large computational cost.

Fortunately, during the last decade, several fast summation algorithms have been developed originally for the discrete vortex method. In this study, the adaptive fast algorithm proposed by Van Dommelen et al [32] has been modified for calculating the velocity field. The basic idea in the method is that when the velocity at the centre, \mathbf{x}_i say, of a control volume Ω_i of area A_{Ω_i} is calculated, the influence of vorticity from the entire flow domain can be divided into the near field, on which the direct summation using equation (6.15) will be performed, and far field, in which a point vortex with strength $\Gamma_i = \omega_i A_{\Omega_i}$ located at \mathbf{x}_i is used temporarily to represent the entire vorticity in the control volume Ω_i and the indirect fast summation method

can be applied:

$$\mathbf{u}(\mathbf{x}_i) = \mathbf{u}'(\mathbf{x}_i)|_{near\ field} + \mathbf{u}^\tau(\mathbf{x}_i)|_{far\ field} \quad (6.16)$$

in which we have

$$\mathbf{u}'(\mathbf{x}_i)|_{near\ field} = \frac{-1}{2\pi} \sum_{j=1}^{N_D} \omega_j(t) \sum_{k=1}^4 \mathbf{l}_k \int_{l_k} \ln |\mathbf{x}_j - \mathbf{x}_i| dl_k \quad (6.17)$$

and

$$\mathbf{u}^\tau(\mathbf{x}_i)|_{far\ field} = \frac{1}{2\pi} \sum_{j=1}^{N_F} \Gamma_j \mathbf{k} \times \frac{\mathbf{x}_i - \mathbf{x}_j}{|\mathbf{x}_i - \mathbf{x}_j|^2} \quad (6.18)$$

where N_D and N_F are the total number of control volumes which are eligible for direct summation and indirect(fast) summation respectively.

By using the complex notation, equation (6.18) can be expressed as

$$u^\tau(Z_i) - iv^\tau(Z_i) = \frac{1}{2\pi i} \sum_{j=1}^{N_F} \frac{1}{Z_i - Z_j} \quad (6.19)$$

where Z is the complex position of \vec{x} and u^τ and v^τ are the two components of \tilde{u}^τ .

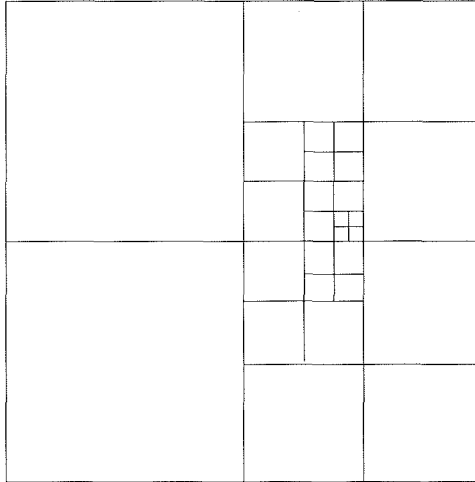


Figure 6.4: Square adaptive zonal decomposition in the context of fast summation algorithm for velocity calculations

The only criterion for calculating the near field or far field effects can be determined by the following process. To implement the fast summation algorithm

efficiently, a square adaptive zonal decomposition is employed. The whole flow domain containing non-zero vorticity is initially contained in a single square zone. This is then divided into four sub-zones. Each zone is then further subdivided into four new zones, provided that there is a minimum number of particles in the zone, thus creating a hierarchical structure of zones as shown in figure (6.4). For each zone, the parent zone, and any children(sub-zones) of the zone are recorded, along with which particles are stored in that zone. By using the complex notation, the centres of the control volume i and the zone can be represented by Z_i and Z_c respectively. Then the contribution of the zone to the velocity at point Z_i can be calculated from a series expansion using the following formula, provided the distance between Z_i and Z_c is greater than some factor times the radius λ of the zone so that the Laurent series will converge:

$$u^\tau(Z_i) - iv^\tau(Z_i) = \sum_{k=1}^{N_t} \frac{\alpha_k}{2\pi i (Z_i - Z_c)^k} \quad (6.20)$$

where $\alpha_k = \sum_j^{N_p} \Gamma_j (Z_j - Z_c)^{k-1}$ and N_p is the total number of vortex particles contained in the zone. Once the influence of a zone is calculated, the children of this zone are then ignored, as all the particles in the zone have been taken into account. If the centre of a control volume is too close to Z_c for the series to converge, then the zone's children are considered in the same way. This process continues until the series expansion can be used, or the smallest zone is reached, and if the series will still not converge, the velocity contribution is calculated from direct summation. The hierarchical structure in the algorithm means that the largest possible zone is used at all times.

6.4 Implementation of boundary conditions

For convenience of description, in the following sections the cells immediately adjacent to the body surface will be referred to as boundary cells and the remaining

cells are called non-boundary cells. At each time-step t , after solving the vorticity transport equation, the new vorticity values at time $t + \Delta t$ in the non-boundary cells are known. For the boundary cells, however, the new vorticity values depend not only on the neighbouring cells through convection and diffusion, but also on the new vorticity(flux) created at the body surface during the time-step Δt . The rate of the vorticity creation per unit length at the body surface can be represented by $-\nu \frac{\partial \omega}{\partial n'}$, see figure (6.6). Considering a boundary control volume with node points j and $j + 1$ shown in figure (6.5), the vorticity at time $t - \Delta t$ is assumed to be ω' . After convection and diffusion through the interfaces (not including the new vorticity generated at the body surface) during a time interval Δt , which is represented by the symbols \longrightarrow and \longleftarrow respectively, the residual vorticity will be ω'' . If the new vorticity in the control volume at time t is calculated as ω , then the vorticity flux per unit length through the body surface is

$$-\nu \frac{\partial \omega}{\partial n'} = \frac{(\omega - \omega'')A_{\Omega_i}}{\Delta t \Delta s'} \quad (6.21)$$

where A_{Ω_i} is the area of control volume Ω_i .

The new vorticity values for each boundary control volume, and hence the surface vorticity flux entering each boundary control volume, can then be determined by implementing the velocity boundary conditions. This leads to a set of linear algebraic equations which must be solved at each time step to obtain the vorticity in the boundary cells.

Theoretically, for the formulation based on the vorticity and velocity description of the flow, the no-penetration and no-slip condition are equivalent in determining the boundary vorticity flux, that is either condition can be used but not both[123][67]. More specifically, if the no-slip condition is used, the no-penetration condition will be automatically satisfied, and vice versa. In such a way, the entire boundary condition can be satisfied without overspecifying the problem. In the ac-

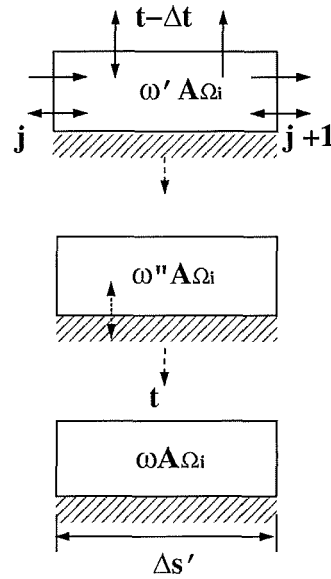


Figure 6.5: Illustration for surface vorticity flux calculation

tual calculation, the contour of the body is divided into a number of panels, each of which also constitutes a segment(face) of the boundary cells. If the no-slip condition is implemented, then, for each panel, a control point must be chosen on which the tangential velocity induced by all the cells is zero. Usually, the midpoint or quarter point of the panel is used. However, although it can be proven that implementation of the no-slip boundary condition leads to conservation of vorticity in the flow field, it is impossible, by the numerical approach, to enforce the zero tangential velocity condition at all points along the panel, which, it has been found, can lead to large errors for long time calculation, as vorticity conservation can not be guaranteed. One alternative approach to satisfying the boundary conditions is by using the no-penetration condition, which can, of course, be implemented at only one point for each panel. The best way, however, is to ensure the mass flux through each panel is zero by using $\psi_j = \psi_{j+1}$ or $\int_{P_j} \mathbf{u} \cdot \mathbf{n}' ds' = 0$, if the body is stationary, for panel P_j with node points j and $j + 1$. More specifically, for each panel $P_j, j = 1, 2, \dots, N_p$, the mass flux F'_j due to the velocity field in the flow region consists of three parts,

that is

$$F'_j = \int_{P_j} \vec{u} \cdot \vec{n}' ds' = F_{jF} + F_{jB} + F_{jW} \quad (6.22)$$

which represents respectively the contribution from the free stream, vorticity in the boundary cells and vorticity in the remaining cells. The flux from the free stream F_{jF} can be calculated as

$$F_{jF} = \int_j \vec{u}_\infty \cdot \vec{n}' ds'_j \quad (6.23)$$

while the flux from the vorticity in the boundary cells is

$$F_{jB} = \sum_{i=1}^{N_p} \omega_i(t) \int_j (\vec{S}_i \cdot \vec{n}') ds'_j \quad (6.24)$$

where vorticity value $\omega_i(t)$, $i = 1, 2, \dots, N_p$ are unknowns to be solved at each time step and meaning of the vector \vec{S}_i can be found in equation (6.15). The flux from the remaining cells with non-zero vorticity is

$$F_{jW} = \sum_{i=1}^{N_w} \omega_i(t) \int_j (\vec{S}_i \cdot \vec{n}') ds'_j \quad (6.25)$$

where N_w is the total number of those cells. Note that, in equation (6.24), the vorticity in each boundary cells includes the newly created vorticity from the body surface during the time step from $t - \Delta t$ to t and the relationship between this vorticity and the vorticity flux from the body surface is given by equation (6.21).

On the other hand, it can be shown that if the no-penetration boundary condition is implemented for $N_p - 1$ panels, then this condition will be automatically satisfied for the remaining panel. In other words, for N_p panels, only $N_p - 1$ equations are independent and another equation is needed to make the solution unique. Fortunately, the requirement of vorticity conservation, or more specifically, the integral of the vorticity flux at the body surface being zero for a stationary body, can be used as the supplemental equation:

$$\sum_{j=1}^{N_p} \int_j -\nu \frac{\partial \omega}{\partial n'} ds'_j = 0 \quad (6.26)$$

The advantage of this approach is that both the conservation of mass and vorticity in the entire flow can be guaranteed during the calculation.

6.5 Calculation of surface pressure and body forces

For viscous flow, the forces exerted on the body come from two sources: surface pressure distribution and surface friction. For the body-oriented local orthogonal coordinate system (s', \mathbf{n}') , the tangential momentum equation can be written at the surface of a stationary body as

$$\frac{1}{\rho} \frac{\partial p}{\partial s'} = -\nu s' \cdot (\nabla \times \omega \mathbf{k}) \quad (6.27)$$

which can be reduced to

$$\frac{1}{\rho} \frac{\partial p}{\partial s'} = -\nu \frac{\partial \omega}{\partial n'} \quad (6.28)$$

The term on the right-hand side of the equation is the rate of vorticity creation per unit length at the solid surface and is known for each panel after implementing the boundary conditions. So for each panel at the surface, the pressure gradient can be calculated as

$$\frac{p_j - p_{j-1}}{\rho \Delta s'_j} = -\nu \frac{\partial \omega}{\partial n'} \quad (6.29)$$

Once the pressure value at a reference point is assumed, the entire pressure distribution along the body surface can be easily calculated by integrating equation (6.29) and the body forces exerted by the surrounding fluid can then be integrated from the surface pressure distribution and the tangential friction force.

For the particular case of flow around a circular cylinder, the drag and lift can be obtained from

$$L = R \oint_{bs} \left(\mu R \frac{\partial \omega}{\partial n'} - \mu \omega \right) \cos \theta \, d\theta \quad (6.30)$$

$$D = R \oint_{bs} \left(\mu R \frac{\partial \omega}{\partial n'} - \mu \omega \right) \sin \theta d\theta \quad (6.31)$$

and the non-dimensional drag and lift coefficients of the body are then given by

$$C_D = \frac{D}{\rho U_\infty^2 R} \quad (6.32)$$

and

$$C_L = \frac{L}{\rho U_\infty^2 R} \quad (6.33)$$

where R is the radius of the circular cylinder.

6.6 Results and Discussion

To show the accuracy and efficiency of the proposed method, a number of calculations have been carried out for the flow around an impulsively started circular cylinder. This flow problem has been extensively used as a prototype of unsteady separated flows and a number of numerical and experimental results are available for validating new numerical methods. In figure (6.6), the definition sketch of the flow is given and in figure (6.7), the simple polar coordinate system used for the calculation is shown, in which the grid is uniformly distributed in the θ direction and is stretched exponentially in the r direction. Since the grids(cells) are needed only for the non-zero vorticity region, a small portion of the entire grids are used in the actual calculation. In the following discussions, both early stage development of the flow at various Reynolds numbers($Re = 2U_\infty R/\nu$) and long time evolution of the wake(Karman vortex street) for $Re = 1000$ are presented, and where possible, comparisons are made with other numerical and experimental results, particularly with the results of a high resolution simulation using the discrete vortex methods[59][100]. In [100], their results have been compared with a number of theoretical, numerical and experimental results, which provide a useful and reliable data base for validating the present method.

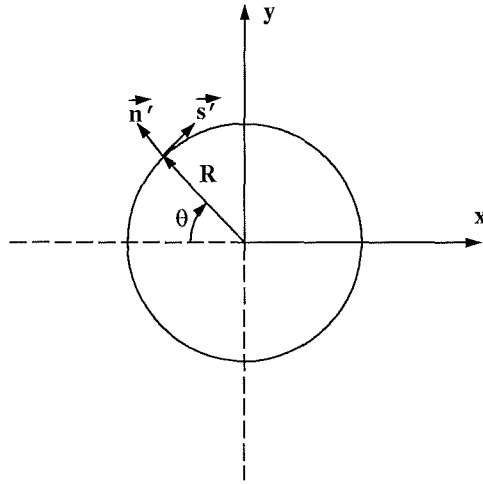


Figure 6.6: Definition sketch of the flow past a circular cylinder

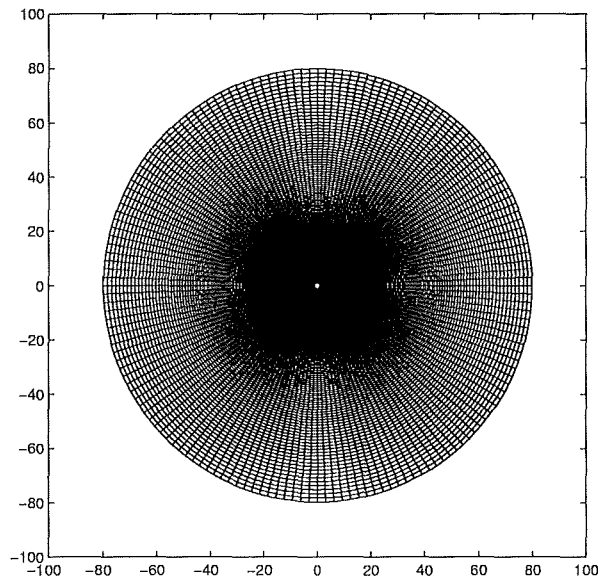


Figure 6.7: Coordinate system and the grids for the flow past a circular cylinder

6.6.1 Fast algorithm vs direct summation

To examine the performance (timing, accuracy etc.) of the fast summation algorithm, calculations using both the direct summation and fast algorithm are performed for a Reynolds number of 1000. The grid points used are 160×80 and the size of the first grid cell in the normal direction to the surface is $\Delta Y_1 = 0.02$. The time-step adopted for the calculation is $\Delta t = 0.01$ and 600 timesteps have been advanced. By the last time-step ($T = 6$), the number of active cells, i.e. the cells with a vorticity value not less than a specified value $\epsilon = 10^{-6}$, is about 5600 and the CPU time used for the direct calculation is nearly six times that of the fast algorithm. The number of terms used for calculating the Laurent series expansion is $N_t = 12$. In figure (6.8), the drag coefficients from both calculations are given and no noticeable discrepancy occurs, which indicates the high accuracy of the fast algorithm. The vorticity contours at $T = 5$ and $T = 6$ from the fast algorithm are also compared in figure (6.9) with its counterpart from the direct summation and, again, the two results are nearly identical. During the calculation, no attempt has been made regarding the optimisation of the fast algorithm and in the future, this will be investigated to gain the maximum benefit in this regard. In the following discussion, all the results are obtained by using the fast summation algorithm for calculating the velocity field.

6.6.2 Grid effects

In order to evaluate the influence of the grid density on the solution, two cases have been calculated for different grid sizes at $Re = 1000$. For the coarser grid, we have grid nodes $I \times J = 160 \times 80$ and $\Delta\theta = 2\pi/160$, $\Delta Y_1 = 0.02$; and when the grid nodes increase to 320×160 , the size of the grids has been halved in both directions. In figure (6.10), the drag coefficients calculated from the different grids are compared. The very small discrepancy indicates the grid systems are fine enough to capture all the flow structures for the Reynolds number considered. In figure (6.11), the

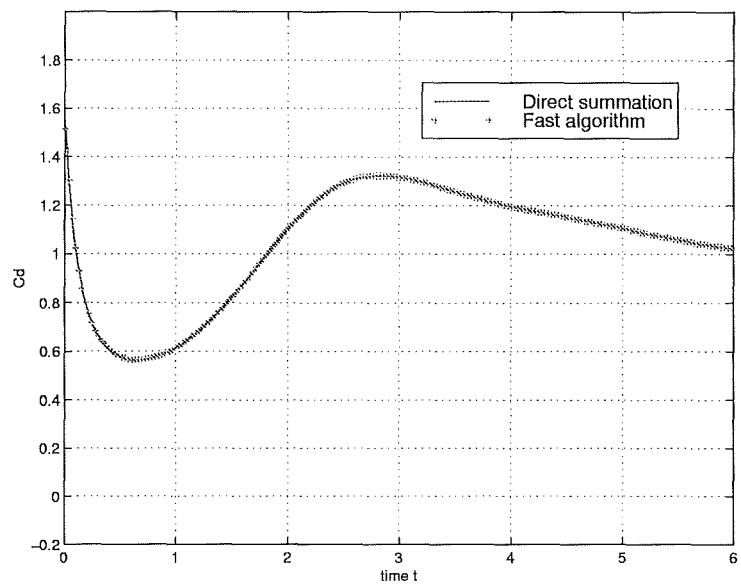


Figure 6.8: Accuracy of the fast algorithm: Drag coefficient

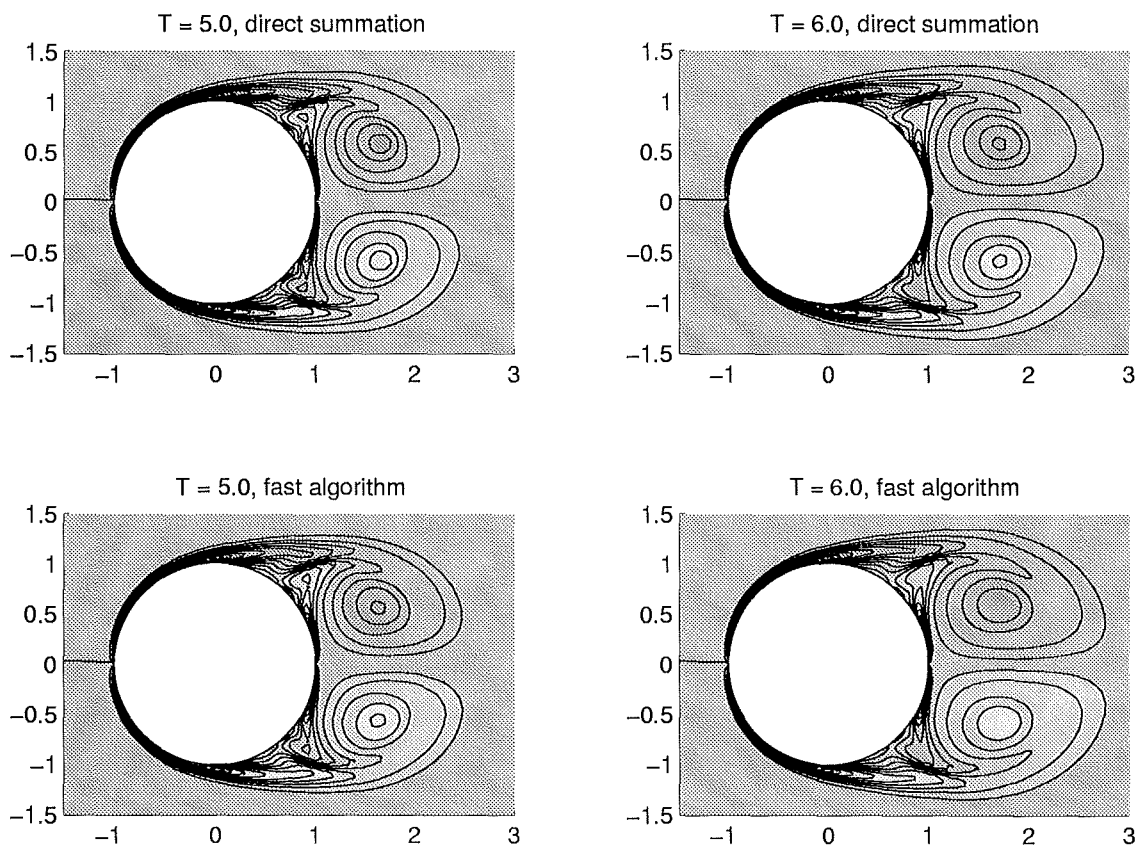


Figure 6.9: Accuracy of the fast algorithm: Vorticity contours

streamline patterns at $T = 5$ are also shown for the two cases, from which it can be seen that, although a slight difference in the size of the secondary vortex is noticeable, the global structures of the flow are the same.

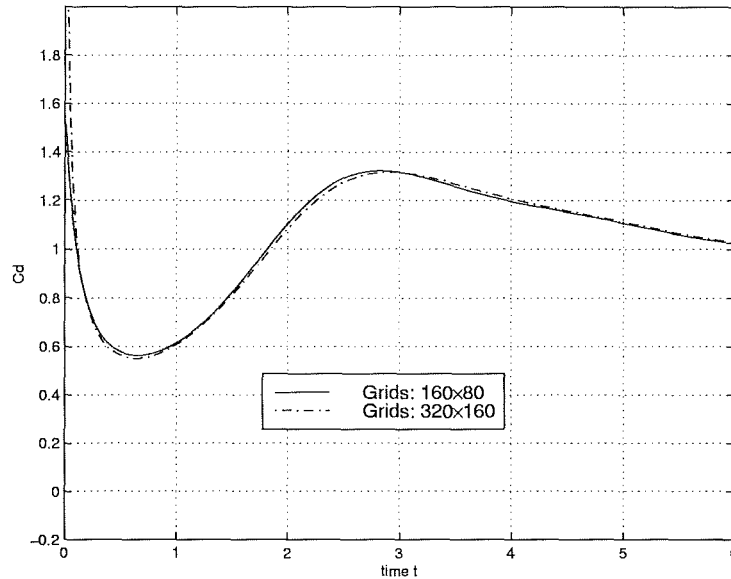


Figure 6.10: Effect of grid density on the drag coefficient

6.6.3 Comparison with other results

In this section, a number of comparisons are made between the present results and other numerical and experimental results for two different Reynolds numbers: $Re=550, 1000, 3000$ and 9500 , which represents the typical cases in terms of validation of numerical codes[59].

Re = 550

In this test case, 160×80 total grid points have been used with a minimum grid size in the normal direction to the surface $\Delta Y_1 = 0.02$ and the time step $\Delta t = 0.01$. In Fig.(6.12), the drag coefficient C_d for $T < 5.0$ is plotted and compared with the result from Shankar[100], which shows a very good agreement. In Fig. (6.13), the radial velocity distributions along the rear centre line of the circular cylinder are

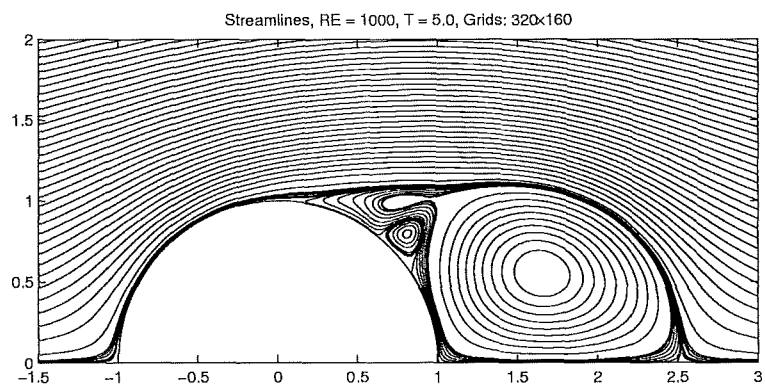
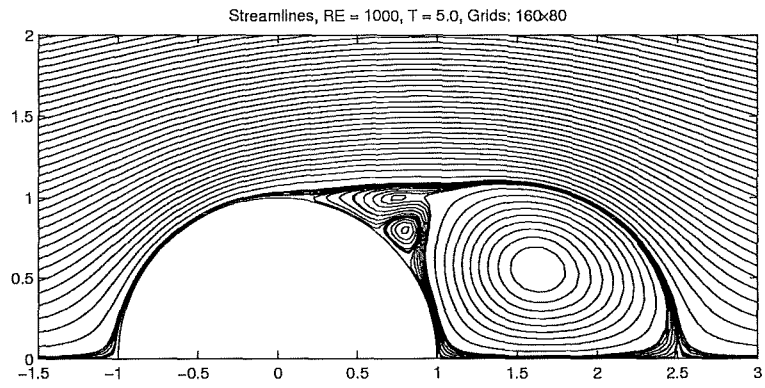


Figure 6.11: Effect of grid density on the streamlines

also compared with the result from Shankar for $T = 1.0, 2.0, 3.0, 4.0$ and 5.0 , and again excellent agreement has been achieved.

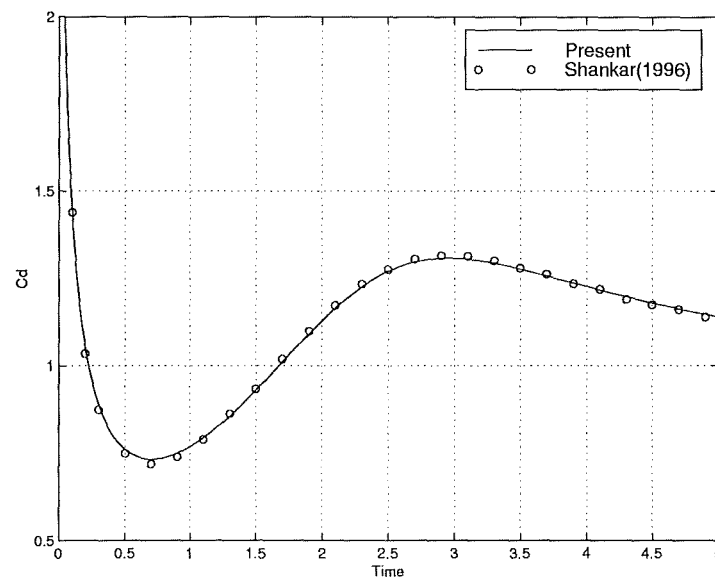


Figure 6.12: Comparison of drag coefficients, $Re = 550$

Re = 1000

For this case, 160×80 grid points have been used and the time step to advance the solution is $\Delta t = 0.01$. In figure (6.14), the history of vorticity development for the impulsively started flow are illustrated by the equi-vorticity contours, which shows that, after the sudden start of the flow, the primary vortex is formed at the rear of the cylinder and then, after time reaches $T = 2$, a secondary vortex begins to form and grow in the middle of the main vortex. The corresponding streamline pattern for $T = 5$ is given in figure (6.11), which clearly shows the secondary vortex is interacting with the primary vortex forming the so-called α phenomenon. The vorticity distribution at the surface for several instants of time are given in figure (6.15). Generally, the present results are in good agreement with those from the computations of Koumoutsakos & Leonard using a high resolution discrete vortex method[59].

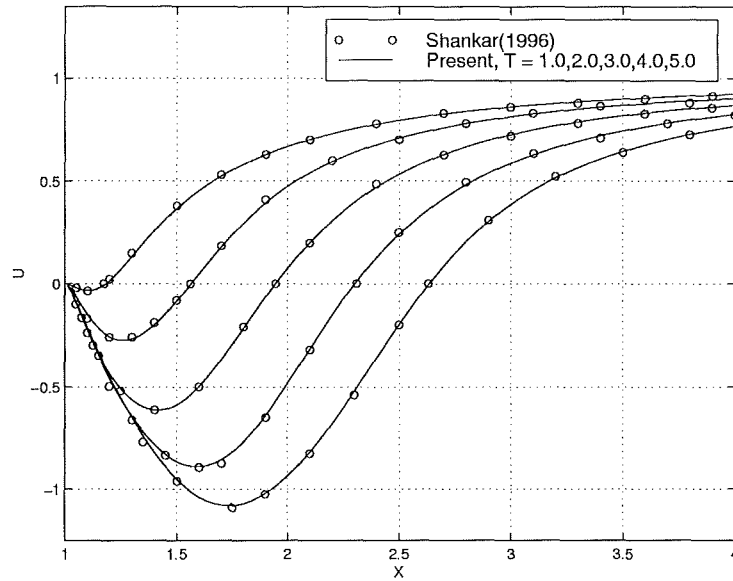


Figure 6.13: Radial velocity distribution along the rear centre line of the circular cylinder, $Re = 550$

Figure (6.16) compares the drag coefficient evolution from the present study with other numerical results. From this figure, it can be seen that the present result agrees particularly well with the result from reference [59], although at least an order of magnitude more vortex elements were reportedly used for their simulation.

Re = 3000

As discussed by Koumoutsakos and Leonard[59], at this Reynolds number, a series of new separation phenomena appear, which poses a challenge for numerical methods to capture all the flow structures. For the results presented, 240×150 grid points have been used with a minimum grid size in the normal direction to the surface $\Delta Y_1 = 0.01$ and the time step $\Delta t = 0.005$. Figure (6.17) and figure (6.18) show the vorticity distribution at the body surface and the equi-vorticity contours for $T = 1.0, 2.0, 3.0, 4.0, 5.0$, and 6.0 , respectively. The interplay between the main vorticity and the secondary vorticity during the flow evolution has been explained in [59] and is reflected in the development of the drag coefficient. For this particular

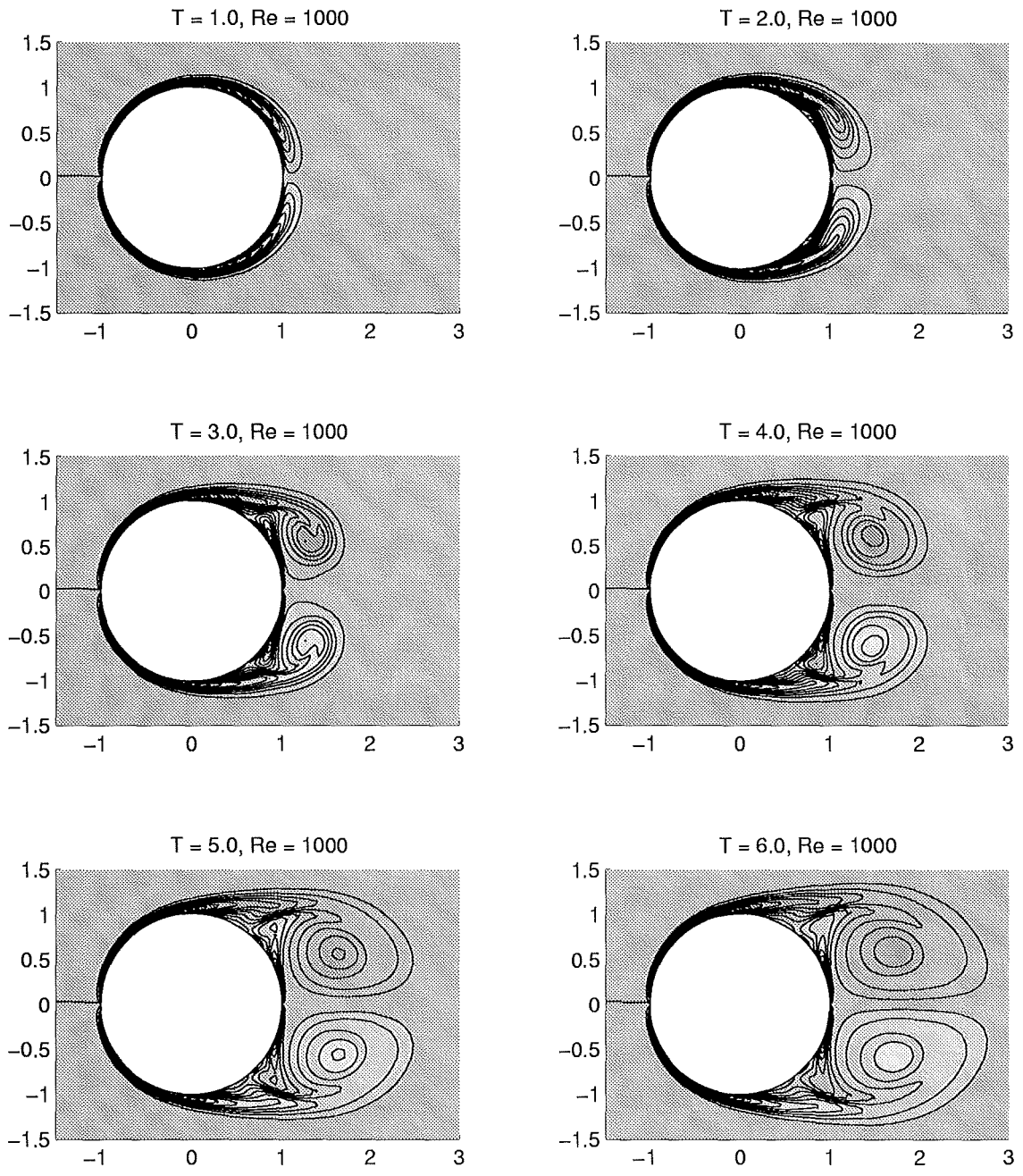


Figure 6.14: Vorticity contours: $Re = 1000$

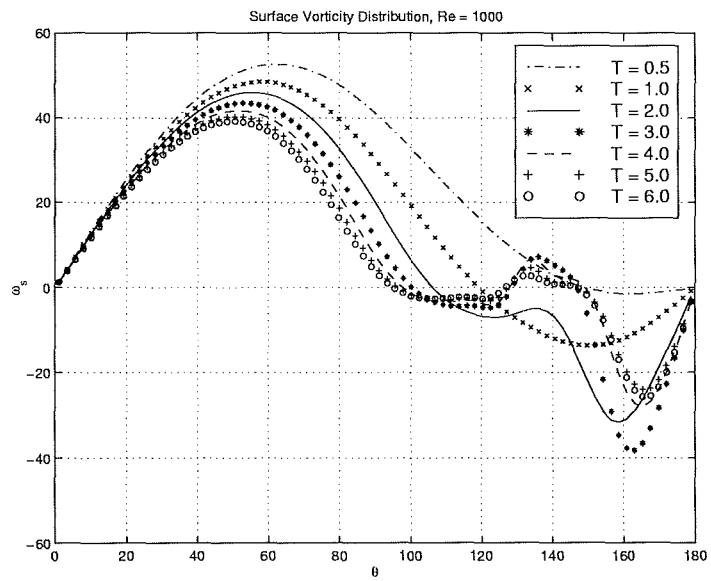


Figure 6.15: Surface vorticity distribution: $Re = 1000$

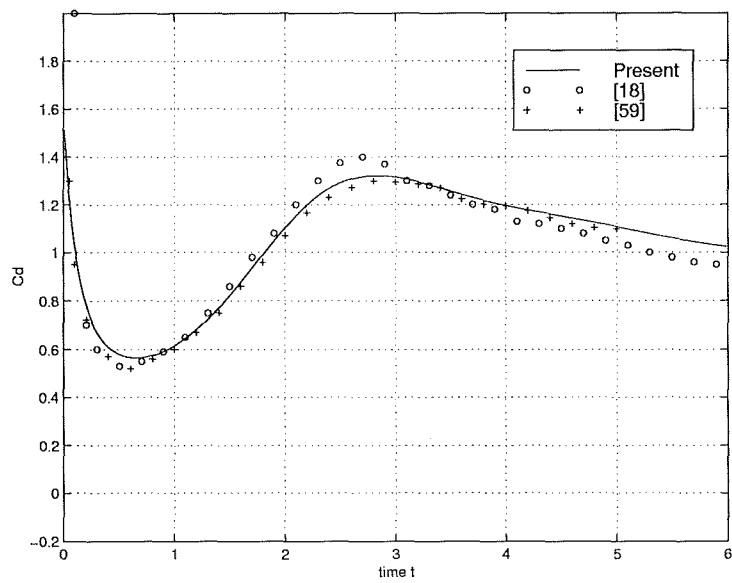


Figure 6.16: Comparison of drag coefficients: $Re = 1000$

case, a drag plateau appears between $T = 2.2$ and $T = 3.0$. From Fig.(6.19), it can be seen that this phenomena has been captured by the present method and the results compare very well with those presented by Koumoutsakos and Leonard[59] and Shankar[100]. For the present study, by the end of the calculation($T = 6.0$), the number of active cells is around 13,000, while for the same time T , 300,000 vortex elements have been used in their study. The result from Cheng[18] et al. by using a hybrid vortex method is also presented in figure (6.19) which, due to the relatively low resolution and the additional numerical diffusion, does not exhibit capture of the drag plateau.

In figure (6.19), the Cd result from a higher grid resolution(320×300) with $\Delta Y_1 = 0.005$ is also presented, which shows that better agreement with the result from Shankar has been achieved by refining the grids.

In figure (6.20), the streamlines for time $T = 5.0$ are presented, which compare well with the experimental flow visualisation of Bouard and Coutanceau[9].

In figure (6.21), the radial velocity distributions along the rear centre line of the circular cylinder are compared with the result from Shankar for $T = 1.0, 2.0, 3.0, 4.0$ and 5.0 , and again excellent agreement has been achieved.

Re = 9500

This case is the highest Re for which simulations are performed in the present study and is by far the most interesting and challenging one[59]. For the results presented , 640×280 grid points have been used with a minimum grid size in the normal direction to the surface $\Delta Y_1 = 0.005$ and the time step $\Delta t = 0.002$. Figure(6.22) and figure (6.23) show the vorticity distribution at the body surface and the equi-vorticity contours for $T = 1.0, 2.0$, and 3.0 , respectively. In figure (6.24), the Cd values are compared with those presented by Shankar[100] and Kruse and Fischer[61], which show a very good agreement among the results from different methods. For the

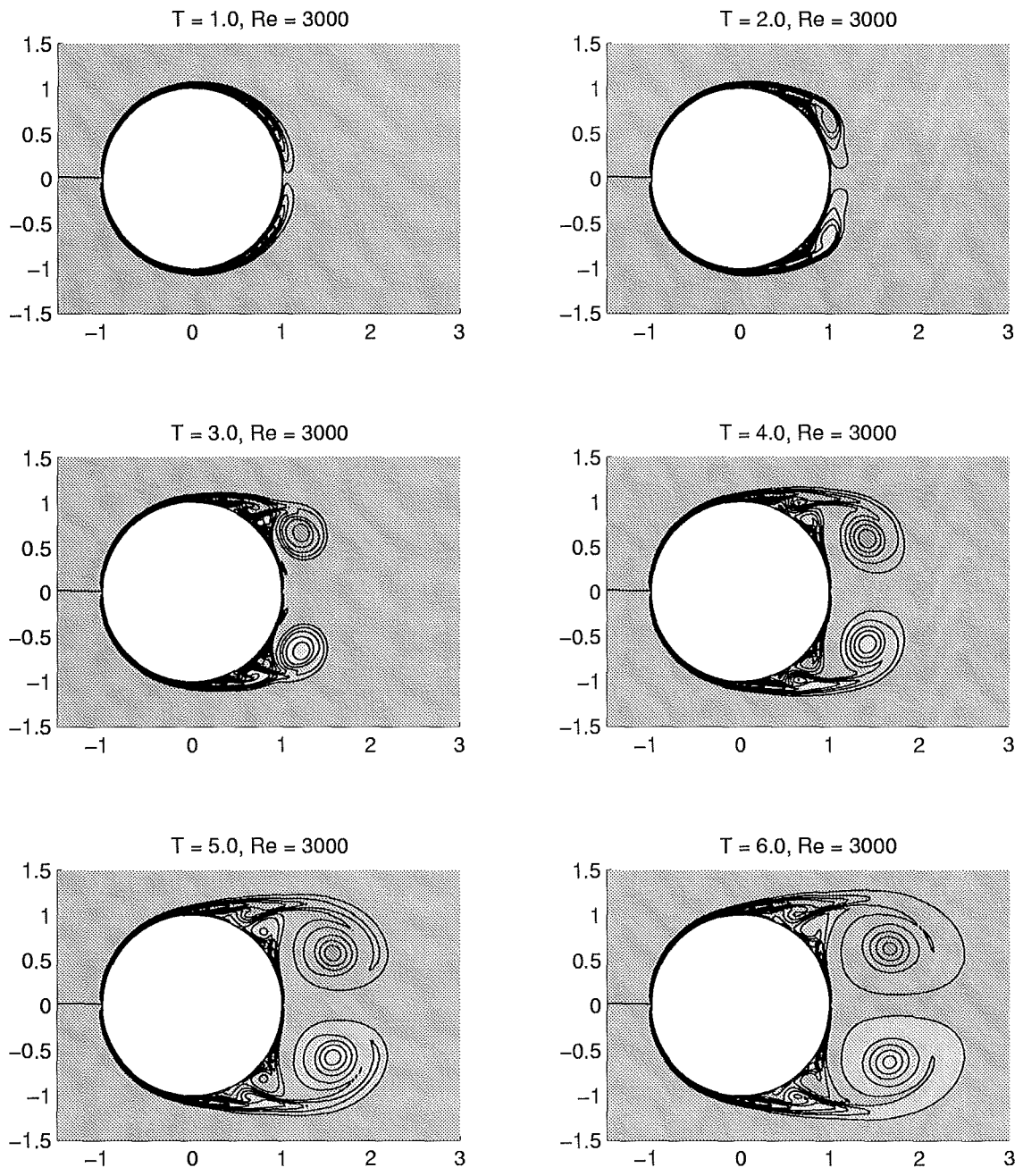


Figure 6.17: Vorticity contours: $Re = 3000$

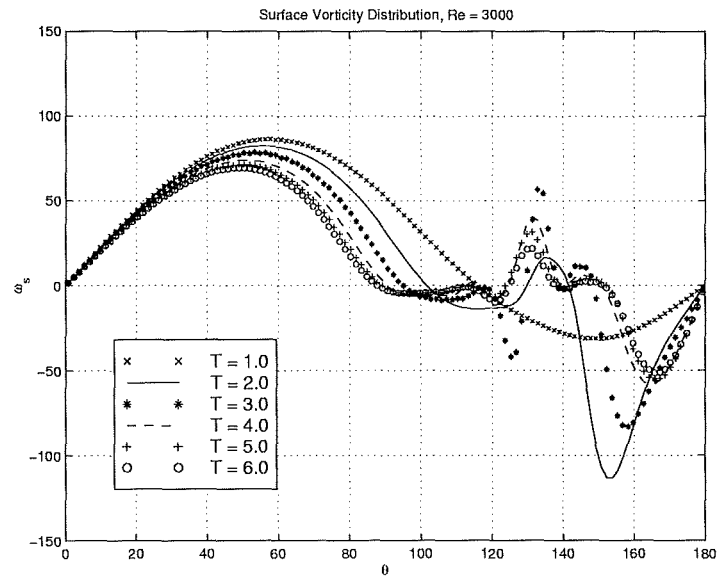


Figure 6.18: Surface vorticity distribution: $Re = 3000$

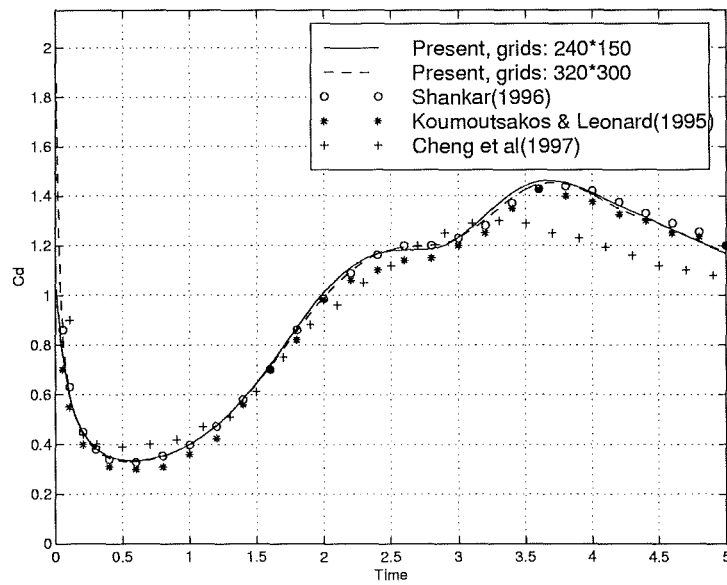
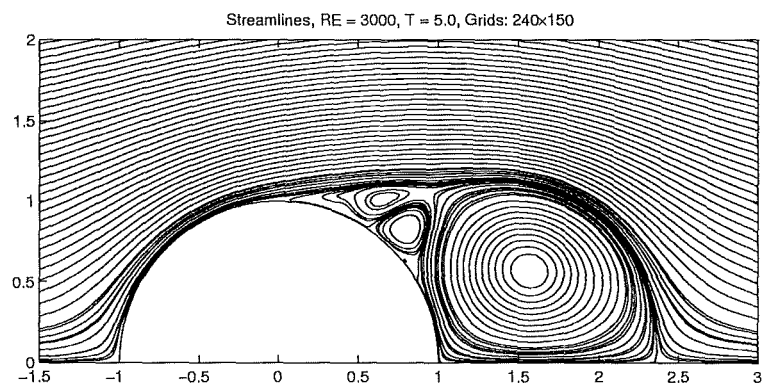


Figure 6.19: Comparison of drag coefficients, $Re = 3000$



A



B

Figure 6.20: Streamlines for $Re = 3000$ at $T = 5.0$; A: Calculated, B: Experiments[9]

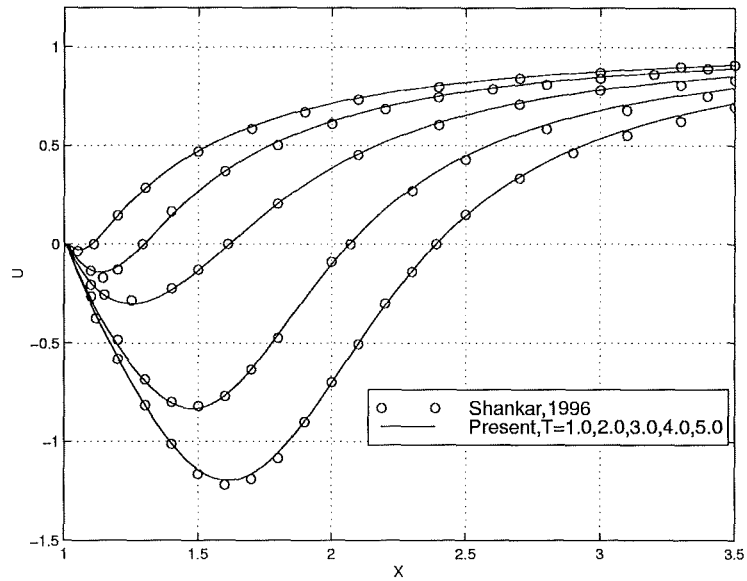


Figure 6.21: Radial velocity distribution along the rear centre line of the circular cylinder, $Re = 3000$

present study, by the end of the calculation ($T = 3.0$), the number of active cells is around 33,000, while for the same time T , 350,000 vortex elements have been used in the study by Koumoutsakos[59], 2044×254 grid points was used by Anderson and Reid[1]. In the Kruse and Fischer's work, a spectral elements method has been used to solve the Navier-Stokes equations in terms of velocity and pressure. The computational grids consists of 6112 spectral element and there are 10 nodes along each dimension in every element. Although a similar number of vortex elements were employed in the Shankar's work in which, by the end of time $T = 3.0$, 60,000 vortices are required, a far more expensive procedure was adopted therein for calculating the viscous diffusion.

In figure (6.25), the radial velocity distributions along the rear centre line of the circular cylinder are also compared with the result from Shankar for $T = 0.5, 1.0, 1.5, 2.0, 2.5, 3.0$.

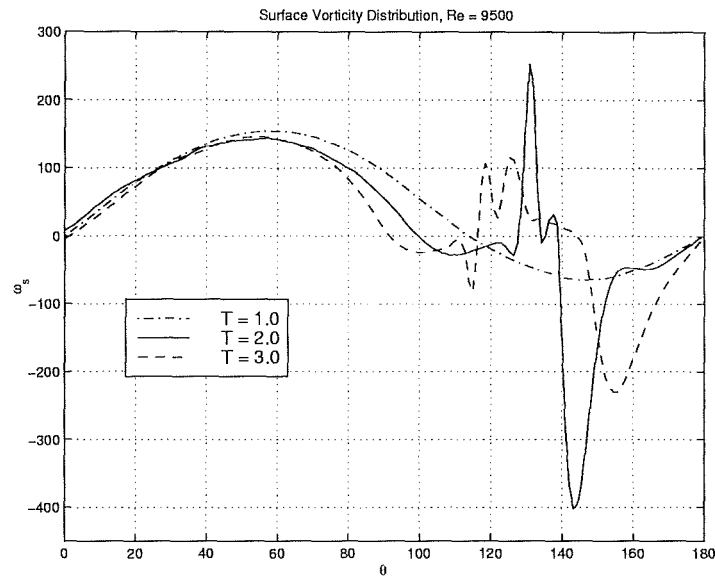


Figure 6.22: Surface vorticity distribution: $Re = 9500$

6.6.4 Long time calculation: $Re = 1000$

In this section, the long time evolution of the flow around an impulsively started cylinder at $Re = 1000$ is presented. The grid points used for the simulation is $NI \times NJ = 160 \times 220$ with $\Delta Y_1 = 0.02$ and the time step is $\Delta t = 0.01$. Figure(6.26) gives two snapshots of the flow in terms of vorticity contours, which shows vortices alternately shedding from the rear part of the cylinder. In figure (6.27), the corresponding streamlines for $T = 168$ are also given. The evolution of the drag and lift coefficients is presented in figure (6.28). In the present study, no artificial perturbation was applied to the flow to initiate the alternate vortex shedding; instead, it is triggered solely by the numerical errors(truncation and roundoff errors) during the calculation. After a long time evolution, say $T > 100$, the vortex shedding process finally settles down, forming the regular vortex pattern in the wake. From figure (6.28), it can be calculated that the average C_d value after $T > 120$ is about 1.52 and the Strouhal number St is about 0.24. Both results are in good agreement with other numerical results from 2-D simulations, as shown in table (6.1), where the

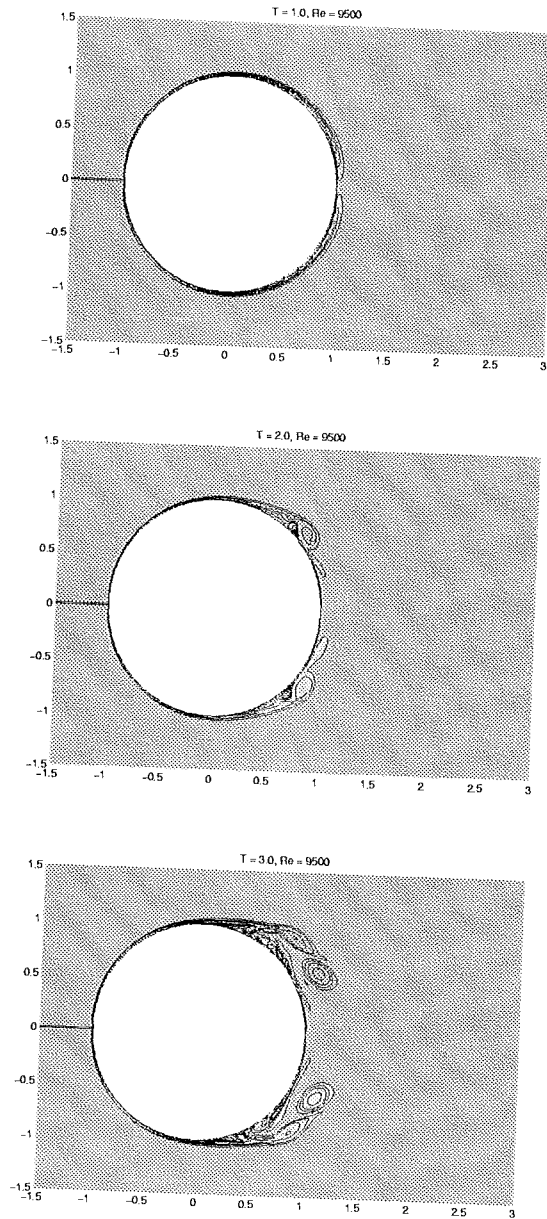


Figure 6.23: Vorticity contours: $Re = 9500$

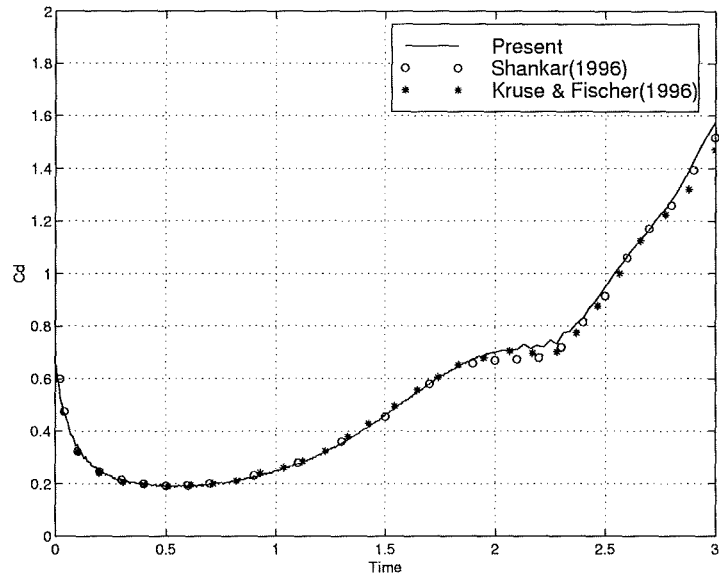


Figure 6.24: Comparison of drag coefficients, $Re = 9500$

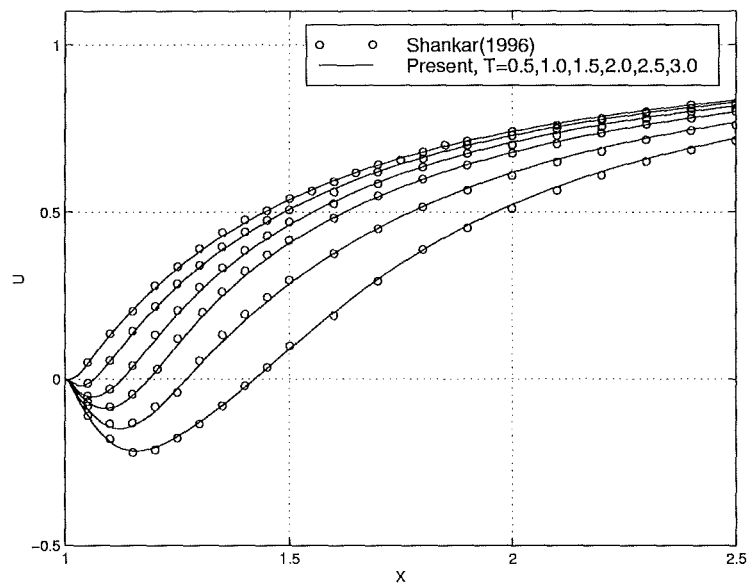


Figure 6.25: Radial velocity distribution along the rear centre line of the circular cylinder, $Re = 9500$

experimental result from Roshko et al[93] is also presented.

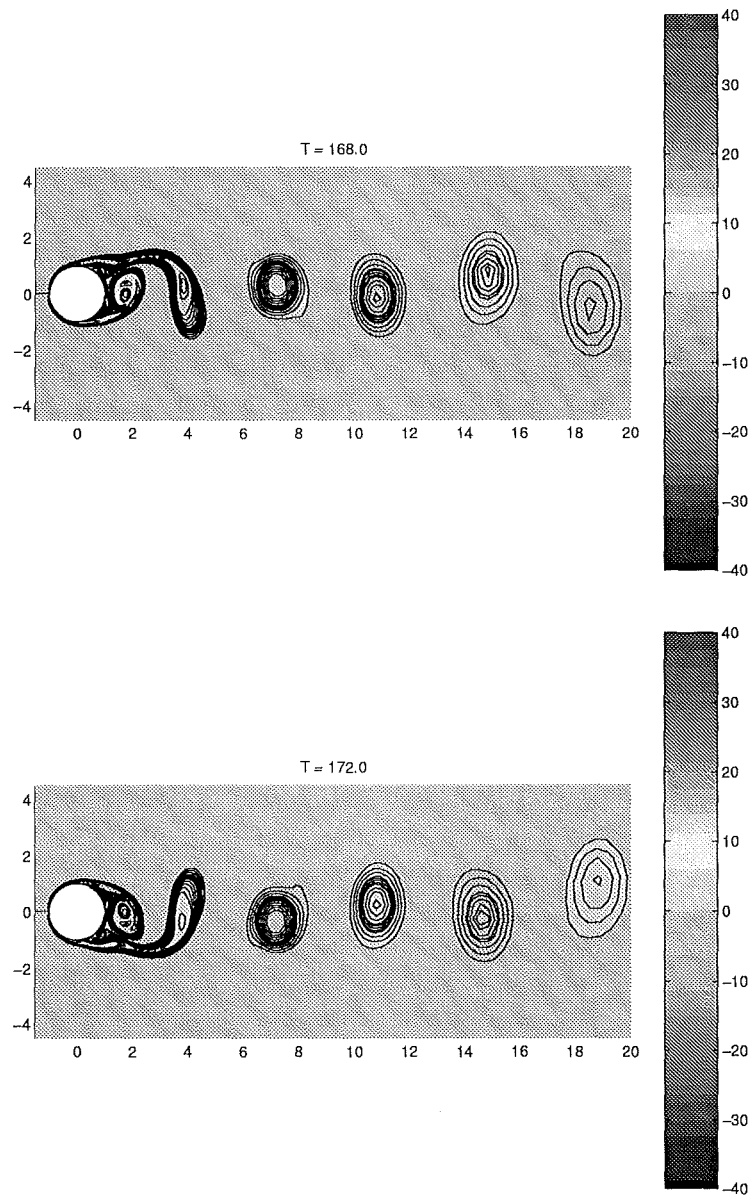


Figure 6.26: Vorticity contours for $Re = 1000$: long time calculation

6.7 Conclusions

A new method based on the vorticity formulation has been developed for unsteady incompressible viscous flow problems. By solving the vorticity transport equation using the finite volume method and calculating velocity using a modified Biot-Savart

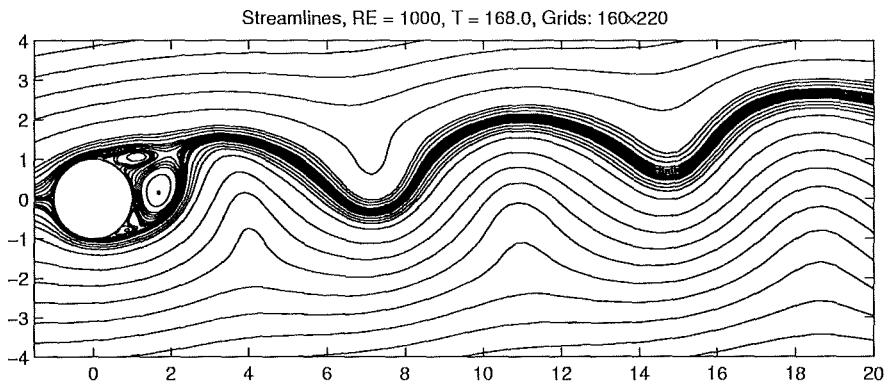


Figure 6.27: Streamlines for $Re = 1000$, $T = 168.0$

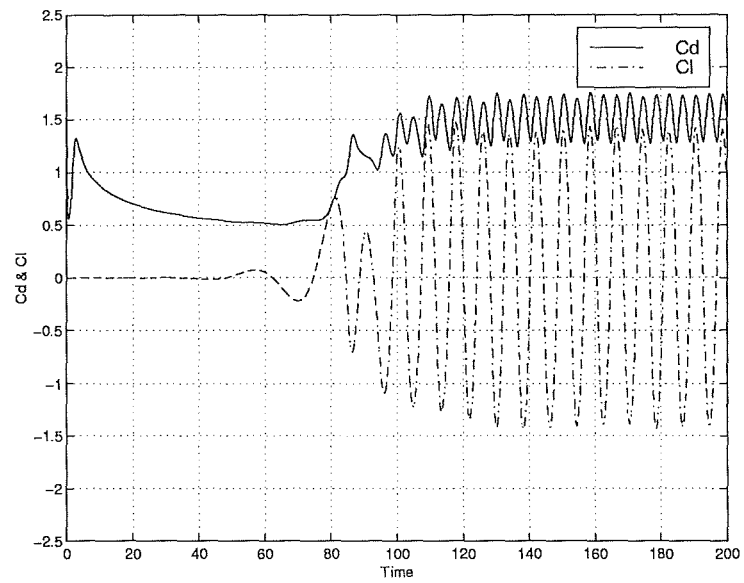


Figure 6.28: Evolution of drag and lift coefficients: $Re = 1000$

	Behr et al	Blackburn et al	Cheng et al	Mittal et al	Roshko	Present
C_d	1.53	1.51	1.23	1.53	1.20	1.52
S_t	0.241	–	0.206	0.245	0.21	0.240

Table 6.1: Drag coefficient and Strouhal number for the flow around a circular cylinder at $Re = 1000$

law, only the flow field region with non-zero vorticity needs to be solved. High efficiency has been achieved by employing an adaptive fast summation algorithm for the velocity calculations. During the calculation, mass and vorticity conservation can be guaranteed by using this approach together with the method of implementing the surface boundary conditions. The accuracy and efficiency of the method have been demonstrated by studying both the early stage development and long term evolution of the flow around an impulsively started circular cylinder at various Re number regime and by comparing present results with other numerical and experimental results. Particularly, for high Re number simulations, highly accurate solution has been obtained without using excessive large number of grid points which are needed by most other methods.

The method can be combined with the discrete vortex method in a domain decomposition approach and can also be extended to 3-D flow problems.

Chapter 7

Conclusions and Future study

7.1 2-D parallel BVI

A two-dimensional discrete vortex method has been used for simulating both a single and twin vortex system interacting with a NACA 0015 aerofoil. The main features of the method can be summarised as follows:

1. In the method, both the vorticity fields from the interaction vortex and the aerofoil surface are initially represented by a finite number of overlapping vortex blobs which are tracked through the flow region according to the local velocity calculated from the Biot-Savart law. This process introduces no numerical diffusion as opposed to the grid-based methods, which is essential to simulate high Reynolds number flow.
2. To satisfy the boundary condition at the body surface and maintain the conservation of vorticity, new vortices are introduced along the surface, which are, in part or in whole, allowed to enter the wake from the entire surface according to the local convection and diffusion of vorticity. Thus, there is no need for either a Kutta condition to determine vorticity shedding rate or empirical methods to calculate flow separation points and by using this approach, it is also made possible to capture vortex-induced separation due to vortex release from surface.

3. High efficiency of the code has been achieved by merging vortices far from the body surface and using a different, usually larger, core radius to discretise the interaction vortex(vortices), as well as incorporating a fast summation algorithm for calculating the velocity of vortices.
4. A new method has also been proposed for calculating the velocity of the nascent vortices to avoid oscillations in the normal component.

By using the method, firstly, a single vortex interacting with an aerofoil at zero angle of attack was studied. The dominant mechanisms during a BVI event, namely the effective angle of attack induced by the approaching vortex and the local effect due to passage of the vortex close by or around the surface, have been analysed using the the unsteady C_p distribution together with images of the passing interaction vortex. For relatively strong BVI, such as the head-on interaction case, vortex induced local flow separation, a phenomenon which has not been well documented in most BVI studies, has also been predicted in the present study. Some phenomena associated with the convection speed of the interaction vortex or separate parts of the vortex have been explained by the mutual interaction of the passing vortex and its induced surface vorticity. Secondly, the effects of some parameters, such as the vortex height and the incidence of the aerofoil on the strength of the interaction were examined. It was found that, although for an oncoming vortex the strongest interaction always occurs in the head-on cases, the induced effects of the vortex is not symmetric about the chord line of the aerofoil due to the nature of the vortex-induced velocity field. It was also revealed that for the cases studied the incidence of the aerofoil(below 12°) has little effect on the strength of the interaction. Finally, a twin vortex system interacting with an aerofoil has also been studied. Due to the rotation of the twin vortex system, a number of test cases have been calculated to examine the effect of the initial position of the twin vortices on the strength

and characteristics of the interaction, which reveals that both the surface pressure distribution and the resultant aerodynamic forces vary significantly with the exact position of the twin vortices.

Extensive comparisons have been made with other numerical results and the results from the Glasgow University BVI wind-tunnel test. Generally, good agreement has been achieved and the possible reasons for discrepancies in some cases have also been discussed.

7.2 Normal blade-vortex interaction

A three-dimensional discrete vortex model has been set up for studying normal vortex-body interaction. The surface of the body (blade) is represented by a number of source panels and the interaction vortex (vortex ring) is discretised into several thousand vortex particles. The strengths of the source panels are adjusted at every timestep to satisfy the no-penetration boundary condition and the vortex particles are allowed to move freely in the flow field with the local velocity. The strengths of the vortex particles are also adjusted according to the stretching of the vorticity field. Two examples have been given of a vortex ring interacting with a finite wing and a sphere. In both cases, as the vortex ring approaches the leading edge of the body, substantial deformation of the vortex ring was predicted. In the former case, the vortex ring is eventually cut by the blade and the compression of the vorticity field on either side of the blade was clearly visible, while in the second case, the vortex was not cut by the sphere and instead it elongated and wrapped around the leading edge of the sphere due to the relative thickness of the body. Quantitatively, the suction force induced by the approaching vortex has also been predicted by using a global vorticity-based method.

Due to the limitations in the available 3-D vortex particle methods, i.e. the difficulties in representing the surface vorticity and its subsequent shedding from the

surface as well as in maintaining the overlapping condition of the vortex particles, which is essential for an accurate 3-D simulation, the calculation inevitably terminated at some time after the vortex cut through the blade or became very thin around the sphere. To simulate the entire penetration process of the vortex, it is the author's belief that in the future study, better results could be obtained by introducing a body-fitted grid system around the body surface, particular in the region of interaction. When the vortex particles come into these grids(cells) their vorticity will be interpolated to the centroid of each grid(cell) and then the centred finite volume method could be used to solve the vorticity transport equation. In this approach, unlike the vortex-in-cell method, the velocity of the flow field and the surface vorticity will still be calculated from the Biot-Savart law to keep some advantages of the vortex particle method while the fast summation method developed in the present study could be used to reduce the computational cost. In such a way, it is possible to have a detailed examination of vortex-boundary layer interaction, which is a challenge in both numerical and physical aspects of the 3-D vortex-body interaction problem.

7.3 Fast summation algorithm

A 3-D version of the fast summation algorithm based on the general Taylor expansions has been developed for the vortex particle method. High efficiency of the code is achieved by employing the incomplete tree-code for vortex sorting and velocity calculations. The adaptivity of the code reduces memory requirement, which is essential for the method to be applied to a large number of vortex particles.

The main features of the method are that, firstly, it can be directly applied to the kernel for calculating the velocity; so only first derivatives are needed to calculate the stretching term, while in the multipole expansion method, both the first and second derivatives are needed to calculate the velocity and the stretching

term respectively. Secondly, it is simpler than the multipole expansion method in terms of mathematical formulation.

The details of the formulation and implementation of the algorithm have been discussed and the performance of the fast summation is tested by calculating the interaction of two vortex rings. The results show that the present method provides a simpler alternative to the fast multipole method and has the potential to be applied to practical flow problems.

7.4 The new hybrid vorticity-based method

A novel hybrid vorticity-based method, which combines some favourable features in the discrete vortex method and the finite volume methods has been developed in the study. In this method, the vorticity transport equation is solved by the cell-centred finite volume method and the velocities needed at the centre of each control volume are calculated by a modified Biot-Savart formula in conjunction with a fast summation algorithm. The vorticity and mass conservation in the flow are guaranteed during the calculation by virtue of the finite volume approach and the method of implementing the boundary conditions at the body surface. As an example, both the early stage development and long term evolution of the flow around an impulsively started circular cylinder are computed using the method and good agreement has been achieved between present results and other numerical and experimental results.

Although only the 2-D version of the method is presented in the present study, it is relatively straightforward to extend the method to 3-D problems.

7.5 Concluding remarks

This study has shown that the vortex methods are useful tools to analyse both 2-D and 3-D vortex-body interaction problems which are of particular interest to

the helicopter industry and other relevant industrial sectors. The future work will include a detailed study of both 2-D and 3-D vortex boundary layer (laminar and turbulent) interaction and this can be achieved by combining the discrete vortex method and the new hybrid vorticity-based method. More specifically, the new hybrid vorticity-based method can be used in the viscous region near the body surface and the vortex particle method can be applied to the outer region of the essentially inviscid flow. The coupling of the two methods has been made possible and easy due to the fact that same technique(via Biot-Savart law) has been used in both the methods to calculate the velocity field. In such a way, the advantage of discrete vortex method in capturing global characteristics of the vortical flow and the advantage of the grid-based method in describing the detailed flow structures can be fully explored.

Appendix A

Recurrence relations for

$$a_k(\mathbf{x}, \mathbf{y}_\tau) = \frac{1}{k!} D_{\mathbf{y}}^k f(\mathbf{x}, \mathbf{y})_{\mathbf{y}=\mathbf{y}_\tau}$$

The coefficients $a_k(\mathbf{x}, \mathbf{y}_\tau) = \frac{1}{k!} D_{\mathbf{y}}^k f(\mathbf{x}, \mathbf{y})_{\mathbf{y}=\mathbf{y}_\tau}$ can be calculated from the following recurrence relations:

$$\begin{aligned} a_{0,0,0} &= f(\mathbf{x}, \mathbf{y}_\tau) \\ a_{k_1, k_2, k_3} &= g^2 \left[\frac{2k_1 + 1}{k_1} (x_1 - y_{\tau 1}) a_{k_1-1, k_2, k_3} + 2(x_2 - y_{\tau 2}) a_{k_1, k_2-1, k_3} \right. \\ &\quad + 2(x_3 - y_{\tau 3}) a_{k_1, k_2, k_3-1} - \frac{k_1 + 1}{k_1} a_{k_1-2, k_2, k_3} \\ &\quad \left. - a_{k_1, k_2-1, k_3} - a_{k_1, k_2, k_3-2} \right], \text{ for } k_1 \neq 0 \end{aligned}$$

$$\begin{aligned} a_{k_1, k_2, k_3} &= g^2 \left[2(x_1 - y_{\tau 1}) a_{k_1-1, k_2, k_3} + \frac{2k_2 + 1}{k_2} (x_2 - y_{\tau 2}) a_{k_1, k_2-1, k_3} \right. \\ &\quad + 2(x_3 - y_{\tau 3}) a_{k_1, k_2, k_3-1} - a_{k_1-2, k_2, k_3} \\ &\quad \left. - \frac{k_2 + 1}{k_2} a_{k_1, k_2-2, k_3} - a_{k_1, k_2, k_3-1} \right], \text{ for } k_2 \neq 0 \end{aligned}$$

$$\begin{aligned} a_{k_1, k_2, k_3} &= g^2 \left[2(x_1 - y_{\tau 1}) a_{k_1-1, k_2, k_3} + 2(x_2 - y_{\tau 2}) a_{k_1, k_2-1, k_3} \right. \\ &\quad + \frac{2k_3 + 1}{k_3} (x_3 - y_{\tau 3}) a_{k_1, k_2, k_3-1} - a_{k_1-2, k_2, k_3} \\ &\quad \left. - a_{k_1, k_2-2, k_3} - \frac{k_3 + 1}{k_3} a_{k_1, k_2, k_3-2} \right], \text{ for } k_3 \neq 0 \end{aligned}$$

where $g^2 = \frac{1}{(x_1 - y_{\tau 1})^2 + (x_2 - y_{\tau 2})^2 + (x_3 - y_{\tau 3})^2}$; and $a_{i,j,k} = 0$, if $i < 0$, or $j < 0$, or $k < 0$.

Appendix B

Proof of equation 2.26

Now, we can prove equation 2.26 by using following identities and integral theorems:

$$(1) \nabla \cdot (f\mathbf{G}) = \mathbf{G} \cdot \nabla f + f\nabla \cdot \mathbf{G}$$

$$(2) \nabla \times (f\mathbf{G}) = f\nabla \times \mathbf{G} + \nabla f \times \mathbf{G}$$

$$(3) \nabla \times (\mathbf{G} \times \mathbf{H}) = (\mathbf{H} \cdot \nabla)\mathbf{G} - (\mathbf{G} \cdot \nabla)\mathbf{H} + \mathbf{G}(\nabla \cdot \mathbf{H}) - \mathbf{H}(\nabla \cdot \mathbf{G})$$

$$(4) \nabla(\mathbf{G} \cdot \mathbf{H}) = \mathbf{G} \times (\nabla \times \mathbf{H}) + \mathbf{H} \times (\nabla \times \mathbf{G}) + (\mathbf{G} \cdot \nabla)\mathbf{H} + (\mathbf{H} \cdot \nabla)\mathbf{G}$$

$$(5) \nabla \times \nabla f = 0$$

$$(6) \nabla \cdot (\nabla \times \mathbf{G}) = 0$$

$$(7) \int (\nabla \cdot \mathbf{G}) dv = \int \mathbf{G} \cdot \mathbf{n} ds$$

$$(8) \int (\nabla \times \mathbf{G}) dv = \int \mathbf{n} \times \mathbf{G} ds$$

$$(9) \nabla_{\mathbf{x}} \cdot (\nabla_{\mathbf{x}'} \frac{1}{r(\mathbf{x}, \mathbf{x}')})) = 0, \text{ for } \mathbf{x} \neq \mathbf{x}'$$

$$(10) \nabla_{\mathbf{x}'} \frac{1}{r(\mathbf{x}, \mathbf{x}')} = -\nabla_{\mathbf{x}} \frac{1}{r(\mathbf{x}, \mathbf{x}')}, \text{ where } r = \sqrt{x^2 + y^2 + z^2}$$

For a solid body translating with velocity $\mathbf{U}_{bt}(t)$ and rotating around a fixed point \mathbf{o} with angular velocity $\Omega(t)$, the velocity $\mathbf{U}_b(\mathbf{x}', t)$ at any point \mathbf{x}' inside the body can be expressed as

$$\mathbf{U}_b(\mathbf{x}', t) = \mathbf{U}_{bt}(t) + \Omega(t) \times (\mathbf{x}' - \mathbf{x}_o) \quad (\text{B.1})$$

and we have

$$\omega(\mathbf{x}') = \nabla_{\mathbf{x}'} \times \mathbf{U}_b(\mathbf{x}', t) = 2\Omega(t) \quad (\text{B.2})$$

and

$$\nabla_{\mathbf{x}'} \cdot \mathbf{U}_b(\mathbf{x}', t) = 0 \quad (\text{B.3})$$

Because

$$\begin{aligned}
& \int_{vb} \omega(\mathbf{x}') \times \nabla_{\mathbf{x}'} G(\mathbf{x}, \mathbf{x}') dv(\mathbf{x}') \\
&= - \int_{vb} \omega(\mathbf{x}') \times \nabla_{\mathbf{x}} G(\mathbf{x}, \mathbf{x}') dv(\mathbf{x}') \\
&= - \nabla_{\mathbf{x}} \times \int_{vb} \frac{\omega}{r(\mathbf{x}, \mathbf{x}')} dv(\mathbf{x}') \\
&= - \nabla_{\mathbf{x}} \times \int_{vb} \frac{\nabla_{\mathbf{x}'} \times \mathbf{U}_b(\mathbf{x}')}{r(\mathbf{x}, \mathbf{x}')} dv(\mathbf{x}') \\
&= - \nabla_{\mathbf{x}} \times \int_{vb} \nabla_{\mathbf{x}'} \times \frac{\mathbf{U}_b(\mathbf{x}')}{r(\mathbf{x}, \mathbf{x}')} dv(\mathbf{x}') + \nabla_{\mathbf{x}} \times \int_{vb} \nabla_{\mathbf{x}'} \frac{1}{r(\mathbf{x}, \mathbf{x}')} \times \mathbf{U}_b(\mathbf{x}') dv(\mathbf{x}') \\
&= - \nabla_{\mathbf{x}} \times \int_{bs} \frac{\mathbf{n} \times \mathbf{U}_b(\mathbf{x}')}{r(\mathbf{x}, \mathbf{x}')} ds(\mathbf{x}') + \int_{vb} (\mathbf{U}_b(\mathbf{x}') \cdot \nabla_{\mathbf{x}}) (\nabla_{\mathbf{x}'} \frac{1}{r(\mathbf{x}, \mathbf{x}')}) dv(\mathbf{x}') \\
&= - \int_{bs} \nabla_{\mathbf{x}} \frac{1}{r(\mathbf{x}, \mathbf{x}')} \times (\mathbf{n} \times \mathbf{U}_b(\mathbf{x}')) ds(\mathbf{x}') + \int_{vb} (\mathbf{U}_b(\mathbf{x}') \cdot \nabla_{\mathbf{x}}) (\nabla_{\mathbf{x}'} \frac{1}{r(\mathbf{x}, \mathbf{x}')}) dv(\mathbf{x}') \\
&= - \int_{bs} (\mathbf{n} \times \mathbf{U}_b(\mathbf{x}')) \times \nabla_{\mathbf{x}'} \frac{1}{r(\mathbf{x}, \mathbf{x}')} ds(\mathbf{x}') + \int_{vb} (\mathbf{U}_b(\mathbf{x}') \cdot \nabla_{\mathbf{x}}) (\nabla_{\mathbf{x}'} \frac{1}{r(\mathbf{x}, \mathbf{x}')}) dv(\mathbf{x}')
\end{aligned} \quad (\text{B.4})$$

and

$$\begin{aligned}
0 &= \int_{vb} \nabla_{\mathbf{x}'} \cdot \mathbf{U}_b(\mathbf{x}') \nabla_{\mathbf{x}'} \frac{1}{r(\mathbf{x}, \mathbf{x}')} dv(\mathbf{x}') \\
&= -\nabla_{\mathbf{x}} \int_{vb} \frac{1}{r(\mathbf{x}, \mathbf{x}')} (\nabla_{\mathbf{x}'} \cdot \mathbf{U}_b(\mathbf{x}')) dv(\mathbf{x}') \\
&= -\nabla_{\mathbf{x}} \int_{vb} \nabla_{\mathbf{x}'} \cdot \left(\frac{\mathbf{U}_b(\mathbf{x}')}{r(\mathbf{x}, \mathbf{x}')} \right) dv(\mathbf{x}') + \nabla_{\mathbf{x}} \int_{vb} \mathbf{U}_b(\mathbf{x}') \cdot \nabla_{\mathbf{x}'} \frac{1}{r(\mathbf{x}, \mathbf{x}')} dv(\mathbf{x}') \\
&= -\nabla_{\mathbf{x}} \int_{bs} \frac{\mathbf{U}_b(\mathbf{x}') \cdot \mathbf{n}}{r(\mathbf{x}, \mathbf{x}')} ds(\mathbf{x}') + \nabla_{\mathbf{x}} \int_{vb} \mathbf{U}_b(\mathbf{x}') \cdot \nabla_{\mathbf{x}'} \frac{1}{r(\mathbf{x}, \mathbf{x}')} dv(\mathbf{x}') \\
&= \int_{bs} (\mathbf{U}_b(\mathbf{x}') \cdot \mathbf{n}) \nabla_{\mathbf{x}'} \frac{1}{r(\mathbf{x}, \mathbf{x}')} ds(\mathbf{x}') + \int_{vb} (\mathbf{U}_b(\mathbf{x}') \cdot \nabla_{\mathbf{x}}) \left(\nabla_{\mathbf{x}'} \frac{1}{r(\mathbf{x}, \mathbf{x}')} \right) dv(\mathbf{x}')
\end{aligned}$$

So

$$\nabla_{\mathbf{x}} \int_{vb} \mathbf{U}_b(\mathbf{x}') \cdot \nabla_{\mathbf{x}'} \frac{1}{r(\mathbf{x}, \mathbf{x}')} dv(\mathbf{x}') = - \int_{bs} (\mathbf{U}_b(\mathbf{x}') \cdot \mathbf{n}) \nabla_{\mathbf{x}'} \frac{1}{r(\mathbf{x}, \mathbf{x}')} ds(\mathbf{x}') \quad (\text{B.5})$$

Inserting equation (B.4) in (B.5), one can obtain

$$\begin{aligned}
& - \int_{bs} \{ (\mathbf{n} \times \mathbf{U}(\mathbf{x}')) \times \nabla_{\mathbf{x}'} G(\mathbf{x}, \mathbf{x}') + (\mathbf{n} \cdot \mathbf{U}(\mathbf{x}')) \nabla_{\mathbf{x}'} G(\mathbf{x}, \mathbf{x}') \} ds(\mathbf{x}') \\
& \qquad \qquad \qquad = \int_{vb} \boldsymbol{\omega}(\mathbf{x}') \times \nabla_{\mathbf{x}'} G(\mathbf{x}, \mathbf{x}') dv(\mathbf{x}') \quad (\text{B.6})
\end{aligned}$$

Bibliography

- [1] C.R. Anderson and Marc B. Reider, 'A High Order Explicit Method for the Computation of Flow About a Circular Cylinder', *Journal of Computational Physics*, **125**, 207–224(1996).
- [2] A. W. Appel, 'An Efficient Program for Many-Body Simulation', *SIAM Journal of Scientific and Statistical Computation*, **6**, 85–103, 1985.
- [3] P.K. Banerjee and L. Morino, 'Boundary Element Methods in Nonlinear Fluid Dynamics', Elsevier Applied Science, 1992.
- [4] J. Barnes, Hut, P., 'A Hierarchical $O(N \log N)$ Force Calculation Algorithm', *Nature*, **324**, 446–449, 1986.
- [5] G.R. Batchelor, 'An Introduction to Fluid Dynamics', Cambridge University, 1967.
- [6] M. Behr, J. Liou, R. Shih and T.E. Tezduyar, 'Vorticity-stream Function Formulation of Unsteady Incompressible Flow around a Cylinder: sensitivity of the computed flow field to the location of the outflow boundary', *Int. J. Numer. Meth. Fluid*, 323-342, 1991.
- [7] H.M. Blackburn and R.D. Henderson, 'A Study of Two-dimensional Flow Past an Oscillating Cylinder', *Journal of Fluid Mechanics*, **385**, 255–286, 1999.
- [8] E.R. Booth and J.C. Yu, 'Two-Dimensional Blade-Vortex Flow Visualization Investigation', *AIAA Journal*, **24**, 1468–1473, 1986.

- [9] R. Bouard and M. Coutancea, 'The Early Stage Development of the Wake behind an Impulsively Started Cylinder for $40 < Re < 10^4$ ', *Journal of Fluid Mechanics*, **101**, 587-607, 1980.
- [10] A. Brocklehurst and A.C. Pike, 'Reduction of BVI Noise Using a Vane Tip', *AHS Aeromechanics Specialists Conference*, San Francisco, January, 1994.
- [11] S.F.J. Butler, 'A Note on Stokes Stream Function for Motion with a Spherical Boundary', *Proc. Camb. Phil. Soc.*, **49**, 169-174, 1953.
- [12] F.X. Caradonna, G.H. Laub and C. Tung, 'An Experimental Study of the Rotor-Vortex Interaction', *NASA TM-86005*, 1984.
- [13] F.X. Caradonna, J.L. Lautenschlager and M.J. Silva, 'An Experimental Study of Rotor-Vortex Interaction', *AIAA Paper 88-0045*, 1988.
- [14] C.M. Casciola, R. Piva and P. Bassanini, 'Vorticity Generation on a Flat Surface in 3-D Flow', *Journal of Computational Physics*, **129**, 345-356, 1996.
- [15] C.C. Chang, R.L. Chern, 'A Numerical Study of Flow Around An Impulsively Started Circular-Cylinder By a Deterministic Vortex Method', *Journal of Fluid Mechanics*, **233**, 243-263, 1991.
- [16] A.Y. Cheer, 'Unsteady Separated Wake Behind an Impulsively Started Cylinder in Slightly Viscous Fluid', *Journal of Fluid Mechanics*, **201**, 485-505, 1983.
- [17] J.M. Chen and D.M. Chang, 'Unsteady Pressure Measurements for Parallel Vortex-Aerofoil Interaction at Low Speed', *Journal of Aircraft*, **34**, 330-336, 1997.
- [18] M. Cheng, T. Chew and S.C.Luo, 'A Hybrid Vortex Method for Flows Over a Bluff Body', *International Journal For Numerical Methods In Fluids*, **24**, 253-274, 1997.

- [19] Y.T. Chew, M. Cheng and S.C. Luo, 'A Numerical Study of Flow Past a Rotating Circular-Cylinder Using a Hybrid Vortex Scheme', *Journal of Fluid Mechanics*, **299**, 35–71, 1995.
- [20] A.J. Chorin, 'Numerical Study of Slightly Viscous Flow', *Journal Fluid Mechanics*, **57**, 785–798, 1973.
- [21] M.H. Chou, 'Simulation of Slight Viscous External Flow by a Grid-Particle Domain Decomposition method', *Computers and Fluids*, **Vol.24**, 333–347, 1995.
- [22] C.Y. Chow and M.K. Huang, 'Unsteady Flows About a Joukowski Airfoil in the Presence of Moving Vortices', *AIAA paper 83-0129*, 1983.
- [23] J.P. Christiansen, 'Numerical Simulation of Hydromechanics by the method of point vortices', *Journal of Computational Physics*, **13**, 369–379, 1973.
- [24] K. Chua and T.R. Quackenbush, 'Fast 3-Dimensional Vortex Method for Unsteady Wake Calculations', *AIAA Journal*, **31**, 1957–1958, 1993.
- [25] N.R. Clarke and O.R. Tutty, 'Construction and Validation of a Discrete Vortex Method for Two-Dimensional Incompressible Navier-Stokes Equations', *Computers and Fluids*, **23**, 751–783, 1994.
- [26] H. Cohen, 'Mathematics for Scientists and Engineers', Prentice-Hall International, 1992.
- [27] A.T. Conlinsk, 'Modern Helicopter Aerodynamics', *Annual Review of Fluid Mechanics*, **29**, 129–145, 1997.
- [28] C.M. Copland, 'The Generation of Transverse and Longitudinal Vortices in Low Speed Wind Tunnels', *Ph.D Thesis, University of Glasgow, October, 1997*

- [29] C.M. Copland, F.N. Coton and R.A. McD Galbraith, 'An Experimental Study of the Idealised Vortex System of a Novel Rotor Blade Tip', *The Aeronautical Journal*, August/September, 385–392, 1998.
- [30] S.C.R. Dennis and J.D. Hudson, 'Methods of Solution of the Velocity-Vorticity Formulation of the Navier-Stokes Equations', *Journal of Computational Physics*, **122**, 300–306, 1995.
- [31] T.L. Doligalski, T.L. Doligalski and J.D.A Walker, 'Vortex Interaction With Walls', *Annual Review of Fluid Mechanics*, **26**, 573–616, 1994.
- [32] L. van Dommelen and E.A. Rundensteiner, 'Fast, Adaptive Summation of Point Forces in the Two-Dimensional Poisson Equation', *Journal of Computational Physics*, **83**, 126–147, 1989.
- [33] C.I. Draghicescu and M. Draghicescu, 'A Fast Algorithm for Vortex Blob Interactions', *Journal of Computational Physics*, **116**, 69–78, 1995.
- [34] J.H. Ferziger and M. Peric, 'Computational Methods for Fluid Dynamics', Springer-Verlag, Berlin, 1996.
- [35] D. Fishelov, 'Simulation of Three-Dimensional Turbulent Flow in Non-Cartesian Geometry', *Journal of Computational Physics*, **115**, 249–266, 1994.
- [36] T.B. Gatski, M.Y. Hussaini and J.L. Lumley, 'Simulation and Modelling of Turbulent Flows', Oxford University Press, 1996.
- [37] A. Gharakhani and A.F. Ghoniem, 'Three-Dimensional Vortex Simulation of the Time- Dependent Incompressible Internal Viscous Flows', *Journal of Computational Physics*, **134**, 75–95, 1997.
- [38] L. Greengard and V. Rokhlin, 'A Fast Algorithm for Particle Simulations', *Journal of Computational Physics*, **73**, 325–348, 1987.

- [39] L. Greengard and W.D. Gropp, 'A Parallel Version of the Fast Multipole Method', *Computers and Mathematical Applications*, **20**, 63–71, 1990.
- [40] P.M. Gresho, 'Incompressible Fluid Dynamics: Some Fundamental Formulation Issues', *Annual Review of Fluid Mechanics*, **23**, 413–453, 1991.
- [41] J.C. Hardin and S.L. Lamkin, 'Aerocooustic Interaction of a Distributed Vortex with a Lift Joukowski Aerofoil', *AIAA paper 84-2287*, 1984.
- [42] J.L. Hess and A.M.O. Smith, 'Calculation of Potential Flow about Arbitrary Bodies', *Progress in Aeronautical Science*, **8**, 1–138, 1967.
- [43] M.B. Horner, J.N. Stewart and R.A. Galbraith et al, 'Preliminary Results From a Particle Image Velocimetry Study of Blade-Vortex Interaction', *The Aeronautical Journal*, **99**, 91–98, 1995.
- [44] M.B. Horner, R.A. McD. Galbraith and F. Cotton, 'Examination of Vortex Deformation During Blade-Vortex Interaction', *AIAA Journal*, **34**, 1188–1194, 1996.
- [45] T.M. Hsu and J.C. Wu, 'Theoretical and Numerical Study of Vortex-Airfoil Interaction Problem', *AIAA Paper No.86-1094*, 1986.
- [46] T.M. Hsu and J.C. Wu, 'Vortex Flow Model for the Blade Vortex Interaction Problem', *AIAA Journal*, **26**, 1988.
- [47] S.C. Hung and R.B. Kinney, 'Unsteady Flow Over a Grooved Wall: A Comparison of Two Numerical Methods', *International Journal For Numerical Methods In Fluids*, **8**, 1403–1437 1988.
- [48] S.A. Huyer and J.R. Grant, 'Computation of Unsteady Separated Flow Fields Using Anisotropic Vorticity Elements', *Journal of Fluid Engineering*, **118**, 839–849, 1996.

- [49] R.T. Johnston and J.P. Sullivan, 'Unsteady Wing Surface Pressure in the Wake of a Propellor', *AIAA Paper 92-0277*, 1992.
- [50] H.E. Jones and F.X. Caradonna, 'Full Potential Modelling of Blade-Vortex Interactions', *Vertica*, **12**, 129–145, 1988.
- [51] K. Kamemoto, 'On Attractive Features of the Vortex Methods', *Review of Computational Fluid Dynamics*, 1995.
- [52] J. Katz and A. Plotkin, 'Low-Speed Aerodynamics - From Wing Theory to Panel Methods', *International Edition*, 1991.
- [53] T. Kita, T. Nagata and T. Nakajima, 'Far-field Condition of Vortex Methods on an Impulsively Started Two-dimensional Circular Cylinder with Rotation', *Physics of Fluids*, **6**, No.8, 2745–2756, 1992.
- [54] T. Kim and M.R. Flynn, 'Numerical Simulation of Air-Flow Around Multipole Objects Using the Discrete Vortex Method', *Journal of Wind Engineering and Industrial Aerodynamics*, **56**, 213–234, 1995.
- [55] M. Kiya, 'Simulating Three-Dimensional Vortex Motions by a Vortex Blob Method', *Sadhana*, **18**, 531–552, 1993.
- [56] Omar M. Knio and A.F.Ghoniem, 'Numerical Study of a Three-Dimensional Vortex Method', *Journal of Computational Physics*, **86**, 75–106, 1990.
- [57] A. Kokkalis, R. A. McD. Galbraith, 'Description of, and Preliminary Results from, a New Blade-vortex Interaction Test Facility', *Proceedings of 12th European Rotorcraft and Powered Lift Aircraft Forum*, 80.1–80.17, 1986.
- [58] P. Koumoutsakos, A. Leonard and F. Pepin, 'Boundary Conditions for Viscous Vortex Method', *Journal of Computational Physics*, **113**, 52–61, 1994.

- [59] P. Koumoutsakos and A. Leonard, ‘High-Resolution Simulations of the Flow Around an Impulsively Started Cylinder Using Vortex Methods’, *Journal of Fluid Mechanics*, **296**, 1–38, 1995.
- [60] S. Krishnamoorthy and J.S. Marshall, ‘Three-Dimensional Blade-Vortex Interaction in the Strong Vortex Regime’, *Physics of Fluids*, **10**, 2828–2845, 1998.
- [61] G.W. Kruse and P. Fischer, Center for FLuid Mechanics, Brown Univeristy, RI, (1996).
- [62] H. Lamb, ‘Hydrodynamics’, Cambridge University Press, 6th edition, 1932.
- [63] D.J. Lee and C.A. Smith, ‘Effect of Vortex Core Distortion on Blade-Vortex Interaction’, *AIAA Journal*, **29**, 1355–1362, 1991.
- [64] D.K. Lee, M.J. Downie and P. Bettess, ‘An Axisymmetrical Model of Separated Flow About A Sphere using Discrete Vortices’, *International Journal For Numerical Methods In Fluids*, **9**, 809–823, 1991.
- [65] A. Leonard, ‘Vortex Methods for Flow Simulation’, *Journal of Computational Physics*, **37**, 289–335, 1980.
- [66] A. Leonard, ‘Computing Three-Dimensional Incompressible Flows with Vortex Elements’, *Annual Review of Fluid Mechanics*, **17**, 523–549, 1985.
- [67] A. Leonard, ‘Direct Numerical Simulation’, *Simulation and Modeling of Turbulent Flows*, Edited by T.B. Gatski and M.Y. Hussaini, Oxford University, 1996.
- [68] R.I. Lewis, ‘Vortex Elements Methods for Fluid Dynamics Analysis of Engineering Systems’, Cambridge University Press, 1991.

- [69] H.Q. Lin, M. Vezza and R.A. McD. Galbrath, 'Discrete Vortex Method for Simulating Unsteady Flow Around Pitching Aerofoils', *AIAA Journal*, **35**, 494–499, 1997.
- [70] A.S. Lyrintzis, E.K. Koutsavdis and R.C. Strawn 'A Comparison of Computational Aeroacoustic Prediction Methods', *Journal of the American Helicopter Society*, **42**, 54–57, 1997.
- [71] J.S. Marshall and R. Yalamanchill, 'Vortex Cutting by a Blade, Part II. Computation of the Vortex Response', *AIAA Journal*, **32**, 1428–1436, 1994.
- [72] J.S. Marshall and J.R. Grant, 'Penetration of a Blade into a Vortex Core: Vorticity Response and Unsteady Blade Forces', *Journal of Fluid Mechanics*, **306**, 83–109, 1996.
- [73] J.S. Marshall and J.R. Grant, 'A Method for Determining the Velocity Induced by Highly Anisotropic Vorticity Blobs', *Journal of Computational Physics*, **126**, 286–298, 1996.
- [74] C.A. Masson, R.B. Green et al , 'An Experimental Investigation of a Loaded Blade-Vortex Interacting with Single and Twin Vortices', *Proceedings of the Technical Specialists' Meeting for Rotorcraft Acoustics and Aerodynamics*, Williamsburg, Virginia, 1997.
- [75] J.A. Miller and D.P. Telionis, 'International Symposium on Nonsteady Fluid Dynamics', University of Toronto, Toronto, Canada, 1990.
- [76] S. Mittal, 'Stabilized Space-time Finite Element Formulation for Unsteady Incompressible Flows', *Ph.D Thesis*, University of Minnesota, 1992.
- [77] D.T. Mook and Bonian Dong, 'Perspective: Numerical Simulations of Wakes and Blade Vortex Interaction', *Journal of Fluid Engineering*, **116**, 5–21, 1994.

- [78] C.P. Mracek, M.J. Kim and D.T. Mook, 'Three-Dimensional Potential Flows by a Vorticity-Panel Method', *Computers and Fluids*, **21**, 31–42, 1992.
- [79] Y. Nakanishi and K. Kamemoto, 'Numerical Simulation of the Flow Around a Sphere with Vortex Blobs', *Journal of Wind Engineering and Industrial Aerodynamics*, **46-47**, 363–369, 1993.
- [80] Y. Ogami and T. Akamatsu, 'Viscous Flow Simulation Using the Discrete Vortex Model - The Diffusion Velocity Method', *Computers and Fluids*, **19**, 403–411, 1991.
- [81] R. Padakannaya, 'Experimental Study of Rotor Unsteady Airloads due to Blade Vortex Interaction', *NASA CR-1909*, 1971.
- [82] A. Panaras, 'Numerical Modelling of the Vortex/Aerofoil Interaction', *AIAA Journal*, **25**, 5–11, 1987.
- [83] R. Parthasarthy and K. Karamcheti, 'Aerodynamic Sound Generation due to Vortex-Aerofoil Interaction', *AIAA paper 73-224*, 1973.
- [84] D.R. Poling, D.P. Telionis and L. Dadone, 'Blade-Vortex Interaction', *AIAA Journal*, **28**, 694–699, 1989.
- [85] Gavin J. Pringle, 'Numerical Study of Three-Dimensional Flow Using Fast Parallel Particle Algorithms', *Ph.D. Thesis*, Napier University, Edinburgh, 1994.
- [86] L. Qian and M. Vezza, 'The 3-D Vortex Particle Method and the Fast Summation Algorithm', *Glasgow University Aero Report*, No. 9620, 1996.
- [87] L. Qian and M. Vezza, 'Discrete Vortex Simulation of Aerofoil Blade-Vortex Interaction', *Proceedings of 2nd East European Conference on Wind Engineering*, **Vol.2**, 517–524, Prague, Czech Republic, 7-11 Sept, 1998.

- [88] L. Qian and M. Vezza, 'Simulation of Parallel Blade-Vortex Interaction Using a Discrete Vortex Method', *The Aeronautical Journal*, 537-543, November, 1999.
- [89] L. Qian and M. Vezza, 'A Vorticity-based Method for Incompressible Unsteady Viscous Flows', *Journal of Computational Physics*, **172**, 515-541, 2001.
- [90] L. Qian and M. Vezza, 'Development of a Vorticity-based Method for Studying Bluff Body Flows', *IUTAM Symposium on Bluff Body Wakes and Vortex-Induced Vibrations*, Marseille, France, 13-16 June, 2000.
- [91] M.M. Rai, 'Navier-Stokes Simulations of Blade-Vortex Interaction Using High-order Accurate Upwind Scheme', *AIAA paper 87-0543*, 1987.
- [92] D. Rockwell, 'Vortex-Body Interactions', *Annual Review of Fluid Mechanics*, **30** 199-229, 1998.
- [93] A. Roshko, 'On the Development of Turbulent Wakes from Vortex Sheets' *NACA Rep. 1191*, 1954.
- [94] P.G. Saffman, 'The Velocity of Viscous Rings', *Stud. Appl. Maths*, **49**, 371-380, 1970.
- [95] E. Saliveros, R.A.McD. Galbraith, 'Collected Data from Blade Vortex Interaction Tests Using a Single Blade, Non-Lifting Rotor', *Glasgow Univ. G.U. Aero Rept.9007-9009*, Glasgow, Scotland, UK, March, 1990.
- [96] T. Sarpkaya, 'Computational Methods with Vortices-The 1988 Freeman Scholar Lecture', *Journal of Fluid Engineering*, **111**, 5-52, 1989.
- [97] K.E. Schmidt and M.A. Lee, 'Implementing the Fast Multipole Method in Three Dimensions', *Journal of Statistical Physics*, **63**, Nos.5/6, 1123-1235, 1991.

- [98] W. R. Sears, 'Aerodynamics, Noise, and the Sonic Boom', *AIAA Journal*, **7**, 557–586, 1969.
- [99] D.D. Seath, J. M. Kim and D.R. Wilson, 'Investigation of the Parallel Blade-Vortex Interaction at Low Speed', *Journal of Aircraft*, **26**, 328–333, 1989.
- [100] S. Shankar and L. van Dommelen, 'A New Diffusion Procedure for Vortex Methods', *Journal of Computational Physics*, **127**, 88–109, 1996.
- [101] S. Shankar, 'A New Mesh-free Vortex Method', Ph.D thesis, Florida State University, (1996)
- [102] W.Z. Shen and T.P. Loc, 'Simulation of 2D External Viscous Flows By Means of a Domain Decomposition Method Using An Influence Matrix Technique', *International Journal For Numerical Methods In Fluids*, **20**, 1111–1136, 1995.
- [103] W.Z. Shen and T.P. Loc, 'Numerical Method for Unsteady 3D Navier-Stokes Equations in Velocity-Vorticity Form', *Computers and Fluids*, **26**, 193–216, 1997.
- [104] W.Z. Shen, T.P. Loc, 'A Coupling Finite Difference Particle Method for the Resolution 2D Navier-Stokes Equations in Velocity-Vorticity form', *Aerospace Science and Technology*, **1**, 97–109, 1997.
- [105] F.S. Sherman, 'Viscous Flow', McGraw-Hill, 1990.
- [106] C. Shih, L. Lourenco, L. van Dommelen and A. Krothapdli, 'Unsteady Flow Past an Aerofoil pitching at a constant rate', *AIAA Journal*, **30**, No.5, 1153–1161, 1992.
- [107] P.A. Smith and P.K. Stansby, 'Impulsively Started Flow Around a Circular Cylinder by the Vortex Method', *Journal of Fluid Mechanics*, **194**, 45–77, 1989.

- [108] P.R. Spalart, 'Vortex Methods for Separated Flows', *NASA TM 100068*, 1988.
- [109] P. Stow, 'Computational Methods in Aeronautical Fluid Dynamics', Oxford University, 1990.
- [110] J. Straus, P. Renzoni, R.E. Mayle 'Airfoil Pressure Measurements During a Blade-Vortex Interaction and a Comparison with Theory', *AIAA Journal*, **28**, 222–228, 1990.
- [111] M. Surendraiah, 'An Experimental Study of Rotor Blade-Vortex Interaction', *M.S. Thesis, Dept. of Aerospace Engineering, Pennsylvania State Univ., University Park, PA*, 1969.
- [112] I. J. Taylor and M. Vezza, 'Development and Validation of a Discrete Vortex Method for the Prediction of Separated Incompressible Flows Around Bluff Bodies', *Glasgow University Aero Report*, No. 9622, 1996.
- [113] I. J. Taylor and M. Vezza, 'Application of a Zonal Decomposition Algorithm to Improve the Computational Count of the Discrete Vortex Calculation', *Glasgow University Aero Report*, No. 9711, 1997.
- [114] I.H. Tuncer, J.C. Wu and C.M. Wang, 'Theoretical and Numerical Studies of Oscillating Airfoils', *AIAA Journal*, **Vol.28**, 1614-1624, 1990.
- [115] M. Vezza and R.A.McD. Galbraith, 'A Method for Predicting Unsteady Potential Flow about an Aerofoil', *International Journal of Numerical Methods in Fluids*, **5**, 347–356, 1985.
- [116] M. Vezza and R.A.McD. Galbraith, 'An Inviscid Model of Unsteady Aerofoil Flow with Fixed Upper Surface Separation', *International Journal of Numerical Methods in Fluids*, **5**, 577–592, 1985.

- [117] J.H. Walther and A. Larsen, 'Two Dimensional Discrete Vortex Method for Application to Bluff Body Aerodynamics', *Journal of Wind Engineering and Industrial Aerodynamics*, **67-68**, 183-193, 1997.
- [118] A. Weigand, 'The Response of a Vortex Ring to a Transient, Spatial Cut', *Ph.D Dissertation, University of California, San Diego*, 1993.
- [119] E. Weinan and J.G. Liu, 'Vorticity Boundary-Condition and Related Issues for Finite-Difference Scheme', *Journal of Computational Physics*, **124**, 368-382, 1996.
- [120] G.S. Winckelmans and A Leonard, 'Contribution to Vortex Particle Methods for the Computation of Three-Dimensional Incompressible Unsteady Flows', *Journal of Computational Physics*, **109**, 247-273, 1993.
- [121] J.C. Wu, 'Theory for Aerodynamic Force and Moment in Viscous Flows', *AIAA Journal*, **19**, 432-441, 1981.
- [122] J.C.Wu and U. Gulcat, 'Separate Treatment of Attached and Detached Flow Regions in General Viscous Flows', *AIAA Journal*, **19**, 20-27, 1981.
- [123] J.C. Wu and J.F. Thompson, 'Numerical Solution of Time-Dependent Incompressible Navier-Stokes Equation Using an Integro-Differential Formulation', *Computers and Fluids*, **1**, 197-215, 1973.

